Contents

List of Tables

List of Figures

Abstract

This thesis deals with the development of quantitative object selection methods and their application to the digital database of the Hamburg/ESO objective prism survey (HES), which covers the total southern extragalactic sky in the magnitude range $12 \lesssim B_J \lesssim 17.5$. The aim is a systematic exploitation of the stellar content of the HES.

A flexible, robust algorithm for detection of stellar absorption and emission lines in HES spectra was implemented. Equivalent widths for the strongest stellar absorption lines were derived for all 3 437 630 spectra (87 % of the HES) used in this work. Broad band ($U-B$, $B-V$) and narrow band (Strömgren c_1) colours were also derived directly from HES spectra, with precisions of $\sigma_{U-B} = 0.092^m$; $\sigma_{B-V} = 0.095^m$; $\sigma_{c_1} = 0.15^m$. Together with continuum parameters derived by principal component analysis, the above features are used for quantitative object selection.

For selection of extremely metal-poor halo stars, automatic spectral classification was employed. Spectroscopic follow-up observations of 58 stars showed that the selection in the HES has a more than three times higher efficiency then the selection in the the so-called HK survey of Beers et al., the up to now largest survey for metal-poor stars. The effective yield of turnoff stars with [Fe/H] < -2.0 is 80 %, in the HES, but only 22 % in the HK survey on average. This is very remarkable considering the fact that the spectral resolution of the HES (~ 10 Å at Ca K) is two times *lower* than in the HK survey (~ 5 Å). In spectroscopic follow-up campaigns of metal-poor stars carried out so far, 90 metal-poor stars were discovered; 11 are unevolved stars with [Fe/H] ≤ -3.0. Since in the HK survey 37 stars with [Fe/H] ≤ -3.0 and $0.3 < (B-V)_0 < 0.5$ were found, the sample of unevolved, extremely metal-poor stars was increased noticably.

Again by automatic spectral classification, it was searched for Field Horizontal-Branch A-type stars (FHB/A) in the HES. In a sample of 104 stars for which follow-up observations were obtained, 91 (or 88 %) turned out to be A-type stars. The HES FHB/A sample contains stars down to $V \sim 17.5$, so that distances of almost 25 kpc from the sun can be reached.

Other object types can be selected efficiently by simpler selection methods. For the selection of carbon stars, cutoff lines in two-dimensional feature spaces were constructed to separate stars with either two strong C_2 or two CN absorption bands from "normal" stars. Application of this procedure to the spectra present on 329 HES plates (effective area $\sim 6400\,\mathrm{deg}^2$) led to the identification of 351 carbon stars. The mean surface density detected by the HES hence is $0.055\,\mathrm{deg}^{-2}$, which is almost a factor three higher than the surface density found by Green et al. (1994) in their photometric CCD survey. Moreover, the survey of Green et al. is $\sim 1.5^m$ *deeper* than the HES ($V_{\mathrm{lim}} \approx 16.5$ in the HES; $V_{\mathrm{lim}} \approx 18.0$ for the Green et al. survey). This indicates that photometric carbon star surveys are highly incomplete.

We started to obtain recent-epoch CCD images for HES carbon stars, in order to measure their proper motions (p.m.) by comparison of these images with archival plate material (DSS-I, POSS, USNO-catalog 2.0). The aim of this project is to increase the sample of dwarf carbon stars (dCs). Up to now, one dC was rediscovered; another star is a likely candidate for a dC, but it can not be ruled out by its p.m. that it is a subgiant. Unfortunately, the selection probability for high p.m. objects in the HES is reduced due to an epoch difference between the direct plates of the DSS-I, used for object detection, and the HES spectral plates. Simulations show that nevertheless ~ 20 new dCs are expected to be found in the HEs. This would *triple* the dC sample.

The epoch difference problem is also relevant for searching white dwarfs (WDs) in the HES. A rough estimation indicates that only in the order of 50 % of all WDs can be found in the HES, without employing special techniques to correct for for their p.m. However, it was found that even without using such techniques, we detect a higher surface density of WDs than the PG survey. This is most likely due to the fact that samples of DA white dwarfs drawn from UV-excess surveys are incomplete at the cool end, if too strict selection criteria are employed and/or colour measurements are inccurate. In the HES, cool DAs with temperatures above ~ 9000 K can readily be identified by their broad Balmer lines.

Further projects aimed at the selection of hot subdwarfs (sdO, sdB), magnetic DB white dwarfs, DZ white dwarfs, and cataclysmic variable stars in the HES.

Zusammenfassung

Inhalt dieser Dissertation ist die Entwicklung von quantitativen Objektselektionsmethoden und ihre Anwendung auf die Datenbasis des digitalen Hamburg/ESO Objektivprismen-Surveys (HES), der den gesamten extragalaktischen Südhimmel im Helligkeitsbereich $12 \lesssim B_J \lesssim 17.5$ abdeckt. Ziel ist die systematische Ausbeutung des stellaren Inhalts des HES.

Es wurde ein flexibler und robuster Algorithmus zur Detektion von stellaren Absorptions- und Emissionslinien entwickelt. Die Äquivalentbreiten der stärksten stellaren Absorptionslinien wurden für alle 3 437 630 Spektren, die in dieser Arbeit verwendet wurden (87 % des HES), berechnet. Breitband-Farben ($U-B$, $B-V$) und Schmalband-Farben (Strömgren c_1) wurden mit Genauigkeiten von $\sigma_{U-B} = 0.092^m$; $\sigma_{B-V} = 0.095^m$ und $\sigma_{c_1} = 0.15^m$ direkt von den HES-Spektren abgeleitet. Drei weitere Parameter, gewonnen durch Hauptkomponentenanalyse, beschreiben den Kontinuumsverlauf der HES-Spektren. All diese Merkmale bilden die Basis für quantitative Selektionsmethoden.

Bei der Suche nach extrem metallarmen Halosternen wurde automatische Spektralklassifikation erfolgreich eingesetzt. Spektroskopische Nachbeobachtung und Analyse einer Stichprobe von 58 Sternen zeigte, dass die Selektion im HES mehr als dreimal effizienter ist als die visuelle Selektion im bisher grössten Survey dieser Art, dem so genannten HK-Survey von Beers et al.: Die Erfolgsrate bei der Suche nach Sternen mit [Fe/H] < -2.0 nahe dem Hauptreihen-*turnoff* beträgt im HES 80 %, im HK-Survey hingegen im Mittel nur 22 %. Dies ist umso bemerkenswerter, als die spektrale Auflösung des HES (ca. 10 Å bei Ca K) um einen Faktor 2 *niedriger* ist als die des HK-Survey (ca. 5 Å). In Nachbeobachtungskampagnen wurden bisher insgesamt 90 metallarme Sterne entdeckt; 11 davon sind turnoff-Sterne mit [Fe/H] ≤ -3.0. Im HK-Survey wurden 37 Sterne mit [Fe/H] ≤ -3.0 und $0.3 < (B-V)_0 < 0.5$ gefunden, so dass die Stichprobe merkbar vergrössert wurde.

Ebenfalls mit automatischer Klassifikation wurde im HES nach Feld-Horizontalast-A-Sternen (FHB/A) gesucht. Von 104 nachbeobachteten Sternen sind 91 (oder 88 %) tatsächlich A-Sterne. Die Stichprobe enthält Sterne bis zu $V \approx 17.5$, so dass Entfernungen von nahezu 25 kpc von der Sonne erreicht werden.

Bei anderen Objekttypen reichen einfachere Methoden zur effizienten Objektselektion aus. Kohlenstoffsterne wurden mit Hilfe von Trennlinien in zweidimensionalen Merkmalsräumen selektiert, die Sterne mit jeweils zwei starken C_2 oder zwei CN-Banden von "normalen" Sternen separieren. Die Anwendung der Selektion auf die Spektren von 329 HES-Platten (effektive Fläche ca. 6 400 deg^2) führte zur Identifikation von 351 Kohlenstoffsternen. Die mittlere Oberflächendichte beträgt somit 0.055 deg^{-2}, was fast um einen Faktor 3 höher ist als der von Green et al. (1994) gefundene Wert von 0.02 deg^{-2}, obwohl der photometrische Survey von Green et al. 1.5 mag *tiefer* ist ($V_{\rm lim} \approx 16.5$ im HES; $V_{\rm lim} \approx 18.0$ bei Green et al.). Dies legt die Vermutung nahe, dass photometrische Kohlenstoffstern-Surveys hochgradig unvollständig sind.

Es wurde damit begonnen, durch Vergleich von neu aufgenommenen CCD-Bildern mit Archivdaten (DSS-I, POSS, USNO-Katalog 2.0) Eigenbewegungen der HES-Kohlenstoffsterne zu bestimmen, um Zwerg-Kohlenstoffsterne (dCs) zu finden. Dabei wurde ein dC wiederentdeckt; ein weiterer Stern ist ein guter dC-Kandidat, jedoch kann anhand der gemessenen Eigenbewegung nicht ausgeschlossen werden, dass es sich um einen Unterriesen handelt. Unglücklicher Weise ist im HES die Selektionswahrscheinlichkeit für Sterne mit Eigenbewegung wegen einer Epochendifferenz zwischen den Direkaufnahmen den DSS-I und den Spektralplatten reduziert. Die Direktaufnahmen des DSS-I werden im HES zur Objektdetektion verwendet. Mit Simulationen wurde jedoch abgeschätzt, dass im HES ca. 20 neue dCs entdeckt werden sollten. Dies würde die Zahl der bekannten dCs *verdreifachen*.

Das Epochendifferenz-Problem tritt auch bei der Suche nach weissen Zwergen (WDs) auf. Eine grobe Abschätzung deutet darauf hin, dass ohne Anwendung spezieller Techniken zur Kompensation von Eigenbewegungen nur 50 % aller WDs im HES gefunden werden können. Andererseits kann aber die in vielen UV-Exzess-Surveys vorhandene Unvollständigkeit bei kühlen DAs – verursacht durch zu strenge Selektionskriterien und/oder ungenaue Farben – im HES umgangen werden, da ihre breiten Balmerlinien ab 9 000 K in HES-Spektren leicht erkannt werden können. Es gibt Hinweise darauf, dass im HES trotz o.g. Unvollständigkeit *insgesamt* eine höhere WD-Oberflächendichte detektiert wird als im PG-Survey.

Weitere Projekte hatten die Suche nach heissen Subdwarfs (sdO, sdB), magnetischen weissen Zwergen vom Typ DB, DZ weissen Zwergen und kataklysmischen Veränderlichen zum Inhalt.

1 Introduction

The Hamburg/ESO survey (HES; Wisotzki et al. 1996; Reimers & Wisotzki 1997; Wisotzki et al. 2000) is an objective-prism survey primarily targeting bright ($B_J > 17.5$) quasars. However, it was recognized right from the beginning (Reimers 1990) that the seeing-limited spectral resolution of the HES (~ 15 Å at Hγ) makes it possible to detect the strongest stellar absorption (or emission) features, so that the *stellar* content of the HES can be exploited systematically as well.

Below I give an overview of other ongoing or recently completed wide-angle surveys in the optical which aim at least partly at finding stars at high galactic latitude, and hence compete with the HES. In the sections of this thesis dealing with specific object types, I give more detailed comparisons of some of these surveys with the HES, and discuss their strengths and weaknesses.

The HK survey is a spectroscopic survey based on "narrow-band" objective prism plates, with a spectral range centered on Ca H+K (hence the name). It was conceived for searching field horizontal branch (FHB) and metal-poor stars at hight galactic latitude, in the northern and southern hemisphere (Beers et al. 1992*b*). Since the selection criterion for these stars was a weak or absent Ca K line, also many hot subdwarfs were discovered (Beers et al. 1992*a*). The faint limit of the HK survey is $B \simeq 15.5$.

The Montreal-Cambridge-Tololo survey (MCT) covers $6750\,\mathrm{deg}^2$ at $b < -30°$ in the southern hemisphere with U and B plates taken with the 0.6 m Curtis Schmidt telescope (Demers et al. 1986; Lamontagne et al. 2000). It aims at providing a complete list of blue ($U-B < -0.6$) stellar objects down to $B \simeq 16.5$.

The Edinburgh-Cape survey (EC) is a photometric survey targeting UV-excess ($U-B < -0.4$) objects in the southern hemisphere (Stobie et al. 1997; Kilkenny et al. 1997). It was originally planned to cover $\sim 10000\,\mathrm{deg}^2$ at $|b| > 30°$ and $\delta < 0°$. However, it was recently decided that some of the more northern fields will *not* be done (O'Donoghue 1999, priv. comm.). The EC goes deeper than the MCT survey; i.e., down to $B \simeq 18$. However, follow-up spectroscopy and photometry is obtained for objects of $B \lesssim 16.5$ only.

The Hamburg Quasar Survey (HQS) is another digital, Hamburg-based objective prism survey. It was carried out in the northern hemisphere, using the Hamburg-Schmidt telescope on Calar Alto (Spain). The HQS covers $11\,000\,\mathrm{deg}^2$ at high galactic latitudes (Hagen et al. 1995). It is deeper than the HES ($B > 18.5$), but has a $\sim 3\times$ lower spectral resolution. Apart from many quasars, its main targets, also a lot of interesting stars have been found in the course of quasar candidate follow-up observations (e.g., Jordan et al. 1998; Dobrzycka et al. 1998; Reimers et al. 1999). There are attempts under way to calibrate the HQS plates more accurately than it is currently the case, and select white dwarfs with quantitative criteria (Homeier 1999, priv. comm.). However, stellar work is much more difficult than in the HES, because of the lower spectral resolution, and less homogenous plate material.

The APM C star survey is an extension of the APM[1] high-redshift quasar survey, aiming at a coverage of the total high-latitude sky ($|b| > 30°$) in the northern and southern hemisphere (Totten & Irwin 1998). Cool carbon stars are selected in a $B_J - R$ colour-magnitude diagram. Limiting magnitudes are $B \simeq 20$ and $R \simeq 17$.

The Sloan Digital Sky Survey (SDSS) (see e.g. Gunn & Knapp 1993) is a deep ($V \lesssim 20$) CCD survey in the northern hemisphere. It is planned to cover ~ 10000 at high galactic latitudes with

[1] The acronym 'APM' refers to the Automatic Plate Measuring facility in Cambridge, UK.

photometry in five broad band filters. It uses the filter system $u'g'r'i'z'$ which is especially designed for the detection of high redshift quasars and galaxies, which are the primary targets. Simulations (Lenz et al. 1998) and first tests with real data (Margon & Szkody 1998) indicate that some stellar applications are feasible, too; e.g. selection of carbon stars, FHB/A stars, or CVs. However, Margon & Szkody (1998) show that a discrimination of metal-poor stars from the locus of normal stars is *not* possible in SDSS two-colour diagrams; on the other hand, Lenz et al. (1998) have developed refined methods that increase the metallicity separation for G-type stars. Metallicity separation *within* samples of stars at [Fe/H] < -2.0 becomes difficult especially for photometric surveys, since the change of broad-band colours with metallicity, caused by reduced line blocking in atmospheres of metal-poor stars, saturates at low metallicities. Hence, we can be curious about how efficient the SDSS can select metal-poor stars in practice.

In Sect. 2 I give a detailed description of the HES, including data reduction and plate calibration procedures. Sect. 3 deals with automatic spectral classification, one of the main selection techniques used for the exploitation of the stellar content of the HES. All remaining sections, with exception of Sect. 9, in which I give my conclusions, describe stellar applications of the HES. Finally, in Appendices A–C I list stars discovered in the course of projects carried out within my thesis work, and not listed in the sections describing the projects itself.

References

Beers, T. C., Doinidis, S. P., Griffin, K. E., Preston, G. W. & Shectman, S. A. (1992*a*), 'Spectroscopy of hot stars in the Galactic halo', *AJ* **103**, 267–296.

Beers, T. C., Preston, G. W. & Shectman, S. A. (1992*b*), 'A search for stars of very low metal abundance. II.', *AJ* **103**(6), 1987–2034.

Demers, S., Beland, S., Kibblewhite, E. J., Irwin, M. J. & Nithakorn, D. S. (1986), 'The Montreal-Cambridge survey of southern subluminous blue stars', *AJ* **92**, 878–884.

Dobrzycka, D., Dobrzycki, A., Engels, D. & Hagen, H.-J. (1998), 'HS 0551+7241: A New Possible Magnetic Cataclysmic Variable in the Hamburg-CfA Bright Quasar Survey', *AJ* **115**, 1634–1639.

Gunn, J. E. & Knapp, G. R. (1993), The Sloan Digital Sky Survey, *in* B. T. Soifer, ed., 'Sky Surveys: Protostars to Protogalaxies', Vol. 43 of *ASP Conf. Ser.*, pp. 267–279.

Hagen, H.-J., Groote, D., Engels, D. & Reimers, D. (1995), 'The Hamburg Quasar Survey. I. Schmidt observations and plate digitizations', *A&AS* **111**, 195–203.

Jordan, S., Koester, D., Vauclair, C., Dolez, N., Heber, U., Hagen, H.-J., Reimers, D., Chevreton, M. & Dreizler, S. (1998), 'HS 0507+0434: a double DA degenerate with a ZZ Ceti component', *A&A* **330**, 277–284.

Kilkenny, D., O'Donoghue, D., Koen, C., Stobie, R. S. & Chen, A. (1997), 'The Edinburgh-Cape Blue Object Survey – II. Zone 1 – The North Galactic Cap', *MNRAS* **287**, 867–893.

Lamontagne, R., Demers, S., Wesemael, F., Fontaine, G. & Irwin, M. J. (2000), 'The Montreal-Cambridge-Tololo Survey of Southern Subluminous Blue Stars: The South Galactic Cap', *AJ* **119**, 241–260.

Lenz, D. D., Newberg, H. J., Rosner, R., Richards, G. T. & Stoughton, C. (1998), 'Photometric Separation of Stellar Properties Using SDSS Filters', *ApJS* **119**, 121–140.

Margon, K. K. B. & Szkody, P. (1998), 'The Recognition of Unusual Objects in the Sloan Digital Sky Survey Color System', *PASP* **110**, 1342–1355.

Reimers, D. (1990), 'A Wide-Angle Objective Prism Survey for Bright Quasars', *The Messenger* **60**, 13–15.

Reimers, D. & Wisotzki, L. (1997), 'The Hamburg/ESO Survey', *The Messenger* **88**, 14–19.

Reimers, D., Hagen, H.-J. & Hopp, U. (1999), 'HS 1023+3900 – a magnetic CV in the period gap with a distinct cyclotron emission line spectrum', *A&A* **343**, 157–162.

Stobie, R. S., Kilkenny, D., O'Donoghue, D., Chen, A., Koen, C., Morgan, D. H., Barrow, J., Buckley, D. A. H., Cannon, R. D., Cass, C. J. P., Cranston, M. R., Drinkwater, M., Hartley, M., Hawkins, M. R. S., Hughes, S., Humphries, C. M., Macgillivray, H. T., McKenzie, P. B., Parker, Q. A., Read, M., Russell, K. S., Savage, A., Thomson, E. B., Tritton, S. B., Waldron, J. D., Warner, B. & Watson, F. G. (1997), 'The Edinburgh-Cape Blue Object Survey – I. Description of the survey', *MNRAS* **287**, 848–866.

Totten, E. J. & Irwin, M. J. (1998), 'The APM survey for cool carbon stars in the Galactic halo. I', *MNRAS* **294**, 1–27.

Wisotzki, L., Christlieb, N., Bade, N., Beckmann, V., Köhler, T., Vanelle, C. & Reimers, D. (2000), 'The Hamburg/ESO survey for bright QSOs. III. A large flux-limited sample of QSOs', A&A, in press.

Wisotzki, L., Köhler, T., Groote, D. & Reimers, D. (1996), 'The Hamburg/ESO survey for bright QSOs I. Survey design and candidate selection procedure', *A&AS* **115**, 227–233.

2 The Hamburg/ESO survey

2.1 Description of Plate Material

The HES is based on IIIa-J plates taken with the ESO Schmidt telescope and its 4° prism (Wisotzki et al. 1996, 2000). It covers the magnitude range $12.0 \gtrsim B_J \gtrsim 17.5$. The magnitude limit depends on plate quality. Note that the value given for the faint limit is the completeness limit for quasar search, which we define to be the average amplitude of the pixel-wise noise in the B_J band $> 5\sigma$ above the diffuse plate background, where σ is the background noise. The *detection limit* of the HES is $B_J \simeq 18$. For stellar applications, the survey magnitude range depends on the object type searched for. In our search for metal-poor stars, we only use spectra below a saturation threshold (which roughly corresponds to $B_J > 14.0$), and spectra with $S/N > 10$. However, for most object types we adopt the 5σ magnitude limit.

The atmospheric cutoff at the blue end and the sharp sensitivity cutoff of the IIIa-J emulsion ("red edge") result in a wavelength range of $3200\,\text{Å} < \lambda < 5300\,\text{Å}$ (see Fig. 4). The spectral resolution of the HES is primarily seeing-limited, and typically 15 Å FWHM at Hγ. For plates taken during good seeing conditions, the pixel spacings chosen in the digitization process results in an under-sampling, so that in these cases the spectral resolution is also limited by the sampling.

The definition of the HES survey area makes use of the mean star density Σ and average column density of neutral hydrogen, $N_{\rm H}$ for each ESO/SERC field. In 0th order, the HES area is defined by all fields which fulfill all of the following conditions:

$$\begin{aligned} +2.5^\circ > \quad \delta \quad &> -78^\circ \\ \Sigma \quad &< \quad 100\ \text{stars}/\text{deg}^2 \\ N_{\rm H} \quad &< \quad 10^{21}\,\text{cm}^{-2}. \end{aligned}$$

$N_{\rm H}$ has been taken from Dickey & Lockman (1990). The above conditions correspond roughly to galactic latitudes $|b| > 30\,$deg. A few fields have been added in order to have a "smooth" survey border. In result, the survey area consists of 380 fields. Objective-prism plates have been taken for all of these, and the plates have been digitized and reduced at Hamburger Sternwarte.[2] As one plate covers approximately $5\times 5\,$deg on the sky, the nominal survey area is $9\,500\,\text{deg}^2$, or the total southern extragalactic sky.

Of the 380 HES plates, 54 have been excluded from exploitation of the stellar content as of now. This has several reasons. First of all, at the time of preparing the plate data for processing with candidate selection algorithms, ~ 40 plates had not been digitized. Other plates have been excluded because files were corrupted due to defect storage media (these plates will have to be re-reduced, or – in a few cases – even re-scanned), or because some of the data (e.g. descriptors, names or content of table columns, etc.) was inconsistent with the rest of the data. Therefore, this work is restricted to 329 plates only.

2.2 Data Reduction

An overview of the HES data flow is given in Fig. 2.

[2] This sentence represents 11 years of work! The following people were involved (in alphabetical order): V. Beckmann, M. Brachmann, N. Christlieb, D. Groote, H. Hagen, M. Ikonomou, T. Köhler, D. Kühl, B. Kuhlbrodt, A. Müller, G. Pizzaro, O. Pizzaro, D. Reimers, H.E. Schuster, C. Vanelle, L. Wisotzki.

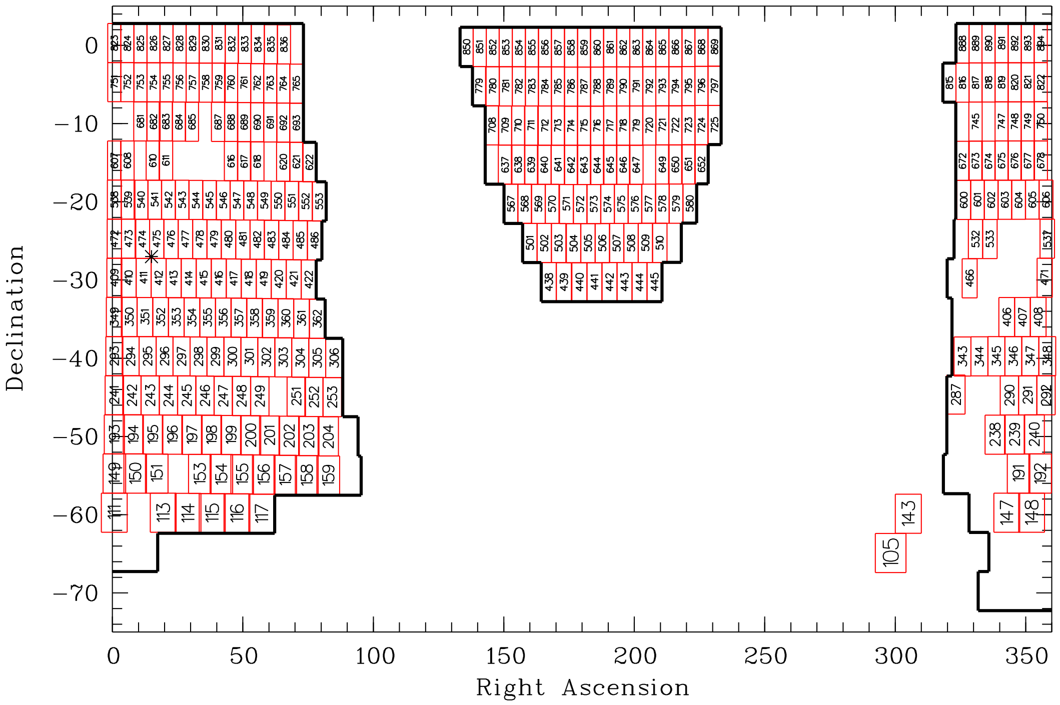

Figure 1: Definition of "official" HES area (framed) and numbers of fields in which the exploitation of the stellar content of the HES is currently carried out. For orientation, the position of the southern galactic pole is marked with '$*$' (lower left corner of field 475).

2.2.1 Plate Digitization

All HES plates have been digitized at Hamburger Sternwarte using a PDS 1010G microdensitometer (Hagen 1987). As the Hamburg PDS is too small for the large (28×28 cm) ESO plates, they have been scanned in four quadrants. The scan is performed with an $30 \times 30\,\mu$m aperture and $20\,\mu$m step width, yielding 7500×7500 pixels per plate quarter. The plate scale of the HES plates is $67\overset{\prime\prime}{.}5\,\mathrm{mm}^{-1}$, so that the centers of two pixels are separated by $1\overset{\prime\prime}{.}35$. The dispersion direction is declination, and increasing wavelength corresponds to increasing declination.

It takes about 16 hours to scan one plate. The raw data amount to ~ 430 MB per field. It is saved temporarily on magneto-optical discs (MOs) for data reduction, and after that archived on CD-ROMs. The data reduction was carried out on a dedicated PC with a Pentium 133 MHz processor, 96 MB RAM and Linux as operating system. The relevant periphery (CD-ROM drive and writer, MO drive) is attached directly to this PC, and ~ 8 GB of harddisk space is visible for it. The reduction of direct and spectral plate data of one field takes 6–8 hours.

2.2.2 Reduction of Direct Plate Data

For the automated reduction of the objective-prism plate data digitized *direct* plates of the *Digitized Sky Survey I* (DSS-I) are used (for an illustration see Fig. 3).

After background subtraction and object detection on the direct plates, an astrometric transformation between direct and objective-prism plates is computed. This yields an input catalog of object positions on the objective-prism plates for the extraction of the spectra, and the zero point for wave-

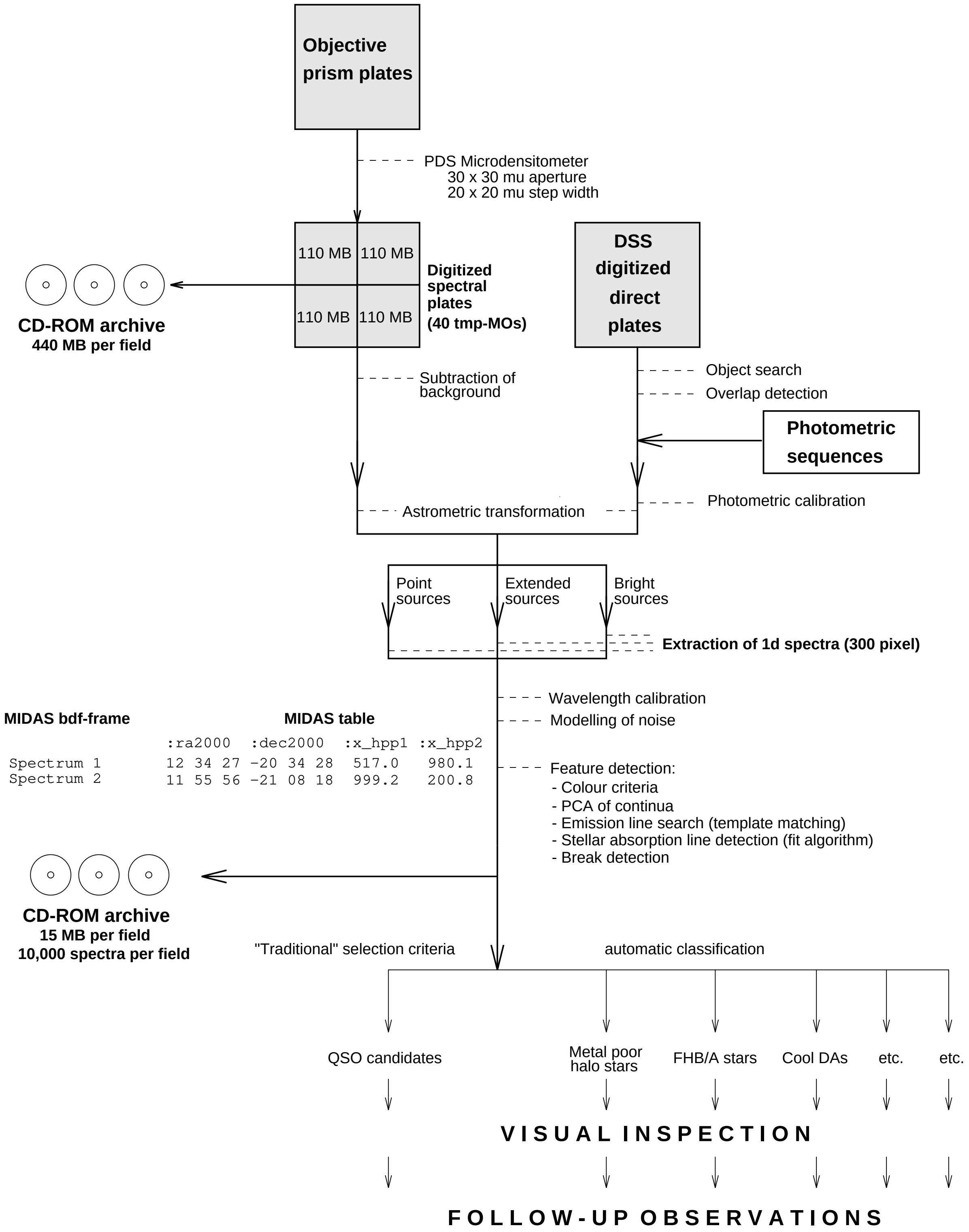

Figure 2: Overview of HES data flow.

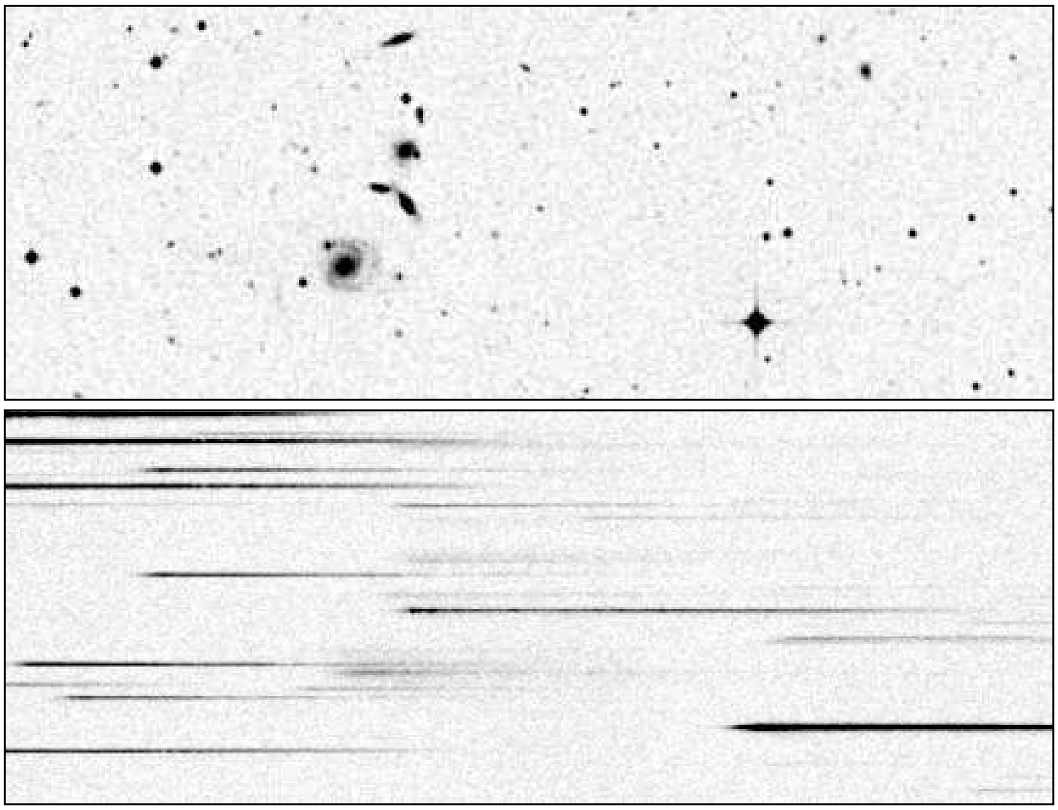

Figure 3: Direct plate scan of the *Digitized Sky Survey I* and corresponding HES plate scan. The wing-shaped object in middle height and slightly to the left in the direct scan is a pair of interacting galaxies with a Seyfert 1 nucleus (HE 0323-4204) at $z = 0.058$.

length calibration.

Although this procedure is appropriate for the primary targets of the HES, i.e. quasars, it is problematic for objects which have a large proper motion. This lesson was learned in the course of a search for dwarf carbon stars (see Sect. 5). The feature detection algorithms failed for G77-61, a dwarf carbon star with $\mu_\alpha = 0\farcs184\,\mathrm{yr}^{-1}$, $\mu_\delta = -0\farcs745\,\mathrm{yr}^{-1}$ (Deutsch 1994). Since the epoch difference Δt between the HES plate and the relevant DSS I plate is ~ 10 years (a typical value), the proper motion results in -5.6 and 1.4 pixel offsets in dispersion direction and perpendicular to the dispersion direction, respectively. Therefore, too low C_2 band index values have been measured. Proper motions along dispersion direction (i.e., declination) can at least partly be recovered by using special techniques, e.g. shifting templates through the spectrum. However, if $\mu_\alpha \cdot \Delta t$ is large, the spectrum of the object is not found on the HES plate, and only sky background is extracted.

Overlapping spectra (hereafter shortly called overlaps) are also detected with the help of the direct data: For each spectrum to be extracted, it is looked for objects in the dispersion direction on the direct plate. If there is one, the automatic procedure marks the corresponding spectrum, so that it can later be excluded from further processing, if this is desired. *It is* desired for stellar work, since the feature detection and automatic classification algorithms would get confused otherwise, and a lot of “garbage” would enter the candidate samples. The elimination of overlaps reduces the HES area from a nominal $9\,500\,\mathrm{deg}^2$ to an effective area of $\sim 7\,500\,\mathrm{deg}^2$. The overlap rate is strongly dependend on galactic lattitude b and varies between 10 % and 50 % within the survey area. 20 % is an average overlap rate for the total survey.

2.2.3 Photometry

Photometric calibration of HES plates is performed by calibrating the direct plates with individual photometric sequences, and after that calibrating the spectral plates with these magnitudes (Köhler 1991; Vanelle 1996). The overall accuracy including zero point error is less than ± 0.2 mag in B_J. Photometric sequences are available for all of the 383 HES plates, and the calibration has been carried out for all 329 plates on which stellar work is done so far.

The B_J band is formally defined by the spectral sensitivity curve of the Kodak IIIa-J emulsion multiplied with the filter curve of a Schott GG395 filter. B_J can be converted to B using the formula

$$B = B_J + 0.28 \cdot (B - V), \tag{1}$$

which is valid for main-sequence stars in the colour range $-0.1 < (B - V) < 1.6$ (Hewett et al. 1995).

2.2.4 Extraction of Objective-Prism Spectra

Extraction of the objective-prism spectra is done by optimal procedures, maximizing S/N. According to their appearance on the direct plates, and brightness on HES plates, three types of objects are extracted in different ways:

`stars` The spectra of point-like sources are extracted by fitting Gaussian profiles to the 2–3 pixels with the highest density values in each column perpendicular to the dispersion direction. The width of the profile is held fixed at a value which is determined globally for each plate. The maximum of the fitted profile curve is taken as extraction value.

`ext` Spectra of sources which appear extended on the direct plates are extracted in a similar manner as point-like sources, but the width of the spectral profile is *not* held fixed during the fitting procedure, and more pixels are used for the fit. Note that `ext`-sources are not necessarily galaxies. For example, if point-like sources are located in diffraction spikes of very bright objects or when two objects are located very close to each other, so that they overlap on the direct plates, they are classified as extended.

`bright` Spectra of objects close to saturation are extracted by *summing* the density values in each column perpendicular to the dispersion direction. This results in an extension of the dynamic range of the objective-prism plates by 2–3 magnitudes.

Each extracted, one-dimensional spectrum consists of 300 pixels. 20 pixels redward of the red edge are included, and 280 pixels blueward (towards *increasing* scan length `x`). Pixel values are densities D above diffuse plate background (bgr) in arbitrary units called counts. The relation between counts and photographic densities $D_{\rm photo}$ is

$$D_{\rm photo} = \frac{D\,[\rm counts] + D_{\rm bgr}\,[\rm counts]}{800}. \tag{2}$$

The HES spectra are stored as MIDAS frames, in which each row represents one spectrum. Each frame is accompanied by a MIDAS table, in which additional information for each spectrum is stored row-wise, e.g. object position on the sky, magnitude, and values for spectral features (see Section 3.2).

The mean number of overlap-free spectra with $S/N > 5$ is ~ 10000 per plate, so that the data base of the HES (including the 54 plates not yet prepared for stellar work) consists of ~ 4 million usable digital spectra. The number of spectra present on the 329 plates used in this work (effective area $\sim 6400\,\mathrm{deg}^2$ is 3 437 630.

2.2.5 Wavelength Calibration

A global dispersion relation for all HES plates has been determined by Ikonomou (1995), using A-type stars. In HES spectra of these stars the Balmer lines at least up to H_{10} are resolved (see Fig. 4), so that a dispersion relation can be computed by comparing the x-positions (scan length in μm) of these lines, determined by template matching, with the known wavelengths. The wavelength calibration zero point is specified by the astrometric transformation between direct plates and spectral plates. The relation between λ[Å] and $x\,[\mu\mathrm{m}]$ is given by the following expression:

$$x = -2953.588 + 8.218377 \cdot 10^{10} \cdot \frac{1}{\lambda^2} + 7.675455 \cdot 10^{16} \cdot \frac{1}{\lambda^4} \tag{3}$$

The wavelength calibration is accurate to $\pm 10\mu$m. This corresponds to ± 13 Å at Hγ and ± 5 Å at $\lambda = 3500$ Å.

2.2.6 Estimation of the Amplitude of Pixel-Wise Noise

The amplitude of pixel-wise noise as a function of density D is determined plate-wise using A-type stars (see also Christlieb 1995). A straight line fit is done to the spectral region between Hβ and Hγ (see Fig. 4). The scatter around the fit is purely due to noise, since in A-type stars the spectral region under consideration is free of absorption lines at the spectral resolution of the HES.

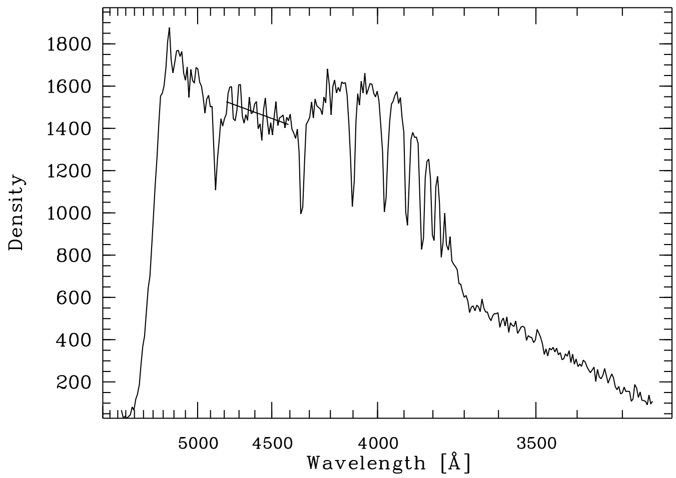

Figure 4: Measurement of noise in absorption line free spectral region of A-type stars. Note that we plot HES objective prism spectra such that wavelengths are *decreasing* towards the right, because the scan length x is *increasing* in this direction. The sharp drop of the spectra at the red end is due to the IIIa-J emulsion sensitivity cutoff at ~ 5400 Å.

We measure the amplitude of the scatter for all A-type stars present on each HES plate (typically ~ 50 per plate), and compute the mean density in the fit region. This yields data points (D, noise), to which a 2nd order polynomial is fitted, i.e.

$$\mathrm{noise} = a_0 + a_1 \cdot D + a_2 \cdot D^2. \tag{4}$$

We use a robust fit algorithm minimizing the sum of absolute deviations, and the following set of boundary conditions:

$a_0 > 0$. The noise at $D = 0$ is the noise of the plate background, which is always > 0.

$a_2 \geq 0$. Since $D \geq 0$, and the noise increases monotonically with D, a_2 must be positive (or zero).

$a_1 \geq 0$. From the previous boundary condition follows that the polynomial has a minimum at $D_{\rm min} = -a_1/(2a_2)$. Using again the argument that the noise increases monotonically with D, it follows that $D_{\rm min} \leq 0$. Since $a_2 \geq 0$, a_1 must be ≥ 0.

An example for a such a fit is shown in Fig. 5.

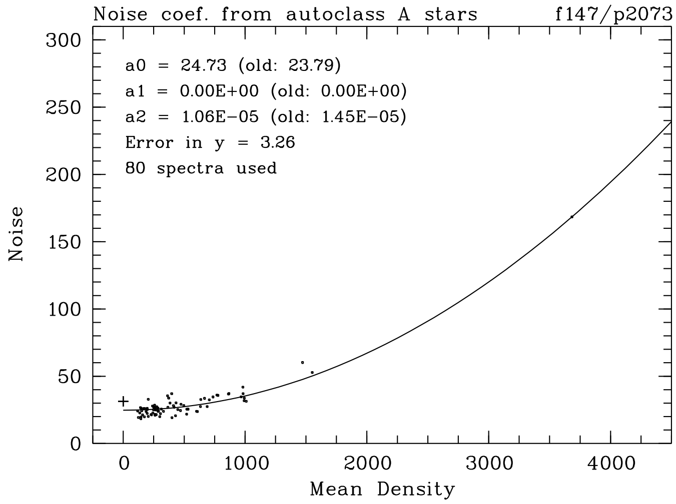

Figure 5: Fitting of a 2nd order polynomial to data points (D, noise), for estimation of pixel-wise noise as a function of density. The plate background noise is marked with '+'. It is always higher than expected from the noise parabola fit, since the optimal spectrum extraction algorithms result in a bias towards lower noise.

For simulations of spectra (see Sect. 3.1) it is very important to know the *form* of the distribution of noise. We investigated this by using 50 spectra of A-type stars from 8 plates with high sky background ($D > 1\,500$), and 60 spectra from 7 plates with low background ($D < 700$) – see Tab. 1. These spectra were chosen by hand from the sample of automatically selected A-type stars, in order to ensure that misclassified spectra, and spectra for which the fit of the continuum between Hβ and Hγ by a straight line is not fully adequate, do not confuse the results. 5 of the original set of 115 spectra have been excluded in the manual selection process.

The deviations from the continuum fits were collected for each spectrum, shifted to a median of 0, and divided by the average of the absolute values of the upper and lower 50 % quartile, so that a comparison of the noise distributions measured in different spectra (with different noise amplitude) is possible. The result is that the distribution of pixel-wise noise is almost perfectly Gaussian, independently of plate background (see Fig. 6).

An approximate relation between average S/N in the B_J band and B_J magnitudes has been derived by using 507 spectra from many different plates. Overlapping spectra undetected by the automatic overlap recognition algorithm, and spectra from plates with unusually high sky background have been excluded from the fit by iterative 3σ clipping. The resulting relation is

$$B_J = 16.8 - 0.086 \cdot \overline{\left(\frac{S}{N}\right)_{B_J}}. \tag{5}$$

Plate	Field	bgr	bgrnoise	N_{spc}
10882	540	1645	31.5	6
11535	823	1728	34.7	9
11552	826	1925	39.4	6
11576	827	1790	36.4	8
11578	825	1541	31.9	2
11579	759	1836	38.3	2
11588	605	1608	32.6	6
12024	195	1555	33.8	11
10144	155	559	18.1	11
10846	539	644	18.3	6
10847	757	688	18.3	9
10849	422	583	17.5	12
11621	154	673	19.7	7
11622	300	665	19.4	7
11623	199	494	17.5	8

Table 1: HES plates used for the investigation of the distribution of pixel-wise noise.

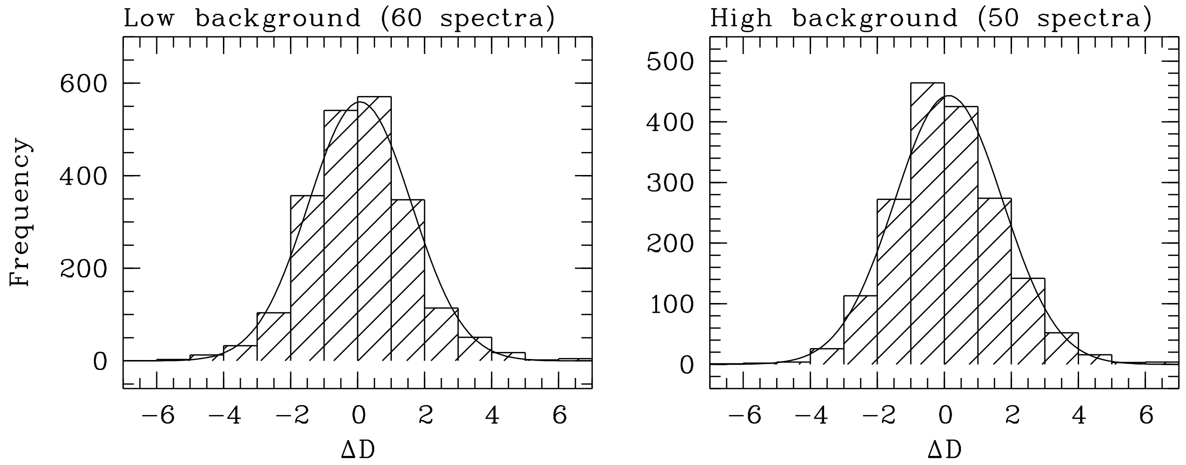

Figure 6: Distribution of pixel-wise noise in absorption line free regions of 60 spectra of A-type stars from 7 plates with low sky background (left panel), and 50 spectra from 8 plates with high background (right panel).

It has a 1σ error of 0.46^m. The large scatter is due to the fact that B_J for a given S/N can vary dramatically with plate background, and seeing. However, the purpose of the above relation is just to have a rough orientation of the B_J magnitude corresponding to a given S/N.

2.3 Candidate Selection

In the HES, the selection of candidates for any type of objects is carried out in two steps. In the first step, candidates are selected automatically by applying e.g. colour criteria, by automatic classification (see Sect. 3; see also Christlieb et al. 1997, 1998*a*,*b*), or other techniques. These candidates have to be

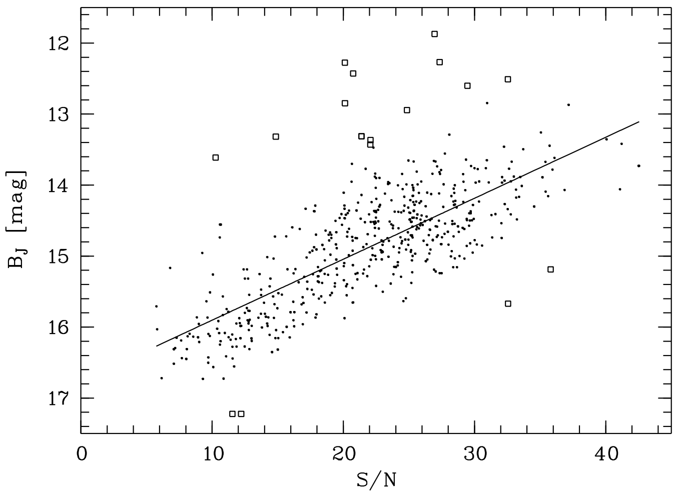

Figure 7: B_J as a function of average pixel-wise S/N in the B_J band. Open squares denote spectra that have been excluded from the fit by iterative 3σ clipping.

inspected manually to identify spectra which have been erroneously selected due to presence of plate artifacts (e.g. scratches, dust, emulsion flaws, ghosts, etc.). Moreover, a few overlaps escape detection by the automatic procedure, so that these spectra have to be rejected by hand. For these purposes, the program `screenspc` has been written. It displays the candidate spectra one by one, and the relevant regions of the direct plate and spectral plate scans upon request (see Fig. 8). With the help of the information being displayed on the screen, it is also possible to reproduce why the given spectrum has been automatically selected.

Acknowledgements

I would like to emphasize that the HES data base is the result of a team effort. The list of team members is too long to mention all of them here (however, see the footnote on p. 6). Special credits go to D. Reimers, the P.I. of the HES and L. Wisotzki for making the survey as successful as it is, the conception of the HES data reduction, and development of methods and algorithms for the exploitation of the data base.

References

Christlieb, N. (1995), Automatische Klassifikation von digitalisierten Objektivprismen-Platten, Diplomarbeit, Universität Hamburg.

Christlieb, N., Graßhoff, G., Nelke, A. & Wisotzki, L. (1997), Automatic classification of digitized objective prism spectra, *in* E. Kontizas, M. Kontizas, D. Morgan & G. Vettolani, eds, 'Wide-Field Spectroscopy', Kluwer, Dordrecht, pp. 109–113.

Christlieb, N., Graßhoff, G., Nelke, A., Schlemminger, A. & Wisotzki, L. (1998*a*), Automatic spectral classification, *in* I. Balderjahn, R. Mathar & M. Schader, eds, 'Classification, Data Analysis, and Data Highways', Springer, Berlin, pp. 16–23.

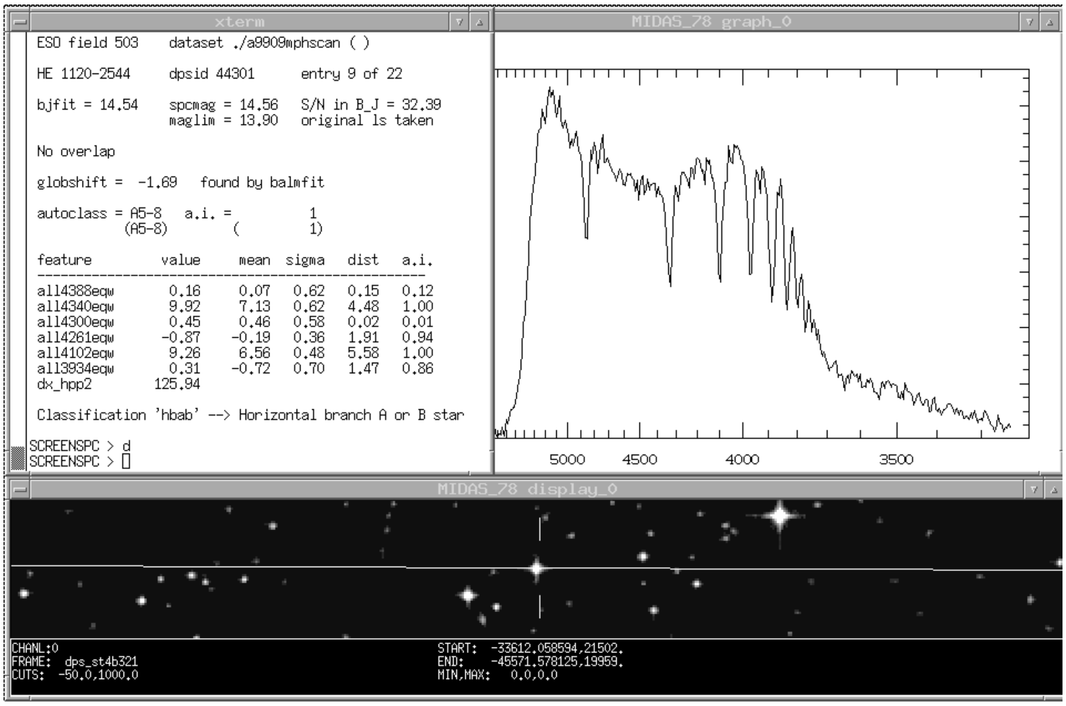

Figure 8: Screen-dump of the program `screenspc`, adapted for automatically classified spectra, in action. The information displayed in the upper left window allows to reproduce why the given spectrum has been assigned to its class (in this case class "A5-8") by automatic classification. In the upper right window the spectrum is shown. In the lower window the relevant regions of the direct plate and spectral plate scans can be displayed upon request in order to identify overlapping spectra and plate artifacts. The white line in the direct plate image corresponds to the dispersion direction of the spectral plate. In the middle, marked with vertical lines, the object under investigation can be seen. Direct and spectral image are displayed on the same scale.

Christlieb, N., Graßhoff, G., Nelke, A., Schlemminger, A. & Wisotzki, L. (1998*b*), Linné, a software system for automatic classification, *in* R. Albrecht, R. Hook & H. Bushouse, eds, 'Astronomical Data Analysis and Software Systems VII', Vol. 145 of *ASP Conf. Ser.*, pp. 457–460.

Deutsch, E. W. (1994), 'Positions and Proper Motions of Dwarf Carbon Stars', *PASP* **106**, 1134–1137.

Dickey, J. & Lockman, F. (1990), 'H I in the Galaxy', *ARA&A* **28**, 215–261.

Hagen, H.-J. (1987), Automatisches Suchen von Quasar-Kandidaten auf Objektivprismen-Platten, PhD thesis, Universität Hamburg.

Hewett, P. C., Foltz, C. B. & Chaffee, F. H. (1995), 'The Large, Bright QSO Survey. VI. Quasar Catalog and survey parameters', *AJ* **109**, 1498–1521.

Ikonomou, M. (1995), Untersuchung der Umgebung von Seyfert-Galaxien, Diplomarbeit, Universität Hamburg, Hamburg.

Köhler, T. (1991), Interne Helligkeitskalibration von Objektivprismenplatten, Diplomarbeit, Universität Hamburg, Hamburg.

Vanelle, C. (1996), Photometrische Eichung von Schmidtplatten, Diplomarbeit, Universität Hamburg, Hamburg.

Wisotzki, L., Christlieb, N., Bade, N., Beckmann, V., Köhler, T., Vanelle, C. & Reimers, D. (2000), 'The Hamburg/ESO survey for bright QSOs. III. A large flux-limited sample of QSOs', A&A, in press.

Wisotzki, L., Köhler, T., Groote, D. & Reimers, D. (1996), 'The Hamburg/ESO survey for bright QSOs I. Survey design and candidate selection procedure', *A&AS* **115**, 227–233.

3 Automatic Spectral Classification

The main goal of automatic classification in the HES is to identify objects of a certain class in its large data base. More formally, the problem can be stated as follows. The HES data base of digital spectra can be represented by feature vectors $\vec{x}$, consisting of a set of continuous values x_i, i.e.

$$\vec{x} = (x_1, \ldots, x_d),$$

where d is the number of features used. In Sect. 3.2 we describe how features are derived from HES spectra. We want to construct a *decision rule* which allows to assign a spectrum with feature vector $\vec{x}$ to one of the n_c classes Ω_j, $j = 1 \ldots n_c$, defined in the specific classification context. That is, we want to carry out a *supervised* classification, as opposed to *un supervised* classification, where the aim is to group objects into classes *not* defined before the classification process.

For supervised classification a *learning sample* is always needed. For our purposes, we define a learning sample to be a set of n_{ls} objects for which the feature vectors are known,

$$\{\vec{x}\} = (\vec{x}_1, \ldots, \vec{x}_{n_{ls}}),$$

and for which the *real* classes are known. The real classes can be defined e.g. by grouping a set of objects according to their stellar parameters (e.g. $T_{\rm eff}$, $\log g$, [Fe/H]), or by assigning classes to a set of spectra by comparison with reference objects. With the help of a learning sample, information on the class-conditional probability densities

$$p(\vec{x}|\Omega_j)$$

can be gained. $p(\vec{x}|\Omega_j)d\vec{x}$ is the probability to observe a feature vector in the range $\vec{x} \ldots \vec{x} + d\vec{x}$ in the class Ω_j. Experience has shown that in most HES applications it is appropriate to model $p(\vec{x}|\Omega_j)$ by multivariate normal distributions, i.e.,

$$p(\vec{x}|\Omega_j) = \frac{1}{(2\pi)^{d/2}\sqrt{|\Sigma_j|}} \exp\left\{-\frac{1}{2}\,(\vec{x}-\vec{\mu}_j)\,\Sigma_j^{-1}\,(\vec{x}-\vec{\mu}_j)'\right\}, \quad (6)$$

where j denotes class number, $\vec{\mu}_j$ the mean feature vector of class Ω_j, and Σ_j the covariance matrix of class Ω_j.

In many applications of automatic spectral classification in the HES, it is not possible to generate a large enough learning sample from *real* spectra present on HES plates. This is because usually the target objects are very rare. Therefore, we have developed methods to generate *artificial* learning samples by simulations, using either model spectra, or slit spectra. The next section is devoted to a description of the procedures involved.

3.1 Simulation of Objective-Prism Spectra

The conversion of model spectra, or slit spectra, to objective-prism spectra consists of 5 steps:

(1) Rebinning to the non-equidistant pixel size according to the global dispersion relation (Eq. 3)

(2) Multiplication with the HES spectral sensitivity curve(s)

(3) Smoothing with a Gaussian filter, for simulation of the seeing profile

(4) Adding of pixel-wise, normally distributed noise

(5) Random shift of the simulated spectrum according to the error distribution of the wavelength calibration zero point ($\pm 10\mu$ m).

Step (4) ensures that objects of any brightness can be simulated; the average brightness corresponding to a given S/N can be derived from Eq. (5).

3.1.1 HES Spectral Sensitivity Curves

Spectral sensitivity curves (SSCs) for HES plates have been determined by comparison of white dwarf model spectra, rebinned to the wavelength dependent pixel size $\Delta\lambda$ of the objective-prism spectra, with objective-prism spectra of DA white dwarfs on HES plates. A first implementation of such a procedure was done by von Laar (1995). The DA model spectra were fitted to slit spectra of each of the white dwarfs under comparison. We do not use the slit spectra directly as reference, because slit losses would produce erroneous results.

By comparing SSCs for plates from different plate batches, with different sky background, and generated with objects spanning a wide brightness range (but below the saturation threshold), we investigated the possible systematic influence of these characteristics on the shape of the SSCs. The parameters of the 12 objects used in this investigation, and plate parameters, are listed in Tab. 2.

Name	B_J	Plate	`bgr`	Batch	$T_{\rm eff}$ [K]	$\log g$
HE 0004-5403	16.2	12076	1123	1D4	18200 ± 300	8.26 ± 0.06
HE 0059-5701	16.4	12052	1026	1D4	30400 ± 300	8.08 ± 0.06
HE 0252-3501	16.0	11420	1039	1D4	17400 ± 300	7.35 ± 0.05
HE 0358-5127	15.4	10844	765	1I3	24100 ± 300	8.10 ± 0.05
HE 0409-5154	16.1	10844	765	1I3	27500 ± 300	8.00 ± 0.06
HE 0412-4744	16.5	10844	765	1I3	19300 ± 300	8.08 ± 0.06
HE 0418-5326	16.1	10939	649	1I3	27900 ± 200	8.00 ± 0.05
HE 1049-1552	14.2	9091	752	1C8	20200 ± 200	8.63 ± 0.04
HE 1058-1258	14.8	9091	752	1C8	24700 ± 200	8.84 ± 0.04
HE 1058-1334	16.6	9091	752	1C8	15900 ± 300	8.00 ± 0.07
HE 1017-1618	15.8	8402	1363	1K6	28600 ± 300	8.30 ± 0.06
HE 1017-1352	14.4	8402	1363	1K6	33500 ± 200	8.25 ± 0.05

Table 2: Sample of DA white dwarfs used for determination of spectral sensitivity curves. `bgr` is the diffuse background (in counts) averaged over four plate quarters.

By comparing the shapes of the 12 resulting SSCs, we found that there is *no* systematic influence of object brightness, plate batch and sky background on SSC shape. The plate material of the HES is astonishingly homogenous as compared to other surveys, e.g. the other Hamburg based objective prism survey, the HQS Hagen et al. (1995). However, a *slight* variation of SSC shape is present (see Fig. 9), which hence must be attributed to another parameter. Since it is the blue part of the SSCs that varies, it is very likely that the time span between hypersensitization and development of the plate is responsible for the shape variations.

We grouped the 12 SSCs into 4 SSC classes of similar shape (see Tab. 3), and averaged them within these classes. When converting model spectra or slit spectra to objective prism spectra, we use an SSC created by averaging the 4 averaged SSCs with randomly assigned weights.

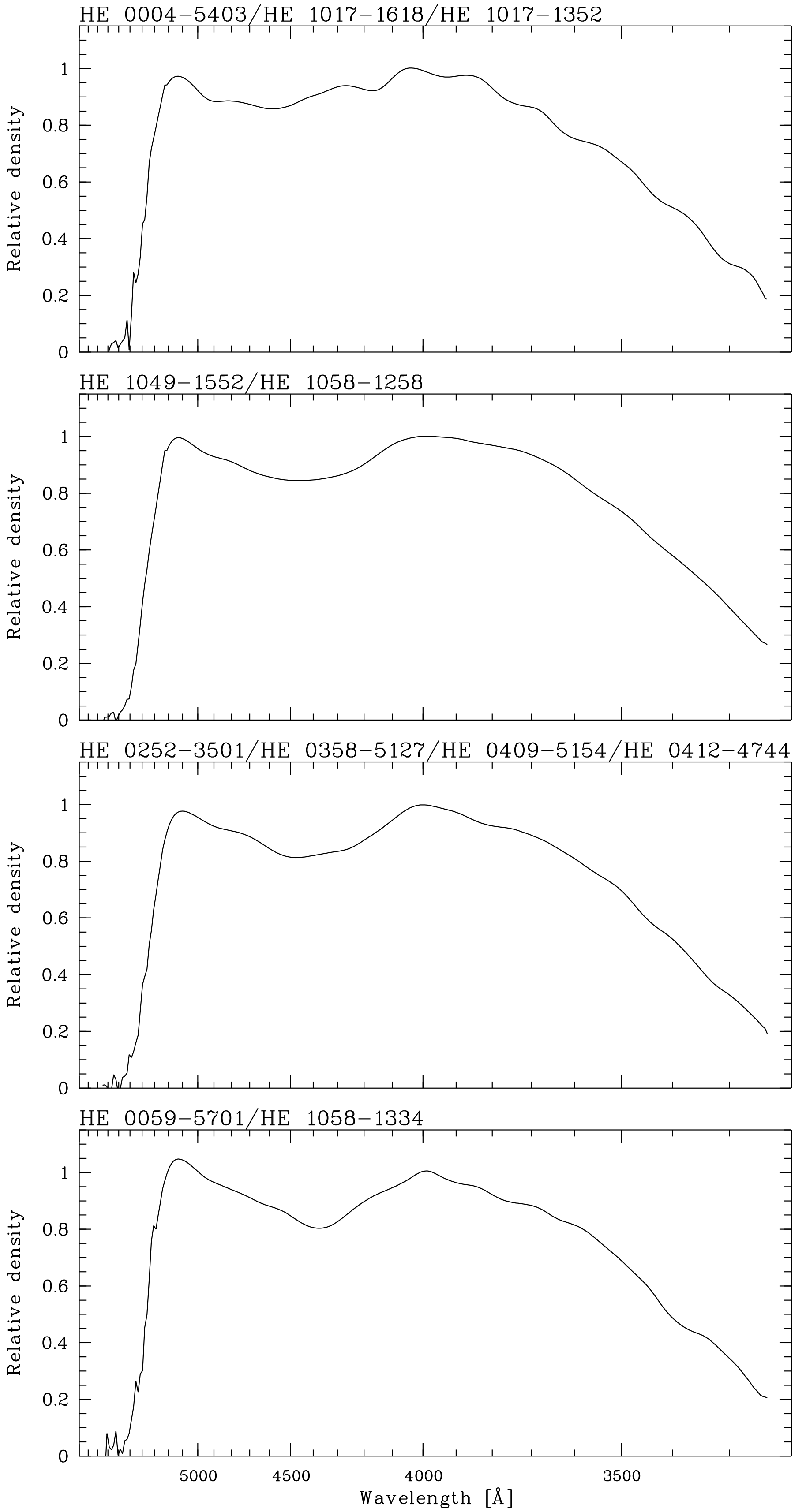

Figure 9: Averaged spectral sensitivity curves.

#	Name	B_J	Plate	bgr	Batch
1	HE 0004-5403	16.2	12076	1123	1D4
1	HE 1017-1618	15.8	8402	1363	1K6
1	HE 1017-1352	14.4	8402	1363	1K6
2	HE 1049-1552	14.2	9091	752	1C8
2	HE 1058-1258	14.8	9091	752	1C8
3	HE 0252-3501	16.0	11420	1039	1D4
3	HE 0358-5127	15.4	10844	765	1I3
3	HE 0409-5154	16.1	10844	765	1I3
3	HE 0412-4744	16.5	10844	765	1I3
4	HE 0059-5701	16.4	12052	1026	1D4
4	HE 1058-1334	16.6	9091	752	1C8

Table 3: Averaging of spectral sensitivity curves of similar shape.

3.1.2 Adding Noise

We add artificial, normally distributed noise to the converted spectra, in order to simulate objective-prism spectra of any brightness. We parameterize the S/N of a spectrum by the mean S/N in the B_J band,

$$\overline{\left(\frac{S}{N}\right)}_{B_J} = \frac{1}{n}\sum_{i=1}^{n}\frac{D_i}{a_0 + a_1 D_i + a_2 D_i^2},$$

using the noise model described in Sect. 2.2.6. Since the noise depends on the density D, it is important to take care of the density variation throughout the spectrum. We thus scale the simulated spectra with a scaling factor c such that the desired mean S/N in B_J is achieved, when the appropriate amount of pixel-wise Gaussian noise is added. We use the typical noise coefficients

$$a_0 = 18.4 \quad (7)$$

$$a_1 = 0.604 \cdot 10^{-2} \quad (8)$$

$$a_2 = 0.719 \cdot 10^{-5}. \quad (9)$$

The mean S/N of the scaled spectrum is:

$$\overline{\left(\frac{S}{N}\right)}_{\text{new}} = \frac{1}{n}\sum_{i=1}^{n}\frac{c \cdot D_i}{a_0 + a_1 \cdot c \cdot D_i + a_2 \cdot c^2 \cdot D_i^2}, \quad (10)$$

For the determination of c we re-arrange this equation to:

$$\frac{1}{n}\sum_{i=1}^{n}\frac{c \cdot D_i}{a_0 + a_1 \cdot c \cdot D_i + a_2 \cdot c^2 \cdot D_i^2} - \overline{\left(\frac{S}{N}\right)}_{\text{new}} = 0 \quad (11)$$

Eq. (11) can be solved iteratively with the Newton-Raphson method. The iteration rule is:

$$c^{(m+1)} = c^{(m)} - \frac{f(c^{(m)})}{f'(c^{(m)})}, \quad (12)$$

where $f(c)$ is the left hand side of Eq. (11). A comparison of simulated spectra with real spectra is shown in Fig. 10.

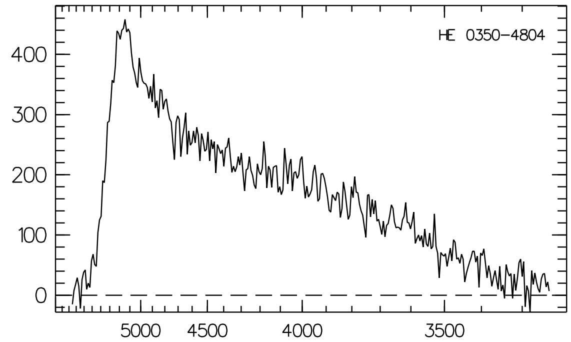

(a) Metal-poor halo star HE 0350-4804.

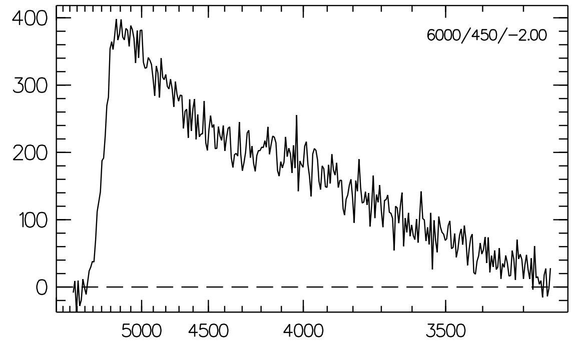

(b) Model spectrum of a metal poor star with the same stellar parameters as HE 0350-4804, converted to objective-prism spectrum and with added artificial noise.

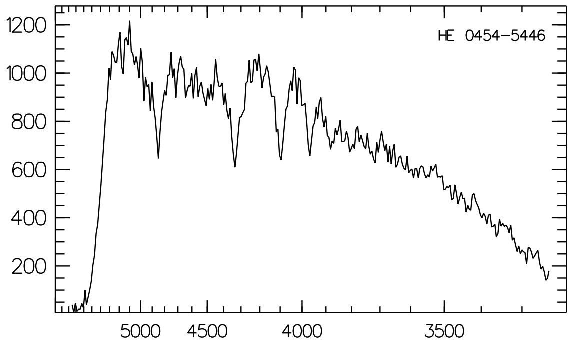

(c) HE 0454-5446, white dwarf of type DA.

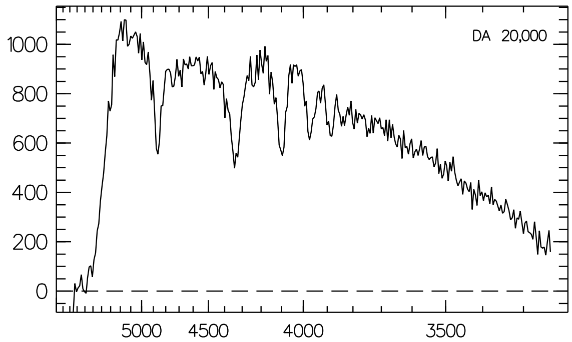

(d) Model spectrum of a DA with $T_{\rm eff} = 20\,000$ K, converted to objective-prism spectrum and with added artificial noise.

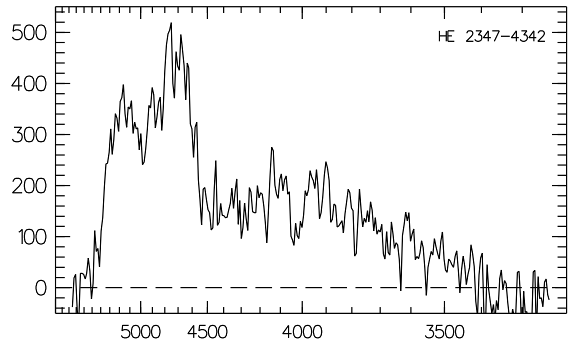

(e) Quasar HE 2347-4342, $z = 2.89$.

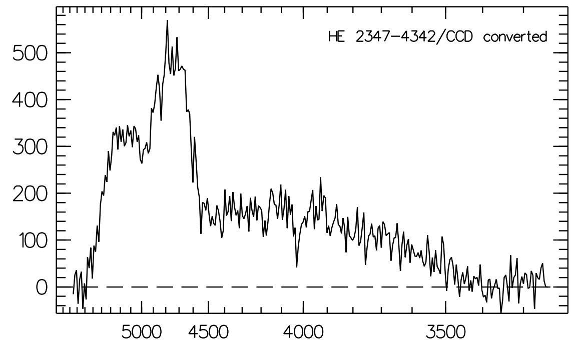

(f) Slit spectrum of HE 2347-4342, converted to objective-prism spectrum and with added artificial noise.

Figure 10: HES spectra of objects of different type (left column) in comparison with simulated objective-prism spectra (right column). The units of the ordinates are densities in arbitrary units.

Since a lower S/N results in a larger scatter of feature values x_i within each class, the parameters of the class-conditional probabilities Eq. (6) are determined independently for artificial learning samples of different S/N. We use the following S/N grid:

$$\overline{\left(\frac{S}{N}\right)_{B_J}} = 5, 10, 15, 20, 25, 30. \tag{13}$$

Each spectrum is then classified by using the learning sample with a S/N which is closest to the S/N of the spectrum; e.g. a spectrum with $S/N = 18$ is classified by using the learning sample with $S/N = 20$.

3.2 Feature Detection

It is critical for automatic classification to have a set of *reliable* features at hand. The total set of available features should contain as much information of the objects to be classified as possible.

A wide range of spectral features is automatically detected from the digitized objective-prism spectra during the data reduction process (see Tab. 4): stellar absorption and emission lines, continuum shape, Calcium-break, bisecting points of spectral density distribution, C_2 and CN band indices, and a Ca K line index.

Name	Description	Detection method
`all5160eqw`	W_λ of Mg I b triplett/TiO λ 5168	Iterative fit procedure
`all4861eqw`	W_λ of Hβ	Iterative fit procedure
`all4388eqw`	W_λ of Fe I λ 4383+85	Iterative fit procedure
`all4340eqw`	W_λ of Hγ	Iterative fit procedure
`all4300eqw`	W_λ of G-Band	Iterative fit procedure
`all4261eqw`	W_λ of Cr I λ 4254 + 75 + Fe I 4260 + 72	Iterative fit procedure
`all4227eqw`	W_λ of Ca I λ 4227	Iterative fit procedure
`all4102eqw`	W_λ of Hδ	Iterative fit procedure
`all3969eqw`	W_λ of Ca H + Hε	Iterative fit procedure
`all3934eqw`	W_λ of Ca K	Iterative fit procedure
`klcomp_1`	1. continuum shape coefficient	PCA
`klcomp_2`	2. continuum shape coefficient	PCA
`klcomp_3`	3. continuum shape coefficient	PCA
`klcomp_4`	4. continuum shape coefficient	PCA
`CaBreak_sn`	S/N Calcium-break	Template matching
`CaBreak_cont`	Contrast of Calcium-break to continuum	Template matching
`CaKindex`	Strength of Ca K	Ratio of average pixel values
`C2idx1`	Strength of C_2 λ5165	Ratio of average pixel values
`C2idx2`	Strength of C_2 λ4737	Ratio of average pixel values
`CNidx2`	Strength of CN λ4216	Ratio of average pixel values
`CNidx3`	Strength of CN λ3883	Ratio of average pixel values
`dx_hpp1`	Half power point distance 1	Summing of pixel values
`dx_hpp2`	Half power point distance 2	Summing of pixel values

Table 4: Automatically detected spectral features in the HES.

3.2.1 Detection of Stellar Lines

We implemented a flexible, robust algorithm which allows to detect stellar absorption and/or emission lines in HES spectra. The algorithm is iterative, consisting of the following steps:

(1) Determination of continuum by filtering with a wide median filter and narrow Gaussian filter.

(2) Improvement of determination of the wavelength calibration zero point by fitting of 3 sets stellar lines. The sets contain the strongest stellar absorption lines of early type, solar type, and late type stars, respectively. The individual lines depths, and the zero point offset of wavelength calibration are fitted simultaneously. The *relative* positions of the stellar lines are held fixed, and the line *widths* is held fixed at the value of the seeing profile widths, which is measured during spectral extraction. The set of lines giving the strongest signal, i.e. largest average equivalent widths, is selected, and the wavelength calibration zero point determined with that fit is adopted.

(3) Improvement of continuum determination:

  (a) Fitting of *all* stellar lines detectable in HES spectra

  (b) Removal of fitted lines from the original spectrum

  (c) Computation of improved continuum by filtering the line-reduced spectrum again with a wide median filter and narrow Gaussian filter

  (c) Start with (3a), if $n_{\rm iter} < 3$; otherwise compute rectified spectrum with final continuum.

(4) Fitting of all stellar lines in the rectified spectrum by Gaussians.

For each spectral line it can be chosen whether it is to be detected in absorption or emission. The output of the fit algorithm are equivalent width, FWHM and S/N of the lines, and shift of the wavelength calibration zero point. Any spectral lines not yet considered can easily be included by just adding its wavelength to the list of lines to be fitted.

3.2.2 PCA of Continua

We perform a Principal Component Analysis (PCA; see e.g. Murtagh & Heck 1987) of the continua determined in the iterative line detection procedure, in order to parameterize the continuum shape of HES spectra. Wisotzki (1991) used PCA in the HES also for quasar selection.

It was found that for the continua of a learning sample of 654 spectra classified by hand, and occupying the classes A5–K9, three principal components account for almost 98 % of the variance in the learning sample. It was possible to fit the continua of almost all of the learning sample spectra with $\chi^2/\nu < 2.0$. Four objects needed 5 or more components. Their spectra were inspected again and it was found that they have an unusual continuum shape, probably because they are binaries. These spectra have thus been excluded from the learning sample.

3.2.3 Broad Band Colours

For many stellar applications it is helpful to have $U-B$ and $B-V$ colours at hand. Therefore, we established colour calibrations using so-called "half power points" (hpp; see Wisotzki et al. 2000). These are bisecting points of a part of the spectrum. Definitions of the hpps can be found in Tab. 5, and an illustration in Fig. 12. hpps are equivalent to broad band colours, but have the advantage of being more robust against noise. `x_hpp1` and `x_hpp2` are well correlated with $U-B$ and $B-V$, respectively.

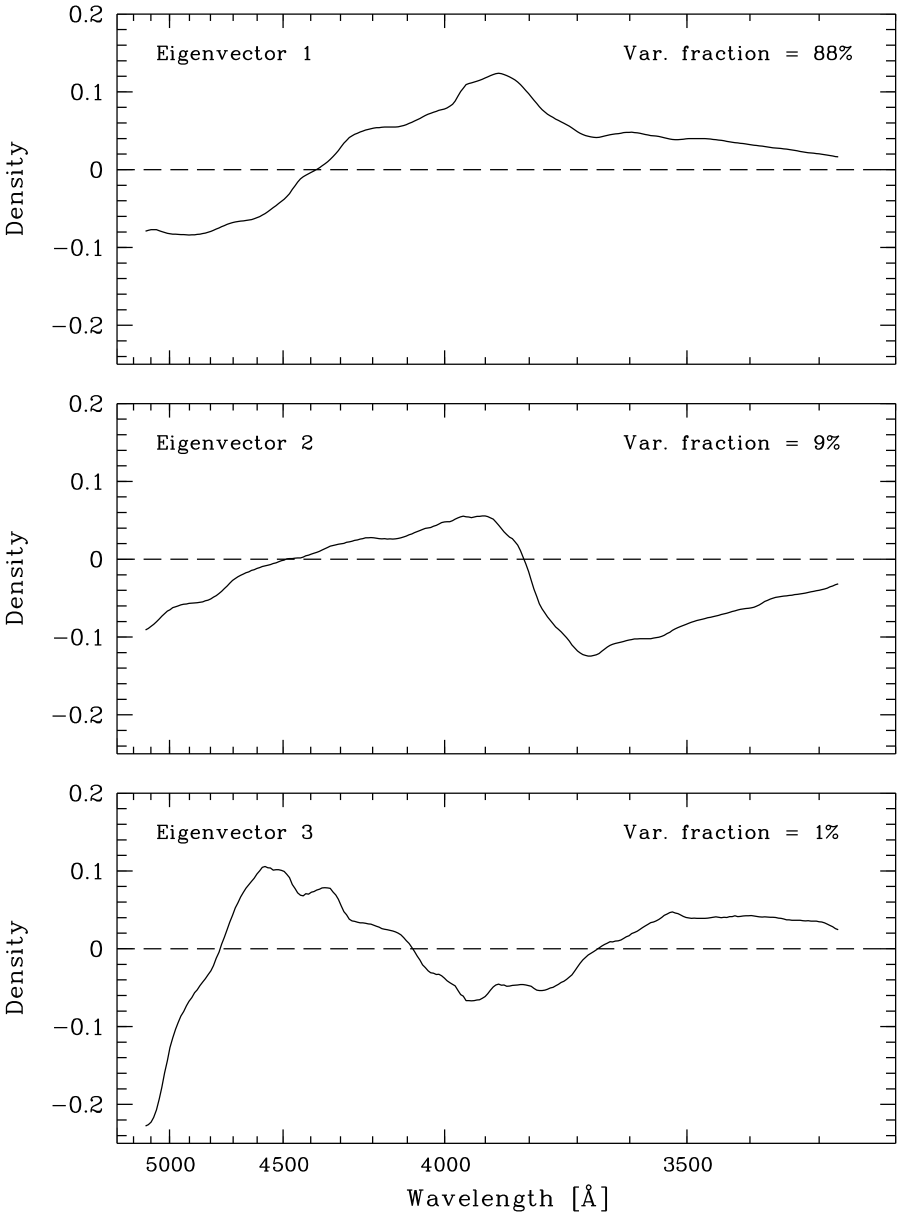

Figure 11: First three principal components of the continua of 654 learning sample spectra.

Name	λ range	correlated with
x_hpp1	$3240\,Å < \lambda < 4840\,Å$	$U-B$
x_hpp2	$3890\,Å < \lambda < 5360\,Å$	$B-V$

Table 5: Definitions of spectral half power points (hpp) used in the HES.

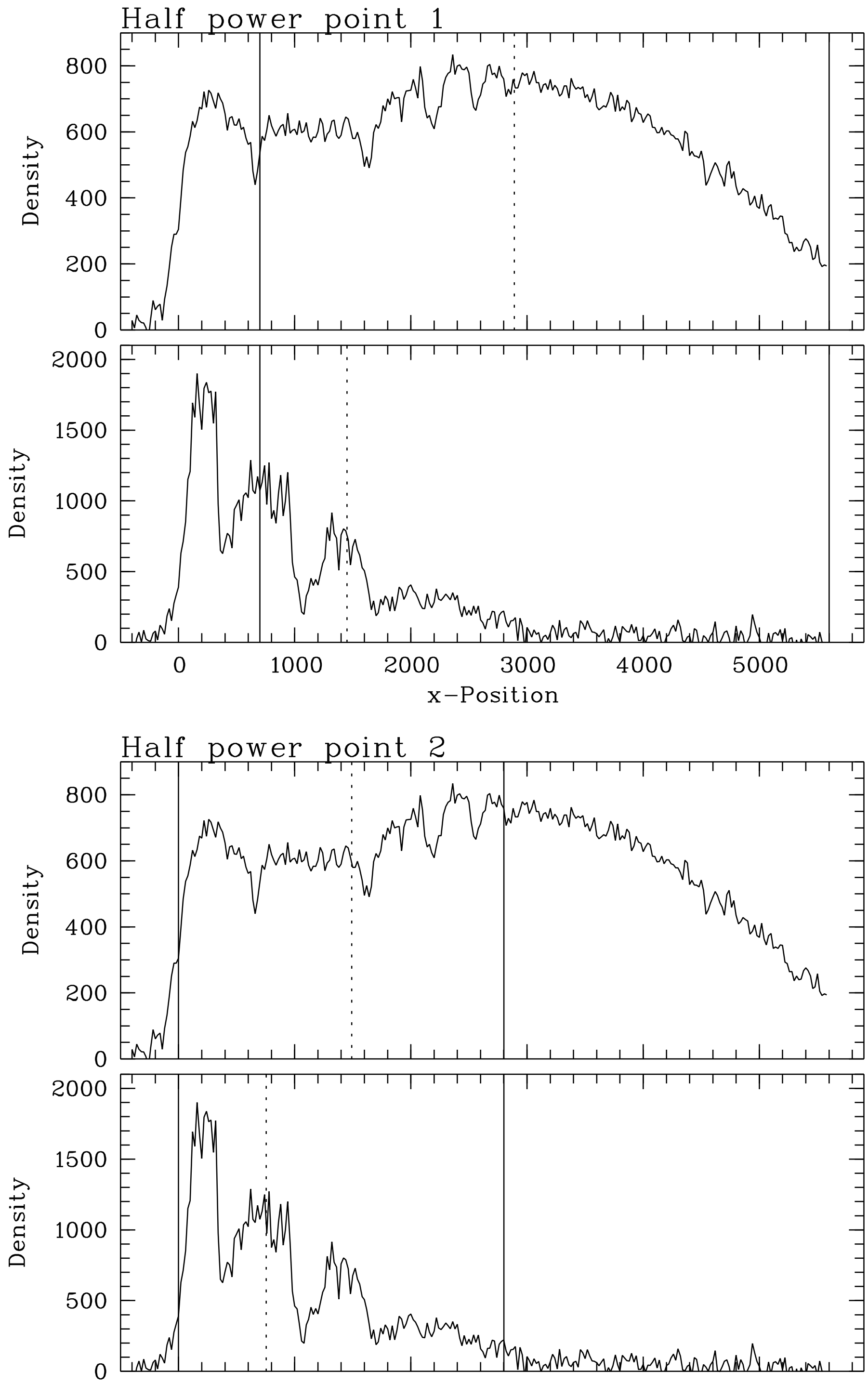

Figure 12: Illustration of spectral half power points x_hpp1 and x_hpp2. Solid lines mark the regions in which the hpps are computed; dotted lines indicate the position of the hpps.

A more precise colour calibration can be achieved when distances `dx` to a cutoff line in a colour-magnitude diagram (see Fig. 13) is used instead of `x` values for the bisecting point, because plate-to-plate variations of the spectral sensitivity curves are compensated in this way. The cutoff line separates the bulk of "normal" stars from UV-excess objects (or objects with unusually low $B-V$ in case of `dx_hpp2`). The cutoff is determined by a break finding algorithm.

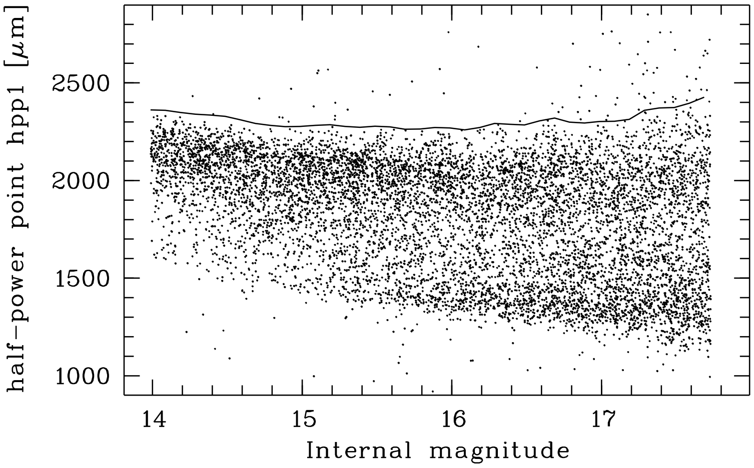

Figure 13: Cutoff-line for bisecting point `x_hpp1` on one HES plate.

Because the blue end of the HES spectra is sensitive to contamination by overlaps, special care must be taken to exclude such spectra from the calibration of `dx_hpp1`. This has been done by applying stricter overlap selection criteria. In addition, an iterative $\kappa\sigma$-clipping with $\kappa = 3$ has been employed to exclude overlaps unrecognized by the automatic detection. 50 of the 623 spectra in the original data set have been clipped out, so that the calibration uses spectra of 573 objects. The resulting fit is shown in Fig. 14.

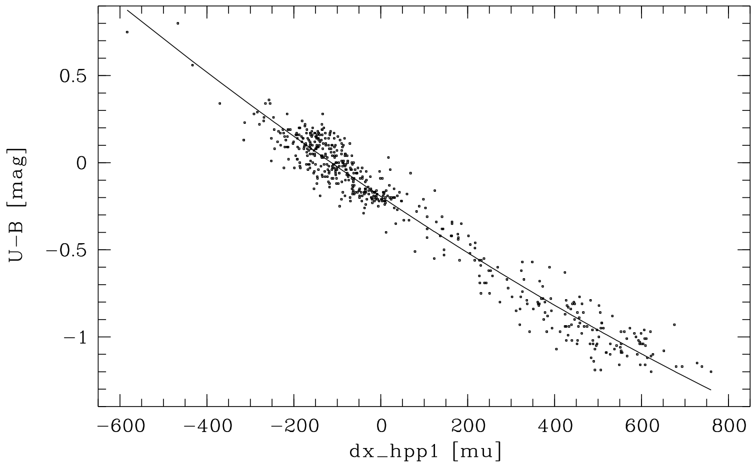

Figure 14: Calibration of `dx_hpp1` using a combined sample of 573 objects from the EC and HK surveys present on HES plates.

A potential problem for the $B-V$ calibration is that the V band is not fully covered by the HES wavelength range. Therefore, the calibration for very red objects is inaccurate, or even impossible. As calibrators for red objects, 36 carbon stars have been used, for which BV photometry was obtained by the author at the ESO 2.2 m telescope in April 1999. Carbon stars with $B-V > 2.5$ have been excluded from the fit. For $B-V \lesssim 1.0$, 778 stars from the HK survey of Beers et al. (1992), 354 FHB and other A-type stars of Wilhelm et al. (1999), and 272 objects from the northern galactic cap fields of the EC survey (Kilkenny et al. 1997) present on HES plates have been used. Linear fits in three colour regions have been done separately, in order to evaluate the scatter independently, and check consistency. Then, a combined fit to all 1256 unique objects was done (see Fig. 15).

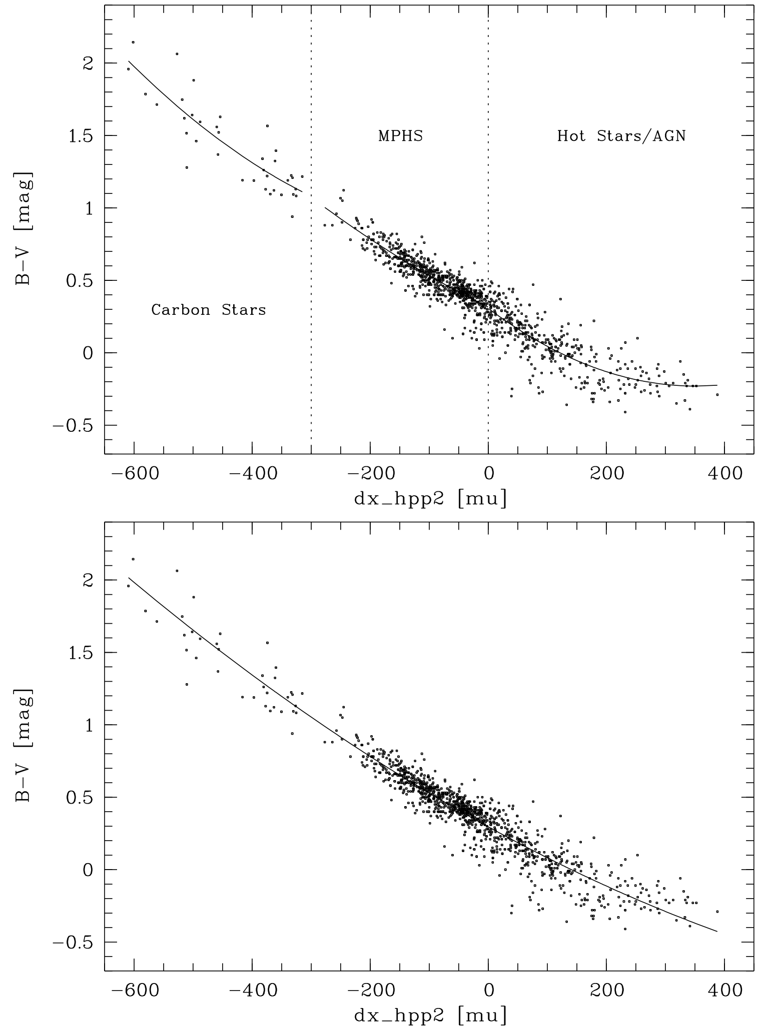

Figure 15: Calibration of dx_hpp2 by separate fits in different colour regions (upper panel), and by combined fit to 1256 objects (lower panel).

The results of the fits are summarized in Tab. 6. Note that a single fit contains objects from a large fraction of the 329 stellar HES plates, and – with the exception of the red $B-V$ fit – a wide range of object types, e.g. metal-poor stars, solar metallicity F- and G-type stars, field horizontal branch A-type stars, "normal" A-type stars, DA white dwarfs, DB white dwarfs, sdB stars, AGN. The achieved accuracies are $\sigma_{U-B} = 0.092^m$, and $\sigma_{B-V} = 0.095^m$ for the $B-V$ fit using all calibration objects together. The accuracy in $B-V$ for red ($B-V \gtrsim 1$) and blue ($B-V \lesssim 0.3$) objects is a factor of ~ 2 worse ($\sigma = 0.15^m$ and 0.12^m, respectively) than for intermediate $B-V$ objects ($\sigma = 0.074^m$).

Colour	a_0	a_1	a_2	valid range	N_{stars}	σ [mag]
$B-V$	0.79	$2.53 \cdot 10^{-5}$	$3.34 \cdot 10^{-6}$	$-600 <$ dx_hpp2 < -300	37	0.15
$B-V$	0.31	$-2.00 \cdot 10^{-3}$	$1.74 \cdot 10^{-6}$	$-300 <$ dx_hpp2 < 0	817	0.074
$B-V$	0.31	$-3.06 \cdot 10^{-3}$	$4.35 \cdot 10^{-6}$	$0 <$ dx_hpp2 < 400	405	0.12
$B-V$	0.30	$-2.24 \cdot 10^{-3}$	$9.62 \cdot 10^{-7}$	$-600 <$ dx_hpp2 < 400	1259	0.095
$U-B$	-0.19	$-1.67 \cdot 10^{-3}$	$+2.76 \cdot 10^{-7}$	$-800 <$ dx_hpp1 $< +800$	573	0.092

Table 6: Broad band colour calibration fits.

3.2.4 Narrow Band Colours

We obtain Strömgren coefficients $c_1 = (u-b) - (v-b)$ directly from HES spectra by averaging the density in the Strömgren *uvb* bands, and computing internal coefficients $c_{1,\mathrm{HES}}$ from that. $c_{1,\mathrm{HES}}$ has been calibrated using a total of 79 stars, which are not saturated in the HES, from three different sources. 22 metal-poor stars have been taken from Schuster et al. (1996), 43 stars from Beers (2000, priv. comm.), of which 2 have been rejected as outliers (see Fig. 16), and 16 hot subdwarfs from an updated version of the catalog of Kilkenny et al. (1988) (Heber 2000, priv. comm.). The 1σ error of the calibration is 0.15^m. c_1 can be used as a gravity indicator, since it measures the strength of the Balmer discontinuity.

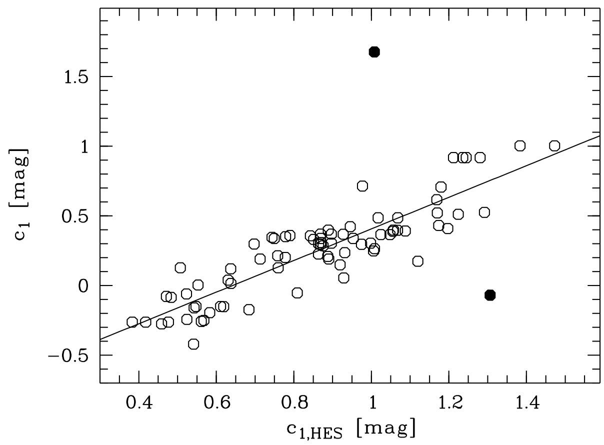

Figure 16: Calibration of Strömgren c_1 measured in HES spectra. The 2 filled circles mark objects excluded from the fit.

3.3 Decision Rules

A central issue in automatic classification is the construction of a decision rule which is optimal for the given classification problem. In the HES, we use two decision rules: The Bayes rule, and a minimum cost rule.

3.3.1 Bayes' Rule

Classification with Bayes' rule minimizes the total number of misclassifications, if the *true* distribution of class-conditional probabilities $p(\vec{x}|\Omega_i)$ is used (Hand 1981; Anderson 1984). Using Bayes' theorem,

$$P(\Omega_i|\vec{x}) = \frac{P(\Omega_i)\,p(\vec{x}|\Omega_i)}{\sum_{\forall i} P(\Omega_i)\,p(\vec{x}|\Omega_i)},$$

posterior probabilities $p(\Omega_i|\vec{x})$ can be calculated. A spectrum of unknown class, with given feature vector $\vec{x}$, can then be classified using Bayes' rule:

Bayes' rule: *Assign a spectrum with feature vector $\vec{x}$ to the class with the highest posterior probability $p(\Omega_i|\vec{x})$.*

3.3.2 Minimum Cost Rule

In most of the classification problems arising in the HES it is desired to compile a sample of objects of a specific class, or a specific *set* of classes. In these cases, Bayes' rule is not appropriate, because we do not want to minimize the total number of misclassifications, but the misclassifications between the desired class(es) of objects, and the remaining classes. Suppose we have three classes, A-, F-, and G-type stars, and we want to compile a complete sample of A-type stars. Then only misclassifications between A-type stars and F- and G-type stars (and vice versa) are of interest. More specifically, misclassifications of A-type stars to F- and G-type stars (leading to incompleteness) are least desirable when a complete sample shall be compiled, and erroneous classification of F- and G-type stars as A-type stars (resulting in sample contamination) can be accepted at a moderate rate. Misclassifications between F- and G-type stars can be totally ignored, because the target object type is not involved.

Classification aims like this can be realized by using a minimum cost rule. Cost factors r_{hk}, with

$$0 \le r_{hk} \le 1; \qquad h = 1,\ldots,n_c; \quad k = 1,\ldots,n_c. \tag{14}$$

allow to assign *relative weights* to individual types of misclassifications. The cost factor r_{hk} is the relative weight of a misclassification from class Ω_h to class Ω_k.

Suppose we have an object of unknown class, with feature vector $\vec{x}$. We ask how large the cost is if it belongs to class Ω_h, and would be assigned to class Ω_k, $h \neq k$. The cost $C_{h\to k}(\vec{x})$ is:

$$\begin{aligned} C_{h\to k}(\vec{x}) &= r_{hk} P(\Omega_h|\vec{x}) \\ &= r_{hk} \frac{P(\Omega_h)\,p(\vec{x}|\Omega_h)}{\sum\limits_{i=1}^{m} P(\Omega_i)\,p(\vec{x}|\Omega_i)} \\ &= r_{hk} \frac{a_h p_h(\vec{x})}{\sum\limits_{i=1}^{m} a_i p_i(\vec{x})}. \end{aligned}$$

In the last step we have used the abbreviations $P(\Omega_h) = a_h$ and $p(\vec{x}|\Omega_h) = p_h(\vec{x})$. We do not know to which of the possible classes Ω_h, $h = 1,\ldots,n_c$, the object actually belongs. Therefore, we estimate the expected cost $C_k(\vec{x})$ for assigning an object with feature vector $\vec{x}$ to the class Ω_k by computing the following sum of costs:

$$C_k(\vec{x}) = \sum_{\substack{h=1 \\ h\neq k}}^{m} C_{h\to k}(\vec{x})$$

$$= \sum_{\substack{h=1 \\ h \neq k}}^{m} r_{hk} \frac{a_h p_h(\vec{x})}{\sum_{i=1}^{m} a_i p_i(\vec{x})} \qquad (15)$$

Now we can formulate the minimum cost rule, which minimizes the total cost (Hand 1981).

Minimum Cost Rule: *Assign an object with feature vector $\vec{x}$ to the class Ω_k with the lowest expected cost $C_k(\vec{x})$.*

If the cost factors have been chosen such that

$$r_{hk} \equiv \delta_{hk},$$

the minimum cost rule classification is identical to classification according to Bayes' rule. In this case the cost for assigning the class Ω_k to a spectrum with feature vector $\vec{x}$ is the probability that the object belongs to one of the other classes $h \neq k$. This follows immediately from Eq. (15). If $r_{hk} \neq \delta_{hk}$, the total number of misclassifications is *not* minimized, so that the quality of a minimum cost rule classification has to be evaluated by other criteria.

3.3.3 Rejection Rule

Non-mathematically speaking, Bayes' rule assigns the class with the highest *relative* resemblance to each spectrum to be classified. However, it is ignorant of the *absolute* resemblance: A spectrum with feature vector $\vec{x}$ may be assigned to a class with *very low* posterior probability $p(\Omega_i|\vec{x})$, if $p(\Omega_i|\vec{x})$ is even lower for all other classes. This means that a class is assigned to *all* spectra, even to "garbage spectra" which have been disturbed, for instance, by plate artifacts. Therefore, it is useful to make use of a rejection criterion.

Reject rule: *Reject an object from classification to class Ω_i, if $a.i.(\Omega_i;\vec{x}) > \beta$.*

The parameter β is a threshold to be chosen, and the parameter $a.i.$ is the *atypicality index* suggested by Aitchison et al. (1977),

$$a.i.(\Omega_i,\vec{x}) = \Gamma\left\{\frac{d}{2};\frac{1}{2}\,(\vec{x}-\vec{\mu}_i)\,\Sigma_i^{-1}\,(\vec{x}-\vec{\mu}_i)'\right\},$$

where $\Gamma(a;x)$ is the incomplete gamma function and d the number of features used for classification. Use of the above rejection criterion is identical to performing a χ^2 test of the null hypothesis H_0 that an object with feature vector $\vec{x}$ belongs to class Ω_i at significance level $1-\beta$, against the alternative hypothesis H_1 that it *does* belong to class Ω_i. We reject the null hypothesis, if its significance level is *low*, i.e., if it is very *un*likely that a feature vector $\vec{x}$ is observed for class Ω_i, given the multivariate normal distributions (6) are the *true* distributions of the class-conditional probabilities $p(\vec{x}|\Omega_i)$.

3.4 Evaluation of Classification Rules

Classification rules can be evaluated by the number of expected misclassifications (in case of Bayes' rule), or by the total expected cost (in case of the minimum cost rule). The three most important methods to estimate these numbers are (Deichsel & Trampisch 1985):

(1) Re-substitution

(2) “Hould out” method

(3) “Leaving one out” method.

Re-substitution means that one uses the learning sample also as test sample. The drawback of this method is that one *underestimates* the number of expected misclassifications, because a classification rule derived with the help of a finite learning sample is always adapted to the individual composition of the learning sample. Therefore, the estimation of the expected number of misclassification is biased (Deichsel & Trampisch 1985).

An improvement in this respect is gained when the “hold out” method is used. Here one randomly divides the learning sample disjunctly into a new, smaller learning sample, and a test sample. Since the learning sample and test sample are completely independent in this case, an unbiased estimate of the expected error rates is possible (Deichsel & Trampisch 1985). However, the drawback is that one needs a large enough learning sample. When modeling the class-conditional probabilities with multivariate normal distributions, the learning sample size has to be large enough to ensure a robust estimation of the parameters of the distributions. When using non-parametric methods, the situation is even worse, because the *shape* of the distribution has to be determined, too, so that additional degrees of freedom are present.

The problem of learning sample size can be circumvented by using the “leaving one out” method. Suppose we have a learning sample of size n_{ls}. We exclude object i from the learning sample, and construct the classification rule using the $n_{ls} - 1$ remaining objects. Object i is then classified with this classification rule. This procedure is repeated n_{ls} times, so that each object of the learning sample is excluded once, and used as test sample. By adding up the numbers of misclassifications obtained in each step, one gets an unbiased estimate of the expected error rate (Deichsel & Trampisch 1985). The only drawback of this method is that it consumes a lot more computing time than the previously mentioned methods, since n_{ls} classification rules have to constructed. However, the computing time increases only *linearily* with learning sample size n_{ls}, so that the usage of the “leaving one out” method was feasible for all HES learning samples used so far (the largest learning sample used had $n_{ls} = 165\,000$).

3.5 Choosing a Feature Combination

It is necessary to select a subset of the available features for each classification problem, and each S/N step, because of several reasons.

(1) Blended lines, e.g. Hε+Ca H, can confuse the classification.

(2) It is advantageous to exclude redundant features from the set of features used for classification, since the usage of less features results in more stable estimates of the parameters of the multivariate normal distributions Eq. (6).

(3) The optimal feature set can vary with S/N. For instance, at low S/N it can be useful to only use continuum shape parameters and colours for classification, because no stellar lines can be detected reliably anymore.

The best method for finding the optimal feature combination is to evaluate *all* $2^d - 1$ possible combinations of the d available features, since this is the only way to *prove* that the combination found is really the best one. However, since the computing time raises exponentially with the number of features, the complete search is only feasible for a limited number of features. On a Linux PC with 333 MHz Pentium II processor the complete search in a feature space of $d = 11$, evaluated with "leaving one out" on a learning sample of 22 500 objects, takes about one day. Since the search has to be done for all 6 S/N steps individually, $d = 11$ is about the feasibility limit.

In practice it is usually possible to select a subset of $d < 11$ features from the 23 available features listed in Tab. 4 by astrophysical considerations alone. E.g., when it is desired to select metal-poor stars, one can restrict the initial feature set to those features that are *possibly* useful as indicators for T_{eff}, $\log g$, and [Fe/H], and one can safely ignore e.g. Carbon band indices. It is also possible to reduce the dimensionality of the feature space by *a priori* combining redundant features, e.g. the equivalent widths of the Balmer lines to a *sum* of equivalent widths.

3.6 Choosing Cost Factors

The cost factors were adjusted by using a special tool, which displays the confusion matrix, estimated with the "leaving one out" method on the learning sample, depending on the choice of three sets of cost factors:

`t2o:` Cost factor for misclassification of an object of the **t**arget class (`'t'`) to (`'2'`) one of the **o**ther classes (`'o'`).

`o2t:` Cost factor for contamination of the target class.

`o2o:` Cost factor for misclassification between other classes.

Since sample completeness and contamination are interdependent, in practice only the *relative* value `t2o`/`o2t` has to be adjusted. A screen-dump of the cost factor tool is shown in Fig. 17.

Acknowledgements

The work described in this section was partly carried out in collaboration with the research group *Epistemische Systeme* lead by G. Graßhoff. Together with A. Nelke and A. Schlemminger, we critically discussed methods of automatic classification we found in the literature, and we developed many ideas during the legendary Saturday morning meetings, which never lasted less than 4 hours! A. Nelke has also implemented the cost factor adjusting tool.

I thank D. Homeier for fitting DA models to slit spectra, and V. Beckmann for obtaining a part of those at ESO. G. Pizarro kindly compiled a list of HES plate batches from the notes he made at the ESO Schmidt telescope.

Precise, photoelectric *UBV* and Strömgren *uvby* photometry for HK survey stars was kindly provided by T. Beers before publication. I thank D. O'Donoghue for making EC survey photometry in digital form available to me. U. Heber provided an updated version of the subdwarf catalog of Kilkenny et al. (1997).

References

Aitchison, J., Habbema, J. & Kay, J. (1977), 'A Critical Comparison of Two Methods of Statistical Discrimination', *Applied Statistics* **26**(1), 15–25.

Anderson, T. (1984), *An Introduction to Multivariate Statistical Analysis*, 2 edn, Wiley & Sons, New York.

classifier970818

Errors Target -> Other

	0	0.1	0.2	0.3	0.4	0.5	0.6	0.7	0.8	0.9	1	t->o
0	93	0	0	0	0	0	0	0	0	0	0	
0.1	106	4	3	3	3	3	3	2	2	2	2	
0.2	106	6	4	4	3	3	3	3	3	3	3	
0.3	106	9	6	4	4	4	3	3	3	3	3	
0.4	106	9	6	5	4	4	4	4	3	3	3	
0.5	106	9	6	6	5	4	4	4	4	4	3	
0.6	106	9	9	6	6	4	4	4	4	4	4	
0.7	106	9	9	6	6	5	4	4	4	4	4	
0.8	106	10	9	8	6	6	5	4	4	4	4	
0.9	106	10	9	9	6	6	6	5	4	4	4	
1	106	11	9	9	6	6	6	5	5	4	4	
o->t												

Errors Other -> Target

	0	0.1	0.2	0.3	0.4	0.5	0.6	0.7	0.8	0.9	1	t->o
0	548	548	548	548	548	548	548	548	548	548	548	
0.1	0	4	7	9	12	14	16	18	18	18	20	
0.2	0	3	4	5	7	9	9	11	12	13	14	
0.3	0	2	4	4	5	5	7	9	9	9	11	
0.4	0	2	3	4	4	5	5	5	7	8	9	
0.5	0	2	3	4	4	4	5	5	5	6	7	
0.6	0	2	2	3	4	4	4	5	5	5	5	
0.7	0	2	2	3	4	4	4	4	5	5	5	
0.8	0	2	2	2	3	4	4	4	4	4	5	
0.9	0	2	2	2	3	4	4	4	4	4	4	
1	0	2	2	2	3	3	4	4	4	4	4	
o->t												

Run New OK

Figure 17: Screen-dump of cost factor adjustment tool. It displays the number of misclassifications from the target class(es) to other classes (upper panel) and vice versa (lower panel) in dependence of the cost factors `o2t` (abscissa) and `t2to` (ordinate). By clicking on one of the matrix fields, one can zoom in to a smaller range of cost factors around the values of that field.

Beers, T. C., Preston, G. W. & Shectman, S. A. (1992), 'A search for stars of very low metal abundance. II.', *AJ* **103**(6), 1987–2034.

Deichsel, G. & Trampisch, H. J. (1985), *Clusteranalyse und Diskriminanzanalyse*, Gustav Fischer Verlag, Stuttgart.

Hagen, H.-J., Groote, D., Engels, D. & Reimers, D. (1995), 'The Hamburg Quasar Survey. I. Schmidt observations and plate digitizations', *A&AS* **111**, 195–203.

Hand, D. (1981), *Discrimination and Classification*, Wiley & Sons, New York.

Kilkenny, D., Heber, U. & Drilling, J. S. (1988), 'A catalogue of spectroscopically identified hot subdwarf stars', *SAAO Circ.* **12**, 1–80.

Kilkenny, D., O'Donoghue, D., Koen, C., Stobie, R. S. & Chen, A. (1997), 'The Edinburgh-Cape Blue Object Survey – II. Zone 1 – The North Galactic Cap', *MNRAS* **287**, 867–893.

Murtagh, F. & Heck, A., eds (1987), *Multivariate Data Analysis*, Reidel, Dordrecht.

Schuster, W. J., Nissen, P. E., Parrao, L., Beers, T. C. & Overgaard, L. (1996), 'uvby-β photometry of high-velocity and metal-poor stars. VIII. Stars of very low metal abundance.', *A&AS* **117**, 317–334.

von Laar, H. (1995), Spektrophotometrische Eichung von Objektivprismenplatten, Diplomarbeit, Universität Hamburg.

Wilhelm, R., Beers, T. C., Sommer-Larsen, J., Pier, J. R., Layden, A. C., Flynn, C., Rossi, S. & Christensen, P. R. (1999), 'Spectroscopy of Hot Stars in the Galactic Halo. III. Analysis of a Large Sample of Field Horizontal-Branch and Other A-Type Stars', *AJ* **117**, 2329–2380.

Wisotzki, L. (1991), Ein statistisches Verfahren zur automatischen Quasarsuche, PhD thesis, Universit"at Hamburg.

Wisotzki, L., Christlieb, N., Bade, N., Beckmann, V., Köhler, T., Vanelle, C. & Reimers, D. (2000), 'The Hamburg/ESO survey for bright QSOs. III. A large flux-limited sample of QSOs', A&A, in press.

4 A Deep Survey for Extremely Metal-Poor Halo Stars

4.1 Introduction

A question that has been asked by astronomers for a long time is whether so-called population III (Pop. III) stars exist. Bond (1981) "roughly" defines them "as stars with [Fe/H] < -3". Of *such* stars, ~ 100 are known today (Beers 1999), but today other definitions of Pop. III are used. Cayrel (1996) defines them as stars "with strictly the chemical composition left by the Big Bang", and Beers (2000*b*), for practical reasons, adds the criterion that such stars should have "a measurable atmospheric abundance of [Fe/H] < -6". Cayrel (1996) estimates the number of Pop. III stars expected to be discovered within the survey of Beers et al. (1992), when completed, to 1.8. However, in estimations like this it is assumed that first generation of stars includes low-mass stars. The mass spectrum of the first generation of is not known, and actually *no* Pop. III star has yet been found (Beers 1999). On the other hand, the absence of Pop. III stars in current samples of metal-poor stars is hardly significant: Today, only 18 stars of [Fe/H] < -3.5 are known (Beers 1999), of which only 5 have their abundances confirmed by high resolution spectroscopy (Beers 2000, priv. comm.). The discovery of a Pop. III star would offer the possibility to study primordial matter, whereas their *quantified* absence would put important constraints to models of the formation of the first generation of stars in our Galaxy, so that either case is interesting in itself.

The chemical compositions of the *second* generation of stars, i.e. extremely metal-poor halo stars (hereafter shortly referred to as MPHS) of [Fe/H] < -2.5, provide detailed information on the early chemical evolution of the Galaxy, and on nucleosynthesis in the first generation of stars. There is evidence that the abundance patterns seen in MPHS can be attributed to individual supernovae of type II (e.g., Shigeyama & Tsujimoto 1998; Tsujimoto et al. 2000).

MPHS also have cosmological applications. The oldest stars provide a lower limit for the age of the Universe, yielding constraints for the cosmological parameters. How can we find the oldest stars? Models of Galactic chemical evolution predict that heavy element abundances, e.g. [Fe/H], are no good age indicators, because mixing of nucleosynthesis products of SN II into the interstellar gas is very inefficient (see e.g. Beers et al. 2000*b*). This means that at given metallicity, there is likely a large scatter of stellar ages, and *some* metal-poor stars can be rather young. However, with increasing time, the interstellar gas is more and more enriched by the nucleosynthesis products of SN II (and later, SN I), so that there is higher chance for young stars to be metal-rich than to be metal-poor. Conversely, if we look at very metal-poor stars, we will find more old stars among them than in a sample of metal-rich stars.

Individual ages of stars can best be measured by two methods: by nucleocosmochronology, and with individual fitting of evolutionary paths. The former is feasible for stars showing an r-process abundance pattern, and having spectra with detectable Thorium (and optionally, Uranium) lines. Today, only two such stars are known: HD 115444 and CS 22892-052 (Cowan et al. 1999). Ages can be derived using the abundance ratios [Th/Eu] and [Th/U]. However, the accuracy achievable with this method, when including *theoretical* uncertainties, is ± 4 Gyrs only (Cowan et al. 1999). A higher accuracy (± 2 Gyrs) can be reached by fitting of individual evolutionary tracks to accurate stellar parameters $T_{\rm eff}$, $\log g$, [Fe/H] and [α/H] (Bernkopf & Gehren 1999, priv. comm; see also Fuhrmann 1999).

If individual ages are obtained for a large sample of MPHS, this would offer the opportunity to study the chemical evolution of the Galaxy *directly* as a function of time. Up to now, one has to use secondary age indicators, like [Fe/H]. As already argued above, such age indicators are likely not valid for population II, due to inhomogeneous mixing of the interstellar matter.

~ 100 stars of [Fe/H] < -3.0 might sound like a large sample. However, in practice one often has to select suitable subsamples of objects. For example, when studying Lithium abundances, it is necessary to restrict the sample to a narrow temperature range, in order to avoid influences of temperature dependent effects, like depletion; for other studies, one wants to select subsamples by kinematic properties. Moreover, the fraction of binaries among the most metal-poor stars is unclear. Abundance analysis of single-lined binaries may be complicated, or even impossible. Last but not least, any *new* questions are sure to arise from the first-pass 8 m-class telescope follow-ups (see Beers 2000*a*), which likely can only be answered by larger samples of extremely metal-poor stars.

For all these reasons, it is desirable to enlarge the survey volume for extremely metal-poor stars *now*, which currently can be only accomplished by the HES (for a review of ongoing surveys for metal-poor stars see Beers 2000*b*). Our specific aims are:

(a) Providing a *quantitative* answer to the question of the existence of Pop. III. This is possible in the HES, since the survey volume can be enlarged with the HES, making the absence of Pop. III stars more significant in case no such object will be found. In contrast to the HK survey, in the HES the selection function of MPHS can be determined by simulations, so that we would be able to quantify the (possible) absence of Pop. III stars.

(b) Enlarging the sample of stars with [Fe/H] < -3.0.

(c) Finding more stars with r-process abundance patterns and detectable Th lines, like CS 22892-052, for age determination.

In order to elucidate what the advantages of the HES compared to the so-called HK survey of Beers et al. (1992) are, we give a detailed comparison of both surveys in the next section. An overview can be found in Tab. 7.

		HK survey	HES
Telescope	north	0.6 m Burrell Schmidt	—
	south	0.6 m Curtis Schmidt	1 m ESO Schmidt
Magnitude range		$11.0 \lesssim B \lesssim 15.5$	$14.0 \lesssim B \lesssim 17$
Widened?		yes	no
Area	north	2800□°	—
	south	4100□°	7600□°
Objective prism		4°	4°
Dispersion		180 Å/mm	450 Å/mm
Spectral resolution		~ 5 Å	~ 10 Å at Ca K
Photographic emulsion		103a-O/IIa-O	IIIa-J
Filter?		interference/Ca H+K	no
Wavelength range		$3875\,\text{Å} < \lambda < 4025\,\text{Å}$	$3200\,\text{Å} < \lambda \lesssim 5200\,\text{Å}$
Candidate selection		visual inspection	automated

Table 7: Comparison of the HK survey and the HES.

4.2 Comparison of HES and HK survey

The HK survey was started in 1978 by G. Preston and S. Shectman of the Carnegie Observatories of Washington. It is based on objective prism plates taken with the 60 cm Burrell Schmidt (northern hemisphere) and Curtis Schmidt (southern hemisphere) telescopes. As in the HES, each photographic plate covers a nominal area of $5^\circ \times 5^\circ$ of the sky. The name "HK survey" is used because in addition to a 4° objective prism (leading to a seeing-limited spectral resolution of ~ 5 Å), an interference filter was mounted on the plate holder to limit the wavelength coverage to ~ 150 Å centered on the Ca H+K resonance lines, effectively reducing the sky background level so that long exposures (typically 90 minutes) could be obtained. In 1983 Beers joined the team, and later expanded the survey with an additional 240 plates in the southern and northern hemispheres. By 1992, 308 acceptable-quality plates were obtained (275 of which are unique). Note that due to the small spectral range of the HK survey, overlapping spectra are much less of a problem than in the HES. Further extension of the HK survey area was prevented by the shortage of photographic plates with 103a-O and IIa-O emulsions. HES areas in common with the HK survey are shown in Fig. 19.

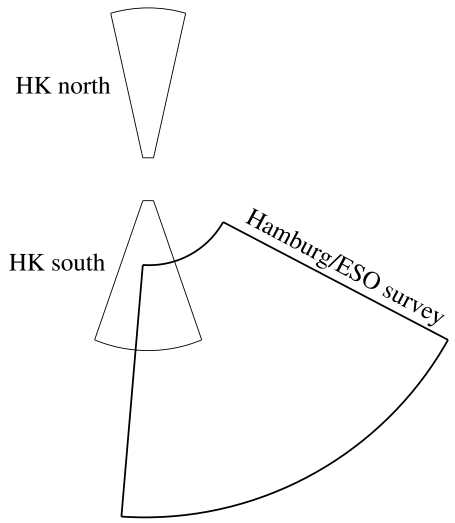

Figure 18: Comparison of HES and HK survey volumes.

The use of a larger telescope, and a 2 times lower resolution of the HES compared to the HK survey, results in a limiting magnitude of about $B = 17.5$. However, we restricted the selection of metal-poor candidate stars in the HES to $S/N > 10$, because it was found that below this S/N level it is extremely difficult to select objects by the absence of individual spectral lines, i.e., the Ca K line in case of metal-poor stars. In result, the faintest low-metallicity candidates in the HES sample reach $B \sim 17$, about 1.5 magnitudes deeper than the HK survey. Spectra of bright objects close to saturation were also excluded from the search for metal-poor stars, because at high illumination, when the characteristic curve of the photographic emulsion gets flatter (at the "shoulder"), the contrast between continuum and spectral lines gets weaker, and apparently *all* stars have weak lines. The saturation threshold chosen in the HES corresponds to $B \sim 14.0$. Taking the common area of both surveys and their magnitude ranges into account, the HES can increase the total survey volume for metal-poor stars by a factor of 8 compared to the HK survey alone (see also Fig. 18).

Candidate selection in the HK survey was done by visual inspection of the widened objective-prism spectra with a binocular 10× microscope. Each plate was inspected twice, with a time lag of a month or more between the two inspections. Candidates were identified on the basis of the observed strengths of their Ca lines, and grouped into rough categories based on this criteria (e.g., possibly metal-poor, metal-poor, and extremely metal-poor). Positions of the candidates were noted on the plates, and coordinates for each candidate were measured later (individually, with Grant machines). In this process, a total of about 10000 metal-poor candidates was selected (roughly half of which have had medium-resolution

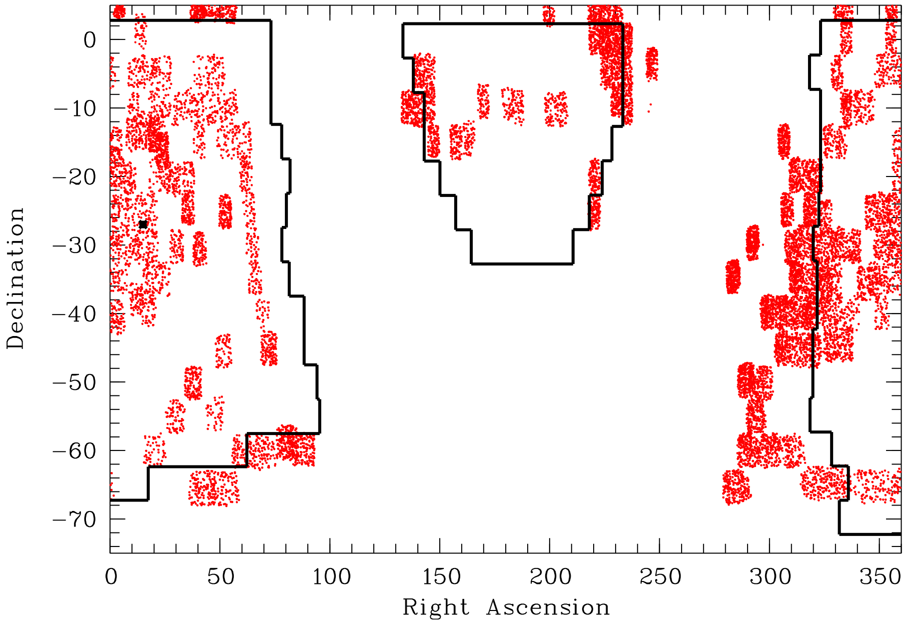

Figure 19: Comparison of HES area (framed) with HK survey area. Dots denote all HK survey candidates in the southern hemisphere.

follow-up spectroscopy obtained to date).

One major advantage of the HES is that the candidate selection is done *automatically*, with *quantifiable* selection criteria. We will show in Sect. 4.5 that although the spectral resolution of the HES is $2\times$ lower than in the HK survey, candidate selection in the HES is up to 3–7$\times$ more efficient than in the HK.

4.3 Candidate Selection in the HES

For the present, we have restricted the selection of metal-poor stars in the HES to the color range $0.3 < B-V < 0.5$, because we decided to focus at first on main-sequence turnoff stars. One of the most interesting applications for these stars is individual age determination based on precise stellar parameters obtained spectroscopically from high-resolution, high S/N observations. However, with a few adaptions the selection procedures described below can easily also be used for cooler stars.

Candidate selection in the HES has been done by two techniques: The Ca K index method and via automatic classification. An alternative, third approach is to determine stellar parameters directly from HES spectra by calibrating spectral features against a learning sample.

4.3.1 The Ca K Index Method

In the Ca K index method, stars are selected when their Ca K line is significantly weaker than “normal.” “Normality” is determined by a least squares fit of a 2nd order polynomial to the Ca K index relative to the parameter `x_hpp2`. At the time this selection technique was used, it was not yet clear that the use of `dx_hpp2` instead of `x_hpp2` leads to a more accurate $B-V$ colour estimation.

A first set of candidates found with this techniques has been observed in spectroscopic follow-up campaigns at the ESO NTT. In Tab. 24 in Appendix A we list the stars found in this effort. Unfortu-

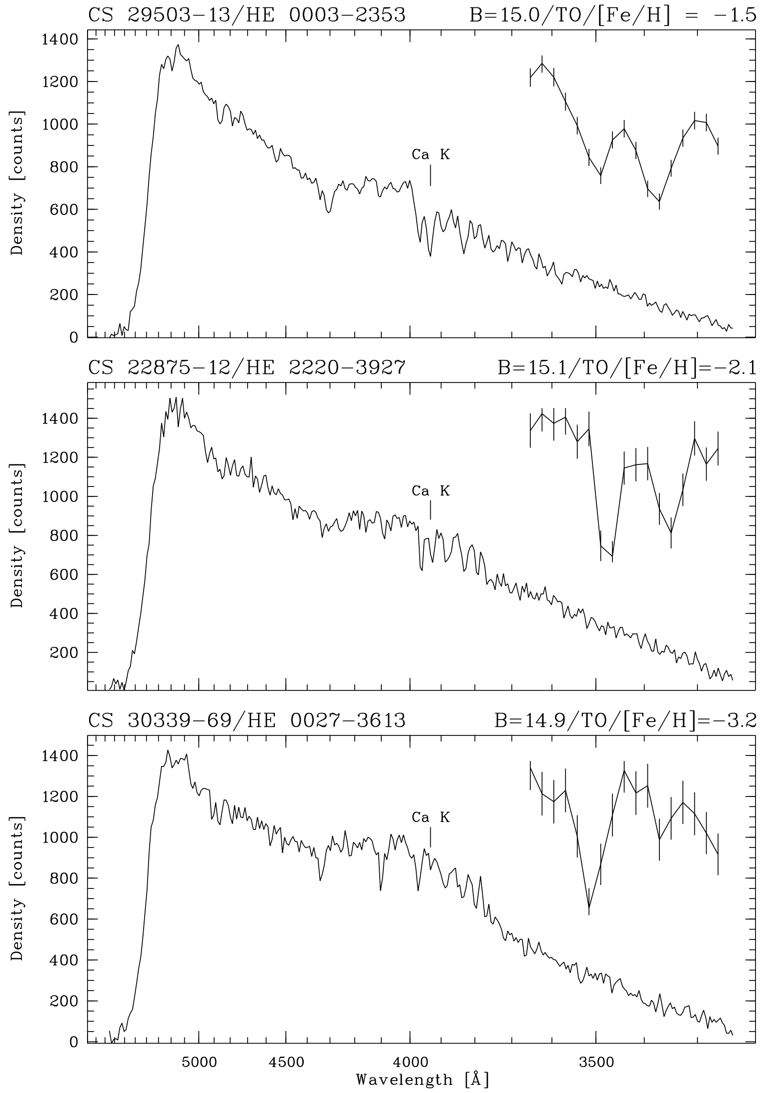

Figure 20: Examples of HES spectra of metal-poor turnoff stars discovered in the HK survey. In the upper right corner of each plot a blow-up of the Ca H+K region is shown, with an over-plot of the pixel-wise 1 σ noise. Note that the detection of Ca K in the lower spectrum is not significant. Metal abundances are on the re-calibrated HK survey scale of Beers et al. (1999).

nately, due to bad weather, and continued technical problems, it was not yet possible to evaluate the quality of the Ca K index selection method. A set of ~ 40 spectra have been obtained at the McDonald 2.7 m and CTIO 4 m telescopes recently by T. Beers, and will be analyzed as soon as the data has been reduced.

4.3.2 Automatic Spectral Classification

For automatic classification of metal-poor stars, we use a learning sample consisting of 45 classes defined by the following grid points:

$$T_{\rm eff} = 5800\,{\rm K}, 6400\,{\rm K}, 6800\,{\rm K}$$

$$\log g = 2.2, 3.8, 4.6$$
$$[\mathrm{Fe/H}] = -0.9, -1.5, -2.1, -2.7, -3.3$$

The learning sample has again been constructed by converting model spectra to simulated objective-prism spectra, as described in Sect. 3.1.

A set 11 of features was selected as a basis for searching the best combination: the strengths of Ca K, measured by the absorption line fit algorithm, and by an index method; the sum of the equivalent widths of Hβ, Hγ and Hδ; the Strömgren coefficient c_1, two continuum principal components, and the half-power points `x_hpp1` and `x_hpp2`. Half power points themselves instead of distances to the cutoff values have to be used since the latter cannot be determined for simulated spectra. Apart from these "standard features" we carried out a principal component analysis of a set of 165 000 simulated spectra, and used the first 3 principal components, accounting for 90.5 % of the variance in the set of simulated spectra, as additional features (see Fig. 21 for the Eigenvectors).

By evaluating all $2^{11}-1=2047$ possible feature combinations at each S/N step by the "leaving one out" method, we identified the feature combinations leading to the lowest number of misclassifications (see Tab. 8). In order to explore the classification accuracy, we used Bayes' rule instead of the minimum cost rule for classification, and assumed equal prior probabilities $P(\Omega_j)$ for each class, because otherwise the estimation of the classification accuracy would be distorted.

Feature	S/N 30	25	20	15	10	5
`all3934eqw`	1	1	1	1	1	1
`CaKindex`	1	1	1	1	0	0
`cklcomp_1`	0	0	1	0	0	0
`cklcomp_2`	0	1	0	0	0	0
`balmsum`	1	1	1	1	0	1
`x_hpp1`	1	1	1	0	0	0
`x_hpp2`	1	1	1	1	1	1
`sklcomp_1`	1	1	1	1	1	1
`sklcomp_2`	1	1	1	1	1	1
`sklcomp_3`	1	1	1	1	1	1
`strc1`	0	0	0	1	0	0
$N=$	8	8	9	8	5	6

Table 8: Best feature combinations for Bayes classification of metal-poor stars in the colour range $0.3 < B-V < 0.5$.

The formal classification errors determined are $\sigma_{T_{\mathrm{eff}}} < 160\,\mathrm{K}$, $\sigma_{\log g} < 0.34\,\mathrm{dex}$ $\sigma_{[\mathrm{Fe/H}]} < 0.71$; for $S/N > 15$, i.e. for $2/3$ of the HES spectra, the errors are $\sigma_{T_{\mathrm{eff}}} < 65\,\mathrm{K}$, $\sigma_{\log g} < 0.06\,\mathrm{dex}$ $\sigma_{[\mathrm{Fe/H}]} < 0.68$. That is, the error estimates for T_{eff} and $\log g$ *are not to be believed*. First of all, our grid of model atmospheres is not dense enough to detect such low errors. Moreover, such accuracies are not even achievable with high-resolution, high S/N spectra. Apart from the grid being too wide, we suspect that there is a systematic difference between our learning (and test) sample, and sets of real spectra.

Considerable effort has been invested in making the simulated objective prism spectra as realistic as possible, and we can exclude with high confidence that the difference is due to the simulated spectra *themselves*. The most reasonable explanation for our too optimistic error estimate is the following. The

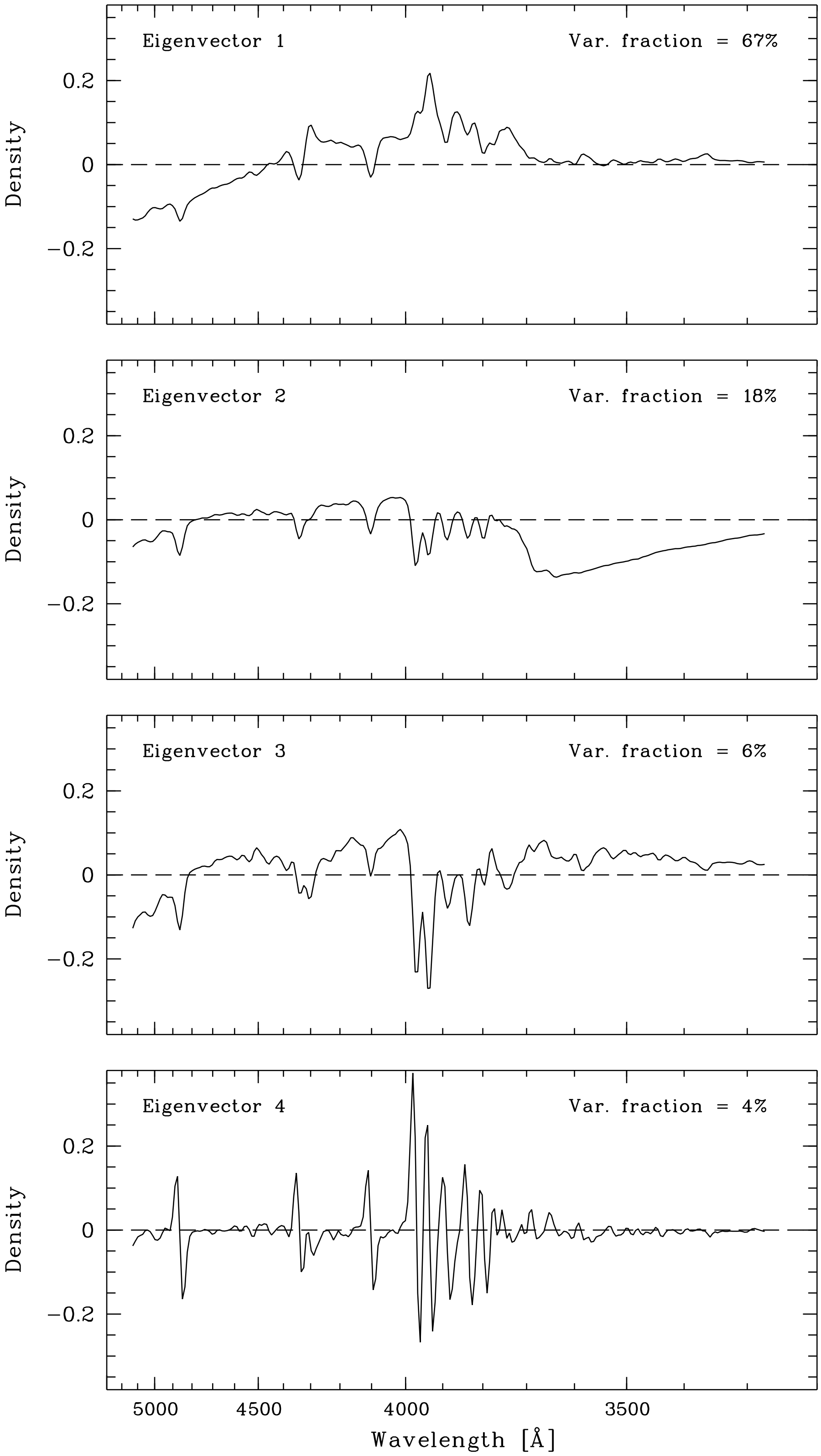

Figure 21: First four Eigenvectors of a sample of 165 000 simulated objective prism spectra for metal-poor stars. The first Eigenvector models the Balmer lines, and $B-V$; the latter is accomplished by changing the continuum slope. The second Eigenvector influences the Balmer discontinuity, the Balmer lines, and Ca H+K. In the third, Ca H+K can be seen even more prominently. The G-band of CH at $\lambda = 4300$ Å can also be seen. The forth Eigenvector mainly accounts for small shifts in the wavelength zero points.

spectra in our learning and test samples have stellar parameters belonging to a *discrete grid*, whereas in reality, the stellar parameters are distributed *continously*. A spectrum with stellar parameters between two grid points is misclassified at least with errors corresponding to (at least) half of the grid point distance, which is $\Delta T_{\rm eff} = 100\,{\rm K}$, $\Delta \log g = 0.4\,{\rm dex}$, and $\Delta{\rm [Fe/H]} = 0.15\,{\rm dex}$ (for $[{\rm Fe/H}] < -0.9$). However, spectra between grid points *do not exist* in our test samples, so that we underestimate the mean errors.

The only ways out of this trap are: (a) testing the classification with sets of real spectra, having a continuous parameter distribution; or (b), making the grid "pseudo-continuous", i.e., so fine that there is no noticeable difference between the spectra belonging to two neighboring grid points. The latter is rather resource demanding, since the number of grid points in three-dimensional parameter space raises to the third power; that is, halving the grid point distance in each dimension lets the number of grid points grow by a factor of $((2n-1)/n)^3$.

As test sample with continuous stellar parameter distribution we tried to use 262 stars from the HK survey present on HES plates, with available [Fe/H] estimate, not saturated in the HES, and in the range covered by our model spectra grid, i.e. $0.3 < B-V < 0.5$. Unfortunately, $T_{\rm eff}$ and $\log g$ are not directly determined in the HK survey, so that only our [Fe/H] estimations could be tested. However, it turned out that only 4 of the 262 objects have an $a.i. < 0.99$; that is, almost all spectra have been rejected from classification. This has likely again to be attributed to a too narrow model spectra grid.

In conclusion, the above considerations indicate that our grid of model spectra is not pseudo-continuous in $T_{\rm eff}$ and $\log g$. This partly is very good news, since it means that there *is* a noticeable difference between the spectra of two neighboring grid points; that is, we can likely classify the HES spectra with an accuracy better then $\sigma_{T_{\rm eff}} \sim 200\,{\rm K}$, and $\sigma_{\log g} \sim 0.8\,{\rm dex}$, at least at high S/N.

4.3.3 The Feature Calibration Approach

We investigated how precise $T_{\rm eff}$, $\log g$ and [Fe/H] can be determined from HES spectra directly, by calibrating HES features against a learning sample of simulated objective prism spectra. If this is possible with an acceptable accuracy, an alternative way of selecting candidates for extremely metal-poor stars would be offered.

In the first step of our investigation we carried out a parameter study to investigate which stellar features a suitable for our purpose. In the study we used a denser grid of model spectra, defined by the following grid points:

$$\begin{aligned} T_{\rm eff} &= 5600(200)6800\,{\rm K} \\ \log g &= 2.2(0.8)4.6 \\ [{\rm Fe/H}] &= -0.3, -0.9, -1.5(0.3)-3.6 \end{aligned}$$

Each of the model spectra has been converted to 500 objective prism spectra, involving randomized spectral sensitivity curves, and smoothed with a Gaussian profile of $45\,\mu{\rm m}$ FWHM, corresponding to an average seeing profile width in the HES. The S/N of the simulated objective prism spectra has been decreased to $S/N = 30$ by adding Gaussian noise.

Effective Temperature Indicators Possible indicators for $T_{\rm eff}$ are `x_hpp2`, the sum of the equivalent widths of Hβ, Hγ and Hδ, determined with the feature detection algorithm described in Sect. 3.2.1, and the first spectral principal component (SPC), `sklcomp_1`.

`x_hpp2` and `sklcomp_1` are very good $T_{\rm eff}$ indicators: From Fig. 22 one can estimate that at $S/N = 30$, $T_{\rm eff}$ can be determined with an accuracy of in the order of $\pm 200\,{\rm K}$ with them. The Balmer

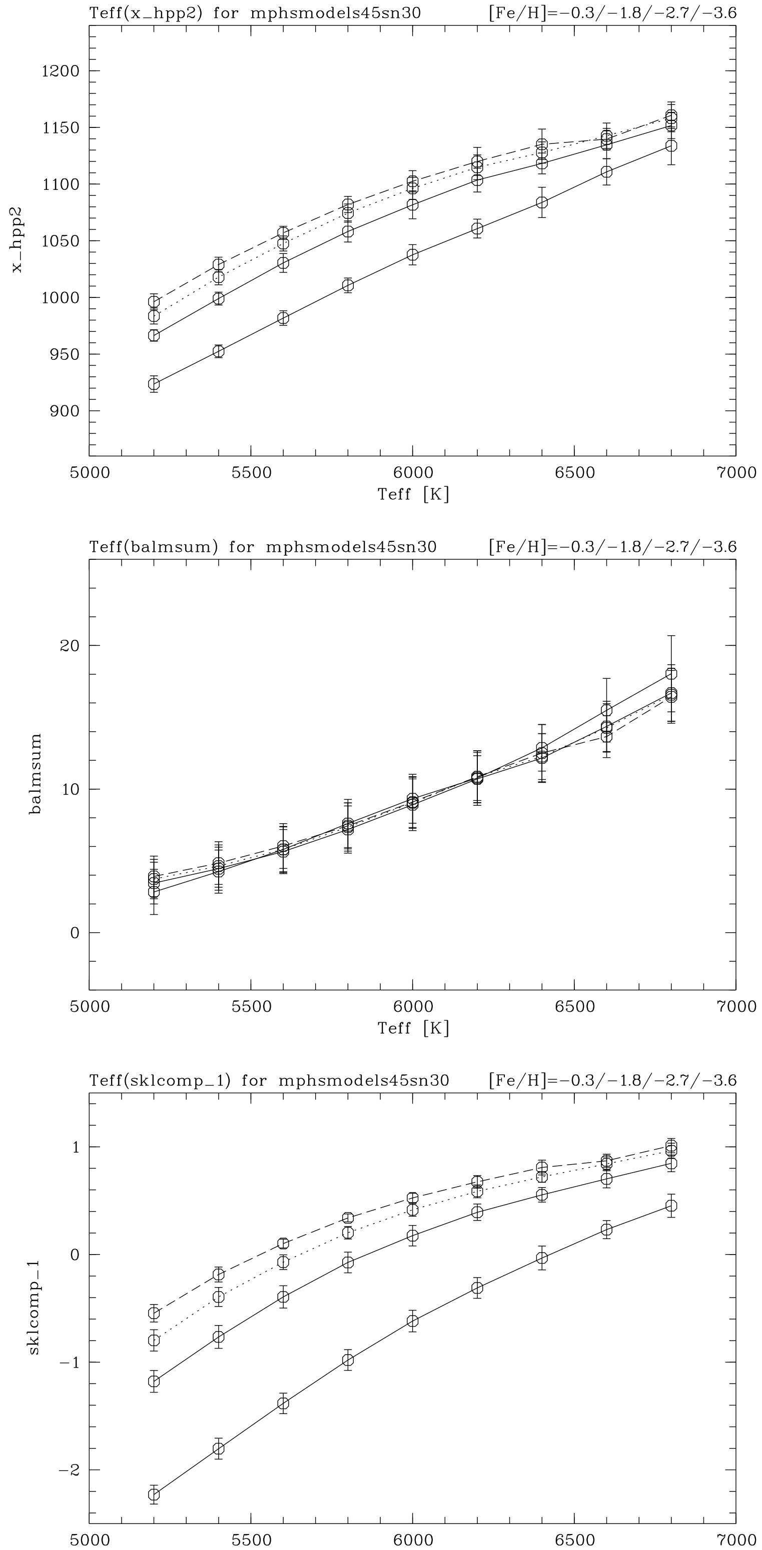

Figure 22: Investigation of possible effective temperature indicators in HES spectra.

line sum is a slightly worse indicator, leading to an accuracy of ~ 400 K. However, x_hpp2 and sklcomp_1 show a strong dependence on [Fe/H], whereas the Balmer line sum is almost completely independent of metallicity.

Gravity Indicators Strömgren c_1 is a possible gravity indicator, since it measures the strength of the Balmer jump. The 2nd SPC might also be suitable, since the corresponding Eigenvector seems to be responsible for modelling the Balmer jump. However, it turned out that c_1 is by far a better gravity indicator (see Fig. 23). Both features show a strong temperature dependence.

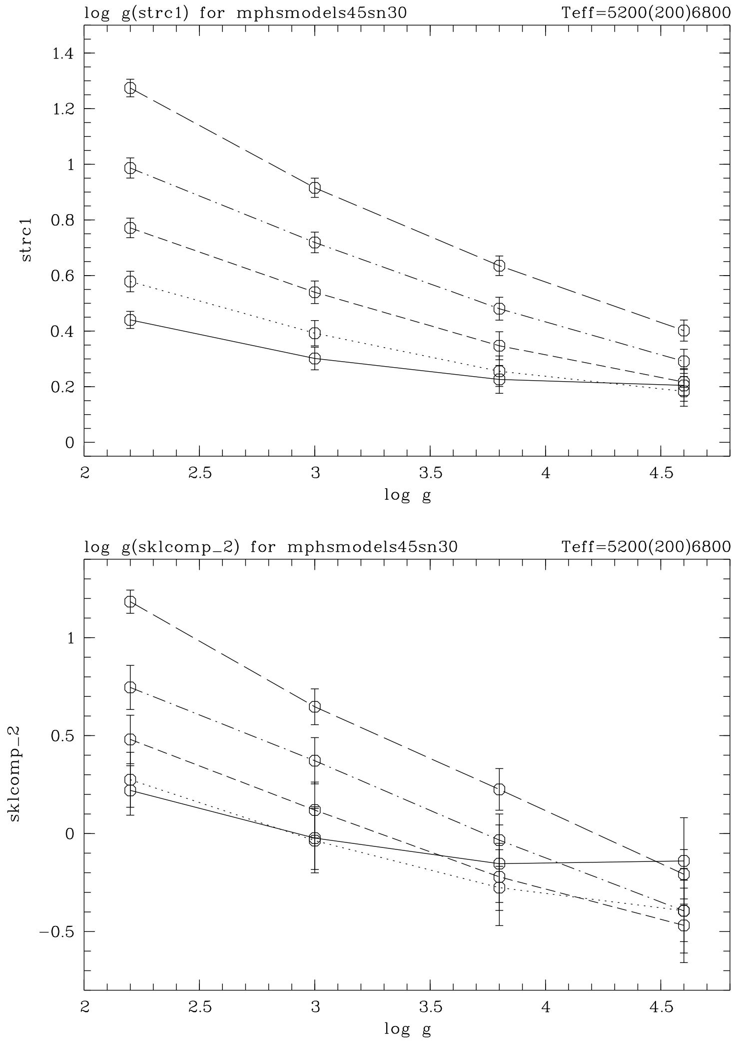

Figure 23: Investigation of possible gravity indicators in HES spectra.

Metallicity Indicators The Ca K line is the most usefull metallicity indicator, because the Ca K line is by far the strongest metal line seen in cool stars. Ca H is not suitable, since it is blended with Hε. We measure the strengths of Ca K in HES spectra with two methods: With a line fitting algorithm (yielding the feature all3934eqw), and with an index (CaKindex). The 3rd SPC contributes to modelling the Ca H+K lines, so it was investigated as well.

As is displayed in Fig. 24, the 3rd SPC shows only a weak dependence on [Fe/H]. all3934eqw

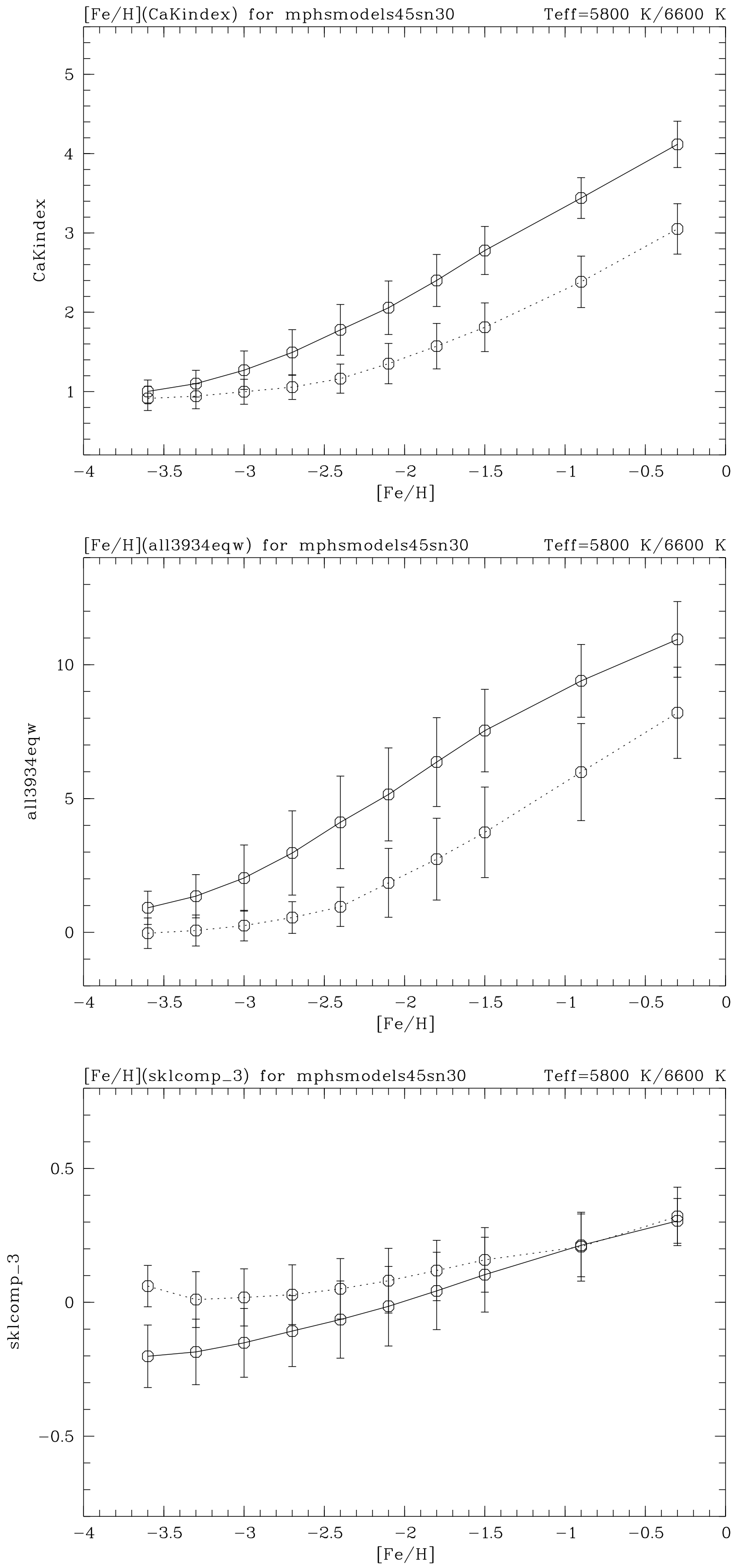

Figure 24: Investigation of possible metallicity indicators in HES spectra.

and `CaKindex` are both suitable. However, investigation of lower S/N spectra revealed that the former is less robust against noise.

Within the set of 165 000 simulated spectra available for each S/N step, we averaged the values of the features under consideration over all 500 simulatd spectra having the same spectral parameters T_{eff}, $\log g$, [Fe/H]. To these data points, the following models were fitted with a least squares fit:

$$\begin{aligned}
T_{\mathrm{eff}} &= a_1 + a_2 \cdot \texttt{sklcomp_1} + a_3 \cdot \texttt{CaKindex} + a_4 \cdot \texttt{sklcomp_1}^2 + a_5 \cdot \texttt{CaKindex}^2 && (16)\\
T_{\mathrm{eff}} &= a_1 + a_2 \cdot \texttt{balmsum} + a_3 \cdot \texttt{balmsum}^2 && (17)\\
\log g &= a_1 + a_2 \cdot c_1 + a_3 \cdot \texttt{balmsum} + a_4 \cdot c_1^2 + a_5 \cdot \texttt{balmsum}^2 && (18)\\
[\mathrm{Fe/H}] &= a_1 + a_2 \cdot \texttt{CaKindex} + a_3 \cdot \texttt{sklcomp_1} + a_4 \cdot \texttt{CaKindex}^2 + a_5 \cdot \texttt{sklcomp_1}^2 && (19)\\
[\mathrm{Fe/H}] &= a_1 + a_2 \cdot \texttt{CaKindex} + a_3 \cdot \texttt{balmsum} + a_4 \cdot \texttt{CaKindex}^2 + a_5 \cdot \texttt{balmsum}^2. && (20)
\end{aligned}$$

We found that the models (16), (19) lead to slightly better results than their alternatives (17), (19), so that we use `sklcomp_1` and `CaKindex` for determining T_{eff} and [Fe/H]. The fit coefficients vary slightly with S/N; thus for each spectrum the appropriate set of coefficients has to be used.

We tested the accuracy of our method by applying it to 6 sets of 165 000 spectra, at $S/N = 5, 10, 15, 20, 25, 30$. Because the parameters of our models have been derived by using these spectra indirectly, it is anticipated that we *underestimate* the errors in this investigation. The results are shown in Fig. 25. For $S/N > 15$, the uncertainties are $\sigma_{T_{\mathrm{eff}}} < 130$ K, $\sigma_{\log g} < 0.48$ dex and $\sigma_{[\mathrm{Fe/H}]} < 0.47$. The errors increase sharply at $S/N < 10$, which reinforces our decision to exclude such spectra from the search for metal-poor stars.

As an independent test sample we used 460 stars from the HK survey present on HES plates, with available [Fe/H] estimate, not saturated in the HES, and in the $B-V$ range covered by our model atmospheres, i.e. $0.29 < B-V < 0.70$. The metallicities were scaled to the HES abundance scale using Eq. (24). The standard deviation of the measurements directly in the HES spectra from the moderate resolution spectroscopy results is 0.85 dex. This is 0.38 dex, or by a factor 1.81, higher than expected for the relatively bright stars from the HK survey used as test objects: The average S/N of that sample is ~ 25, which led to $\sigma_{[\mathrm{Fe/H}]} = 0.47$ in the sample of simulated spectra. The lower accuracy is most likely due to the discontinuity effect discussed above.

There is also evidence for a systematic deviation between the two sets of [Fe/H] measurements: The mean difference between is -0.28 dex; i.e., the [Fe/H] estimates directly from HES spectra are too low. Moreover, there is a systematic trend of the [Fe/H] deviations with [Fe/H] itself; i.e., a too low [Fe/H] is assigned to spectra of "metal-rich" objects, and a too high [Fe/H] to spectra of metal-poor objects (see Fig. 26). The former results in contamination of metal-poor star samples selected with this method, and the latter in incompleteness. This method is thus expected to be of restricted usefulness for the selection of metal-poor stars.

4.3.4 Visual Inspection

The final step of the selection is visual inspection of the automatically selected spectra at the computer screen. This step is done for *all* selections described above. Visual inspection is necessary for identification of plate artifacts (e.g. scratches or emulsion flaws), and for rejection of obviously misclassified spectra, i.e. spectra which clearly show a Ca K line. Misclassifications like that happen due to equivalent width measurement errors. The remaining candidates are divided into three classes according to the appearance of the Ca K line region: "class a" candidates show clearly no line; in spectra of "class b"

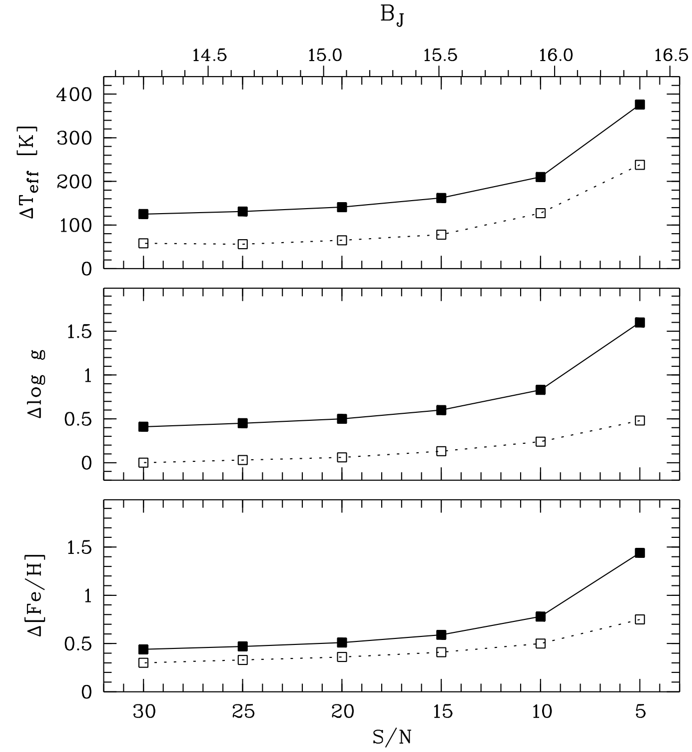

Figure 25: Accuracy of HES feature calibration method for determining stellar parameters directly from HES spectra in dependence of S/N (solid line), compared to accuracy achieved with automatic classification (dotted line). corresponding B_J derived from Eq. (5).

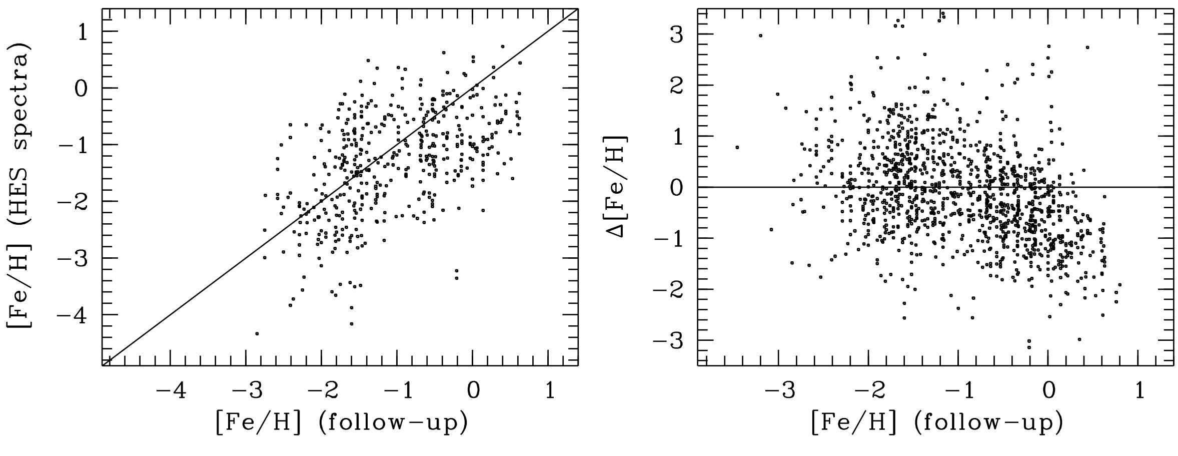

Figure 26: Comparison of [Fe/H] derived from HES spectra with the feature calibration method versus [Fe/H] from moderate resolution follow-up spectroscopy of HK survey stars. [Fe/H] was scaled to the HES abundance scale.

candidates it is unclear if they have a line, and “class c” candidates *do* show a Ca K line, but however, a weak one. Typically, only 10 % of the candidates belong to class a or b, 40 % belong to class c, 25 % are misclassifications, and further 25 % are disturbed spectra.

4.4 Spectroscopic Follow-up techniques

As we have seen in Sect. 4.3, stellar parameters can be derived from HES spectra (and objective prism spectra in general) only with limited accuracy. Therefore, the HES, and all other objective prism surveys, can only provide *candidate* identifications. Because one does not want to spend significant amounts of large telescope time for obtaining high-resolution, high-S/N spectra of uninteresting stars, spectroscopic follow-up observations of such candidates has to be done with great care.

4.4.1 The Ca K-index and ACF Methods

For candidate low-metallicity stars in the HK survey, medium resolution (1–2 Å) spectroscopy and broadband *BV* photometry are used to obtain metallicity estimates using two separate techniques. The first technique relies on the assumption that the strength of the Ca K line tracks the overall stellar [Fe/H], an assumption which is particularly good for stars with [Fe/H] ≤ -1.5. The second is based on an Auto-Correlation Function (ACF, originally described by Ratnatunga & Freeman 1989) of a stellar spectrum. The ACF method is particularly good for stars with [Fe/H] > -1.5, where the Ca K line begins to saturate with increasing metal abundance. Beers et al. (1999) discuss this calibration, and demonstrate, based on comparisons with some 550 stars with external high-resolution abundance estimates, that these approaches used in combination yield abundance determinations with small scatter (on the order of 0.15–0.20 dex) over the entire range of stellar abundances we expect to find in the Galaxy ($-4.0 \leq$ [Fe/H] ≤ 0.0).

4.4.2 The “All in One Shot”-Technique

Due to limited telescope time available for follow-up observations, it would be desirable to obtain estimates of stellar parameters, e.g., [Fe/H], $T_{\rm eff}$, and $\log g$, purely spectroscopically, *without* the need for additional photometry. The first approach attempted with the HES follow-up made use of comparisons with synthetic spectra. However, our experience was that the choice to employ the Mg I b lines as gravity indicators leads to a number of difficulties. For example, satisfactory results required high S/N (> 50) spectra, which are very time consuming to obtain for the fainter stars. Furthermore, at [Fe/H]$\lesssim -2.5$ and turnoff temperatures, Mg I b is so weak that it is not sensitive to gravity anymore. Finally, the comparison of follow-up spectra with synthetic spectra has to be done manually at the computer screen, which is a time sink as well.

As an alternative, the “all in one shot”-technique described below was developed. It is fast, since for each star a single spectrum with $S/N \sim 30$ at Ca K is all that is required, and data analysis can be done fully automatically.

Following the idea of Norris & Freeman (1979), we obtain Strömgren *ubv* directly from the slit spectra by multiplication with filter response curves and integration over the appropriate wavelength range (see Fig. 27). Spectrophotometry of each candidate is obtained by using a wide slit ($\gtrsim 3\times$ seeing disc) rotated to the parallactic angle, to avoid atmospheric slit losses. When using EMMI at the 3.5 m ESO NTT, the spectral coverage required for obtaining Strömgren c_1 coefficients from the spectra ($3200\,\text{Å} < \lambda < 4900\,\text{Å}$) limits the maximum possible dispersion to 1.8 Å per pixel (grating #4), since in the blue arm of EMMI a 1 k CCD is the only available choice. The pixel size is $0\farcs37$, so that at seeing $< 1\farcs2$, a spectral resolution of < 6 Å results. Exposure times for obtaining $S/N > 30$ at Ca K are 5 min for stars of $B < 17.0$. In the case where stars exhibit a very weak Ca K line, as recognized from online-reduced spectra, an additional, longer, exposure with narrow ($1\farcs0$) slit is obtained. The average total exposure time per object is typically 10 min, which makes it possible to observe ~ 30 metal-poor candidates per night.

The spectra are shifted into the rest frame by cross-correlation with a model spectrum of similar stellar parameters, and applying the appropriate radial velocity correction. Note that the radial velocities derived are not useful measurements in themselves, since the precise position of the object in the (wide) slit is not known. Therefore, zero-point offsets in wavelength can occur.

Three features are used for determination of the stellar parameters [Fe/H], $T_{\rm eff}$, and $\log g$: the Strömgren coefficient c_1, the Hδ index HP2, and the Ca K index KP (for a definition see Beers et al. 1999). The internal accuracy achieved for spectrophotometric c_1 is $\sigma_{c_1} = 0.022$ mag, which compares favorably with errors from photoelectrically measured indices.

Stellar parameters are derived by using the following set of equations:

$$T_{\rm eff} = a_{11} + a_{12} \cdot c_1 + a_{13} \cdot \mathrm{HP2} \quad (21)$$
$$\log g = a_{21} + a_{22} \cdot c_1 + a_{23} \cdot \mathrm{HP2} \quad (22)$$
$$[\mathrm{Fe/H}] = a_{31} + a_{32} \cdot \mathrm{HP2} + a_{33} \cdot \mathrm{KP} \quad (23)$$

The coefficients a_{ij} have been determined from least squares fits to the dense grid of model spectra already described above, i.e.

$$\begin{aligned} T_{\rm eff} &= 5600(200)6800\,\mathrm{K} \\ \log g &= 2.2(0.8)4.6 \\ [\mathrm{Fe/H}] &= -0.3, -0.9, -1.5(0.3) - 3.6. \end{aligned}$$

Using equations (21)–(23), it was possible to reproduce the stellar parameters of the model spectrum grid with the following accuracy:

$$\begin{aligned} \sigma_{T_{\rm eff}} &= 24\,\mathrm{K} \\ \sigma_{\log g} &= 0.21 \\ \sigma_{[\mathrm{Fe/H}]} &= 0.16. \end{aligned}$$

Note that these are *internal* errors for *noise-free* spectra. Unfortunately, due to lack of an independent test sample, it is not yet possible to estimate the *real* accuracy of this approach. However, experience with spectrum synthesis has shown that at the spectral resolution used in the HES follow-up, errors in $\log g$ and [Fe/H] are typically twice as high as the numbers above, and errors in $T_{\rm eff}$ are typically < 200 K.

4.4.3 Neuronal Network Techniques

At the University of Texas in Austin, a group around T. von Hippel is currently exploring the use of Artifical Neuronal Networks (ANNs) for determination of stellar parameters $T_{\rm eff}$, $\log g$ and [Fe/H] from moderate resolution spectra, taken with a narrow slit, so that radial velocities could be obtained simultaneously (see Qu et al. 1998; Snider et al. 2000).

However, looking closely to Snider et al. (2000) reveals that the classification accuracy claimed, i.e. $\sigma_{T_{\rm eff}} = 3\,\%$ (corresponding to 135–189 K), $\sigma_{\log g} = 0.41$ dex and $\sigma_{[\mathrm{Fe/H}]} = 0.22$ dex, is doubtful. This

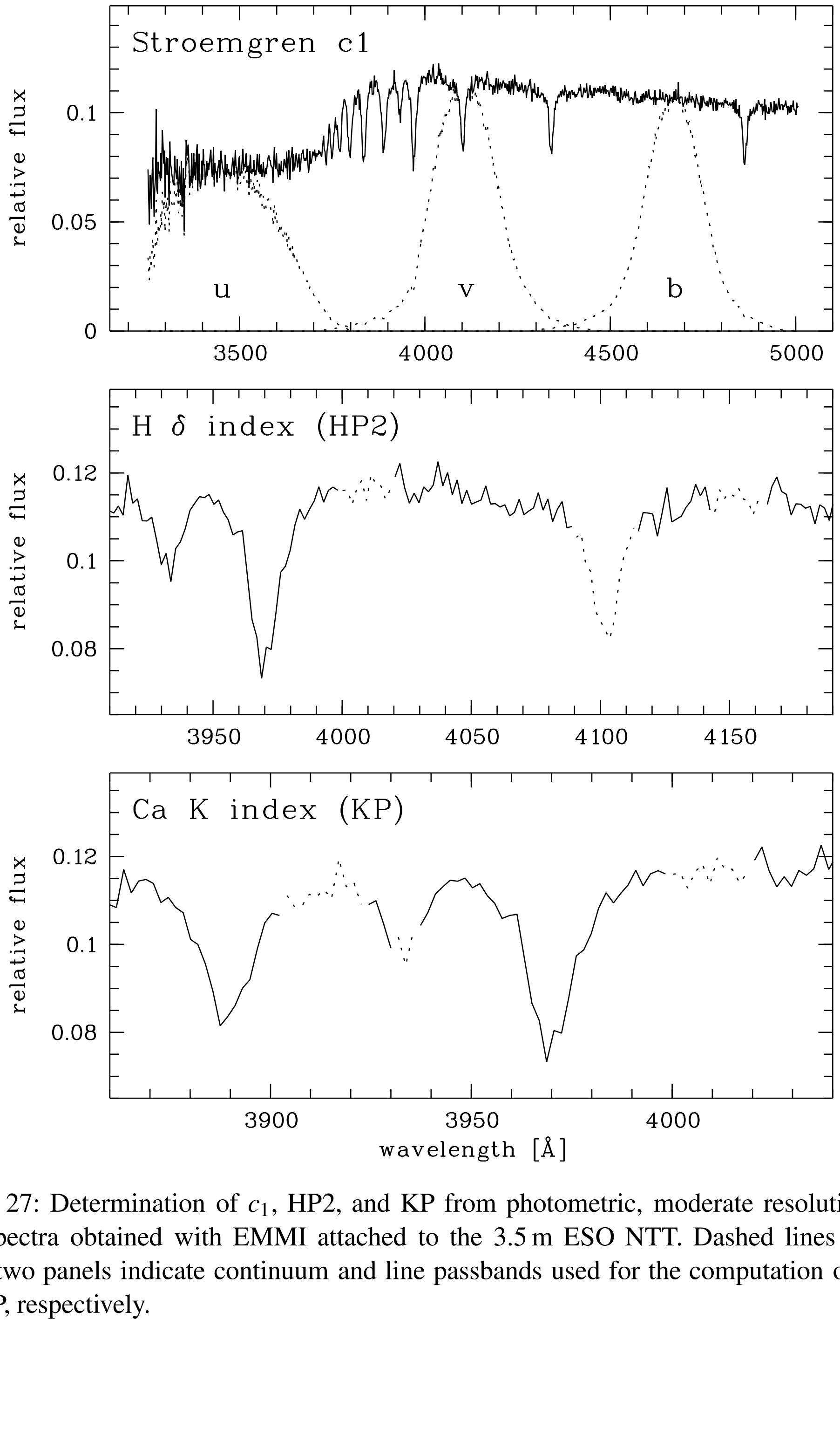

Figure 27: Determination of c_1, HP2, and KP from photometric, moderate resolution ($\sim$ 5 Å) spectra obtained with EMMI attached to the 3.5 m ESO NTT. Dashed lines in the lower two panels indicate continuum and line passbands used for the computation of HP2 and KP, respectively.

is due to the following reasons. In their T_{eff}–$\log g$ diagram (also known as "Kiel diagram"), subgiants (SG) and horizontal branch (HB) stars seem to be missing (see Fig. 28). One can see a few points above the main sequence, but one would expect them to be located a bit higher, and there should be more of them, especially close to the turnoff. It is expected that there are very few HB stars above ~ 6000 K, because of the RR Lyrae gap, but one expects a lot more *red* HB stars to be present. This means that either HB stars and SGs have been *excluded* from the learning and test samples, or there is something wrong with the gravity determination.

In the first case, Snider et al. (2000) would underestimate the error of their method in [Fe/H], since there is a degeneracy between high gravity, low metallicity stars and low gravity, high metallicity stars. That is, at the same temperature, a star with e.g. $[\text{Fe/H}] = -2.0$ and $\log g = 2.0$ has a Ca K line (used as metallicity indicator) as weak as a $[\text{Fe/H}] = -3.0$ and $\log g = 4.8$ star would have.

The accuracy of the $\log g$ determination would be also underestimated as compared to "real life" (that is, as compared to a sample which occupies the Kiel diagram diagram as indicated above), if HB stars and SGs would have been excluded. By just saying that every star at $T_{\text{eff}} < 5000$ K has $\log g = 2.5$, and every star at $T_{\text{eff}} > 5000$ K has $\log g = 4.5$, one would arrive at an average error for $\log g$ which is probably not far away from 0.41 dex, since the numerous dwarfs, having an almost "flat" distribution in the Kiel diagram, dominate the average error.

If HB stars and subgiants have *not* been excluded, and there is an error in the gravity determination, one can not trust neither the claimed $\log g$ accuracy, nor the [Fe/H] accuracy; the latter being the case again because of the confusion between between high gravity, low metallicity stars and low gravity, high metallicity stars.

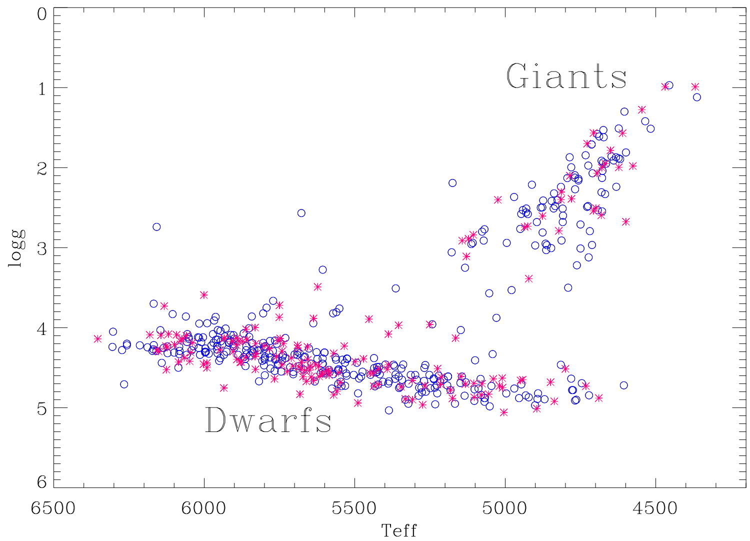

Figure 28: HRD of training and test set of Snider et al. (2000) (their Fig. 2).

A drawback common to all ANN approaches is also that it is very difficult, if possible at all, to understand *how* the classification results were obtained. In case of the determination of stellar parameters from moderate resolution spectra, it would be very interesting to know how the ANN of Snider et al. (2000) carries out the classification in $\log g$, and to learn about the physical reasons behind this. In this way, also any "fake" indicators used in the classification process, like e.g. effective temperature as gravity indicator, as described above, could be identified.

4.5 Effective Yields

As emphasized pointed out by Beers (2000*b*), the *effective yield* (EY) of a detection method is one of the most important properties of a survey for metal-poor stars. EY is defined as follows:

$$\mathrm{EY}_x := \frac{N_{\mathrm{stars}} \text{ with } [\mathrm{Fe/H}] < x}{N_{\mathrm{stars,\ observed}}}.$$

When EYs for different surveys are compared, it is crucial to make sure that the comparison is done on the same abundance scale. In case of the HK survey and the HES, it was found that metallicities derived from the first-pass analysis of the HES follow-up spectroscopy are ~ 0.5 dex *higher* on average, than obtained from the Beers et al. (1999) re-calibration. That is,

$$[\mathrm{Fe/H}]_{\mathrm{HK}} = [\mathrm{Fe/H}]_{\mathrm{HES}} - 0.5. \tag{24}$$

This offset of the scales is primarily due to the different temperature scales adopted in the two methods. In the HK survey, effective temperatures are (implicitly) derived from *BV* photometry, whereas in the HES, Balmer lines are used. The abundance scale previously employed in the HK survey, e.g. in Beers et al. (1992), is known to be an *additional* 0.2 dex lower for the lowest metallicity stars (see Beers et al. 2000*a*).

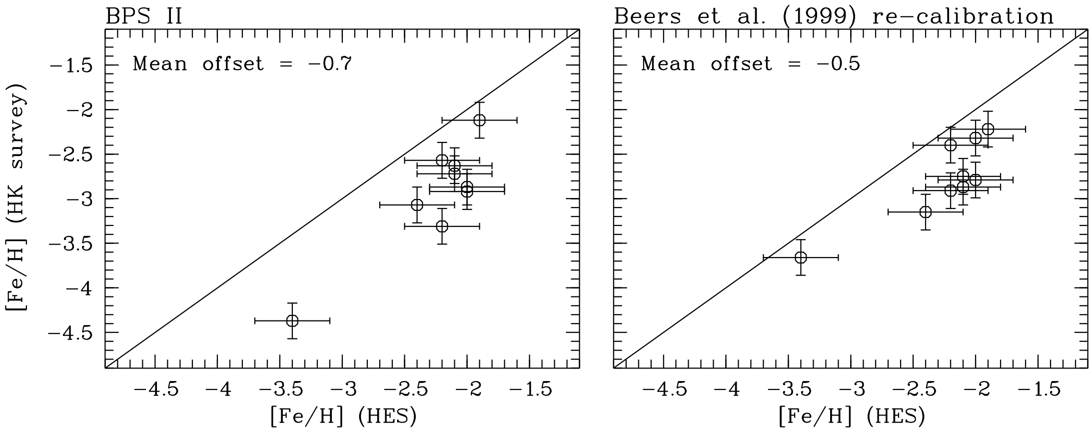

Figure 29: Comparison of HES and HK survey abundance scales. Error bars are 0.2 dex for the HK survey values, and 0.3 dex for HES values.

Thus far, only nine stars have been analyzed with *both* follow-up techniques (see Fig. 29), and there is especially a paucity of comparison objects at $[\mathrm{Fe/H}]_{\mathrm{HES}} < -2.5$. However, the derived trend is consistent for all data points. Only turnoff stars have been used in the comparison; therefore, it can not be excluded that the abundance difference is less (or even more) pronounced for cooler stars.

For this discussion, we restrict our EY comparison to turnoff stars in the color range $0.3 < B-V < 0.5$, and carry out the comparison after an offset of 0.5 dex has been subtracted from the HES metallicities.

In order to explore what the *highest possible* EY in the HES is, we observed a sample of 56 HES metal-poor candidates with EMMI at the ESO NTT. The stars were selected by automatic classification, by using a set of 8 spectral features. These were selected by hand, because at that time the search for the best feature combinations was not yet completed.

Survey/selection method	$EY_{-2.0}$	$EY_{-2.5}$
HK survey/without $B-V$ pre-selection	11 %	4 %
HK survey/with $B-V$ pre-selection	32 %	11 %
HES/automatic classification	80 %	27 %

Table 9: Comparison of effective yields (EY) of metal-poor turnoff stars of the HK survey and the HES. [Fe/H] is on the re-calibrated HK survey scale of Beers et al. (1999).

The automatic classification programs were fed only with a subset of all spectra present on each HES plate. As already mentioned, only spectra with $S/N > 10$ and $B \gtrsim 14$ are considered. Moreover, spectra outside of the range $0.3 < B-V < 0.5$ are excluded, where $B-V$ is known to ± 0.1 mag from the calibration of `x_hpp2`.

Below we summarize the selection criteria for metal-poor stars in the HES for the selection by automatic classification. Pre-selection of spectra to which automatic classification procedures are applied is done by criteria (1)–(3); (4) and (5) use the results of automatic classification, and (6) is a rejection criterion corresponding to a χ^2 test at a 3σ level.

(1) $0.3 < B-V < 0.5$

(2) $(S/N)_{\rm HES} > 10 \Longleftrightarrow B \lesssim 16.5$

(3) Photographic density D below saturation threshold

(4) $\log g \geq 3.8$

(5) $[\mathrm{Fe/H}] \leq -2.7$

(6) *a.i.* < 0.99.

Only candidates assigned classes a or b in the visual inspection have been observed. EY of stars at $[\mathrm{Fe/H}] < -2.0$ for this sample is 80 % (see Tab. 9)! This has to be compared with 11 % or 32 % in the HK survey, depending on whether a pre-selection based on $B-V$ color has been made or not, respectively.

4.6 Discussion and Conclusions

Selection of metal-poor candidates at the main-sequence turnoff in the HES by automatic classification is $\sim 3\times/\sim 7\times$ more efficient as compared to visual inspection in the HK survey with/without pre-selection by *BV* photometry. This is very remarkable considering the fact that the spectral resolution of the HES is $2\times$ *lower* than in the HK survey. Reasons for the higher efficiency are the larger spectral coverage of the HES, better quality of the HES spectra, and the automated, quantitative selection, which is presumably more precise than the selection by eye. Moreover, we have intentionally observed class a and b candidates only, because we wanted to explore what the *maximum possible* efficiency is. Simulations we have carried out indicate that, in exchange for a high EY of truly metal-poor stars, one has to sacrifice completeness of the candidate sample on the order of 50 %. Thus, the EY of a selection aimed at compiling a *complete* sample of metal-poor stars by means of including class c candidates, and also candidates from complementary selection methods (e.g. the feature calibration method), will be proportionately lower.

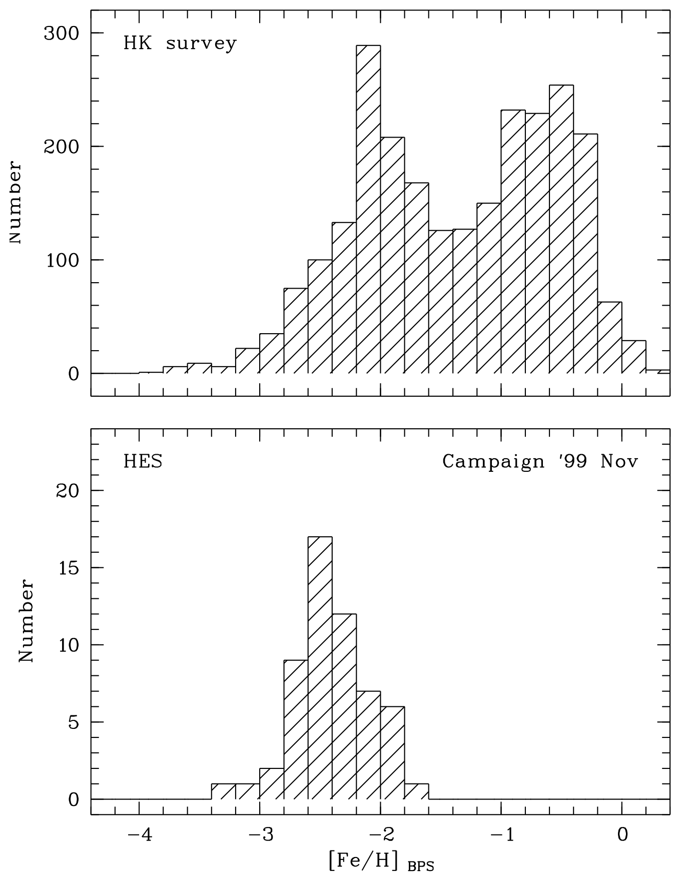

Figure 30: Metallicity distribution function of stars in the color range $0.3 < B-V < 0.5$ from the HK survey (upper panel), and of a sample of 56 stars selected by automatic classification in the HES. Note the prominent lack of high metallicity ([Fe/H] > -1.5) stars in the HES sample compared to the HK survey sample.

It is possible to derive rough stellar parameters for stars in the range $5200\,\mathrm{K} < T_{\mathrm{eff}} < 6800\,\mathrm{K}$ directly from HES spectra by either automatic classification, or the calibrated feature approach. Experiments are carried out to do the same for digitized HK survey spectra, by using ANNs (Rhee et al. 1999). However, since only a small spectral range is covered by the HK survey, so that much less information, and in particular no colour information, is included in those spectra, it is even more challenging to do this in the HK survey.

The follow-up technique used in the HK survey results in determinations of [Fe/H] precise to ± 0.2 dex; the accuracy of the HES technique remains to be evaluated. The advantage of the "all in one shot"-technique used in the HES is that no photometry is needed in addition to moderate resolution spectra. However, a drawback is that no useful radial velocities can be measured from spectra obtained with the wide slit, since the object position within the slit is not precisely known, so that unknown zero-point offsets in wavelength occur.

In follow-up campaigns carried out so far, 90 metal-poor stars were discovered; 11 are unevolved stars at $[\mathrm{Fe/H}]_{\mathrm{HK}} \leq -3.0$ (see Tab. 24 in Appendix A). In the HK survey, 37 stars with $[\mathrm{Fe/H}]_{\mathrm{HK}} \leq -3.0$, and $0.3 < (B-V)_0 < 0.5$ were found (Beers 2000, priv. comm.). We thus increased the number of unevolved, extremely metal-poor stars already noticeably.

When compiling target lists for high-resolution observations, combining stars from different surveys, it is important to take into account their different abundance scales. An offset of 0.5 dex has to be subtracted from [Fe/H] estimates obtained from the HES follow-up, when they are compared with [Fe/H] values derived from the HK survey.

Since the limiting magnitude for metal-poor stars in the HES is ~ 17.0, and "saturated" objects are excluded from the selection procedure, the HES provides mainly fainter candidates, in the magnitude range $14.0 < B < 17.0$, whereas the HK survey is able to provide bright candidates in the range $11.0 < B < 15.5$.

The HES is ~ 1.5 mag deeper than the HK survey. Therefore, the former can increase the total survey volume for metal-poor stars by a factor of 8, taking into account common areas and the magnitude ranges of both surveys. We estimate that the total number of stars at $[\mathrm{Fe/H}]_{\mathrm{HK}} < -3.0$ known today, ~ 100, can be increased to ~ 400 by the HES, provided that follow-up observations can be obtained for all candidates. Extension of the procedures described above for the inclusion of cooler stars, and complementation of the selection by automatic classification with alternative procedures such as the Ca K index method, could easily increase the number of stars with $[\mathrm{Fe/H}]_{\mathrm{HK}} < -3.0$ to even higher numbers.

4.7 Outlook

4.7.1 Moderate-Resolution Spectroscopic Follow-Up

The bottleneck in searching extremely metal-poor stars are spectroscopic follow-up observations, because even in objective prism surveys with relatively high spectral resolution, like the HK survey, or the HES, it becomes difficult to detect the strongest metal line, i.e. Ca K, at $[\mathrm{Fe/H}]_{\mathrm{HK}} \lesssim -2.0$. Therefore, one is basically "blind" below this metallicity, i.e., one can not distinguish between e.g. a $[\mathrm{Fe/H}]_{\mathrm{HK}} = -2.5$ star and a star of $[\mathrm{Fe/H}]_{\mathrm{HK}} < -3.0$. Unfortunately, the low metallicity tail of the halo metallicity distribution function (MDF) peaks around $[\mathrm{Fe/H}]_{\mathrm{HK}} = -2.2$ (see Fig. 30), so that one has to "fight" against stars of moderately low metal abundance when searching for extremely metal-poor stars. From Tab. 1 in Beers (1999) it can be seen that even if it is possible to exclude all stars of $[\mathrm{Fe/H}]_{\mathrm{HK}} > -2.0$ from the candidate sample, which is already quite challenging, one has to observe ~ 10 stars for finding a star of $[\mathrm{Fe/H}]_{\mathrm{HK}} < -3.0$, and for each star of $[\mathrm{Fe/H}]_{\mathrm{HK}} < -3.5$, one has to observe ~ 60 stars.

For these reasons, it is impossible to make a considerable progress in finding extremely metal-poor stars by using the capacities of a single observatory, like ESO. Therefore, we have established a number of international collaborations by which we gain access to non-ESO telescopes. The telescopes involved are listed below.

ESO Telescopes Due to continued technical problems with EMMI, we will use EFOSC2 attached to the 3.6 m telescope in the future only. Now that we were able to prove that our selection methods work, we received for the first time as many nights as we have requested, i.e. 5 nights per semester. Since our program was proposed as long term project, we expect that we will continue to receive a similar amount of observing time over the next years. Experience at the NTT has shown that it is possible to observe ~ 30 candidates per night in average weather conditions. Therefore, we expect to get spectra of up to ~ 300 candidates per year at ESO.

UK Schmidt/6dF The multi-object spectrograph 6dF (Watson 1998), mounted at the UK Schmidt telescope, is scheduled to come into operation in November 2000. With 6dF it is possible to observe up to 150 targets in a field of view of $6° \times 6°$. At the spectral resolution required for metal-poor star follow-up, objects down to $B \approx 16.5$ can be observed. This would lead to two sets of 4×1 h exposures per night. At $B > 16.5$, the surface density of metal-poor stars from the HES and HK survey combined is ~ 30 per 6dF field (the remaining fibers could be filled with other HES targets, e.g. candidate FHB/A stars, and candidate white dwarfs). It is thus possible to observe ~ 60 metal-poor candidates per night, which is twice as much as is possible with single slit spectroscopy at a 4 m class telescope. In collaboration with M. Bessell (ANU), we will submit a first proposal in summer 2000. Should it be possible to get ~ 2 weeks of observing time per year, about 800 candidates per year could be observed.

2.3 m MSSSO Telescope Again in collaboration with M. Bessell, and J. Norris (ANU) we will ask for observing time at the 2.3 m MSSSO telescope in the period August–October 2000. At that time, 6dF will not yet be in operation. It is probably neither recommended, nor promising to continue submitting proposals for the 2.3 m *after* 6dF is available, so that we will use this telescope only temporarily. Two nights in May have already been granted to us.

CTIO/KPNO 4 m The author is Co-I of a "NOAO Survey Program" aiming at follow-up of metal-poor candidates from the HK survey and the HES. In that proposal we asked for 10 nights per year at the CTIO 4 m, and additional 5 nights per year at the KPNO 4 m, over a period of 5 years. Should the proposal be accepted, we would be able to observe some 500 HES targets per year.

CFHT In a collaboration with D. VandenBerg (University of Victoria, Canada) we have access to the CFHT. A first proposal asking for 5 nights in December 2000 is about to be submitted.

Taking into account a time loss of $\sim 1/3$ of due to bad weather or technical problems, we estimate that $\sim 3\,500$ HES candidates will be observed within the next 3 years, which should at least double the number of stars of $[\mathrm{Fe/H}]_{\mathrm{HK}} < -3.0$.

4.7.2 High-Resolution Spectroscopy

VLT/UVES A first proposal asking for observing time in period 65 (April–October 2000) has been *rejected*. A refined proposal will be submitted in the next period.

Two HES metal-poor stars have already been observed with VLT UT2 in the course of UVES science verification. These stars are HE 1303$-$2708 and HE 1353$-$2735. The spectra have $R = 45\,000$, and $S/N > 50$ per pixel throughout the whole spectral range covered, which is $\lambda = 5940$–9750 Å. An additional $S/N > 50$ spectrum in the range $\lambda = 4090$-5310 Å has been taken for HE 1353$-$2735. These spectra are currently being reduced and will be analyzed soon.

Subaru/HDS The instrument group of the High Dispersion Spectrograph (HDS), scheduled to be mounted at the Subaru telescope in February 2000, has ~ 40 nights of test observing time available to them. We (and other people, working in other fields of astronomy) were asked to submit proposals for observations of HES metal-poor stars using this time. We expect to receive first data by mid-2000. These observations are seen as start of a long-term collaboration from both sides.

Keck/HIRES J. Cohen from the California Institute of Technology has access to the Keck telescope and is interested in collaborating on high-resolution spectroscopy of HES metal-poor stars with HIRES. A first proposal for 4 nights in the period August–September 2000 has been submitted.

Acknowledgements

I thank T. Beers for a trustful and close collaboration. I am especially appreciating that he provided me with the result of almost two decades of work, his master list of all HK survey stars that had follow-up spectroscopy and/or photometry. This list is largely unpublished. Tim also smoothed my English in those parts of this sections that have been taken from Christlieb & Beers (2000).

The first paragraph of Sect. 4.2 is an adapted version of a paragraph in Christlieb & Beers (2000) written by T. Beers. The description of the HK survey candidate selection (2nd paragraph on page 37), and Sect. 4.4.1, are from the same source, and were included in original form.

J. Reetz and T. Gehren contributed to the search for metal-poor stars in the HES by providing model atmospheres, SIU (a tool for spectrum analysis), repeated hospitality at their institute, and many discussions.

I thank J. Norris for bringing the idea of deriving Strömgren c_1 from photometric spectra to my attention.

References

Beers, T. C. (1999), Low-Metallicity and Horizontal-Branch Stars in the Halo of the Galaxy, *in* B. Gibson, T. Axelrod & M. Putman, eds, 'The Third Stromlo Symposium: The Galactic Halo', Vol. 165 of *ASP Conf. Ser.*, pp. 202–212.

Beers, T. C. (2000*a*), Observational constraints on the Nature of the first stars – final comments, *in* A. Weiss, T. Abel & V. Hill, eds, 'The First Stars, Proceedings of the second MPA/ESO workshop', Springer, Heidelberg.

Beers, T. C. (2000*b*), Population III by popular demand – progress and previews, *in* A. Weiss, T. Abel & V. Hill, eds, 'The First Stars, Proceedings of the second MPA/ESO workshop', Springer, Heidelberg. astro-ph/9911171.

Beers, T. C., Chiba, M., Yoshii, Y., Platais, I., Hanson, R. B., Fuchs, B. & Rossi, S. (2000*a*), 'Kinematics of Metal-Poor Stars in the Galaxy. II. Proper Motions for a Large Non-Kinematically Selected Sample', AJ, submitted.

Beers, T. C., Preston, G. W. & Shectman, S. A. (1992), 'A search for stars of very low metal abundance. II.', *AJ* **103**(6), 1987–2034.

Beers, T. C., Rossi, S., Norris, J. E., Ryan, S. G. & Shefler, T. (1999), 'Estimation of Stellar Metal Abundance. II. A Recalibration of the Ca II K Technique, and the Autocorrelation Function Method', *AJ* **117**, 981–1009.

Beers, T. C., Suzuki, T. K. & Yoshii, Y. (2000*b*), The Light Elements Be and B as Stellar Chronometers in the Early Galaxy, *in* L. da Silva, M. Spite & J. R. de Medeiros, eds, 'to appear in: IAU Symposium 198: The Light Elements and Their Evolution', ASP Conf. Ser., ASP, San Francisco.

Bond, H. E. (1981), 'Where is population III?', *ApJ* **248**, 606–611.

Cayrel, R. (1996), 'The first generation of stars', *A&A Rev.* **7**, 217–242.

Christlieb, N. & Beers, T. C. (2000), Ongoing Large Surveys for Metal-Poor Stars in the Galactic Halo, *in* M. Takada-Hidai, ed., 'to appear in: 2nd Subaru HDS Workshop', National Astronomical Observatory, Tokyo. astro-ph/0001378.

Cowan, J. J., Pfeiffer, B., Kratz, K.-L., Thielemann, F.-K., Sneden, C., Burles, S., Tytler, D. & Beers, T. (1999), 'R-Process Abundances and Chronometers in Metal-poor Stars', *ApJ* **521**, 194–205.

Fuhrmann, K. (1999), 'The Disk Populations in the [Mg/H]-[Fe/Mg] Plane', *Ap&SS* **265**, 265–268.

Norris, J. E. & Freeman, K. C. (1979), 'The cyanogen distribution of the giants in 47 Tucanae', *ApJ* **230**, L179–L182.

Qu, Y., Snider, S., von Hippel, T., Sneden, C., Lambert, D., Beers, T. & Rossi, S. (1998), 'Neural Network Techniques Applied to Low Resolution Spectra of Halo Stars', *BAAS* **193**, #44.09.

Ratnatunga, K. U. & Freeman, K. C. (1989), 'Field K Giants in the Galactic Halo. II. Improved Abundance and Kinematic Parameters', *ApJ* **339**, 126–148.

Rhee, J., Beers, T. C. & Irwin, M. J. (1999), 'Automatic Identification, Classification, and Abundance Estimation for Metal-Poor Stars in the Galaxy from Objective-Prism Spectroscopy Using a Neural Network Analysis', *BAAS* **31**, 971.

Shigeyama, T. & Tsujimoto, T. (1998), 'Fossil Imprints of the First-Generation Supernova Ejecta in Extremely Metal-deficient Stars', *ApJ* **507**, L135–L139.

Snider, S., Qu, Y., Allende-Prieto, C., von Hippel, T., Beers, T. C., Sneden, C., Lambert, D. L. & Rossi, S. (2000), 'Teff, log g, [Fe/H] Classification of Low-Resolution Stellar Spectra Using Artificial Neural Networks', *in* 11th Cambridge Workshop on Cool Stars, in press (astro-ph/9912404).

Tsujimoto, T., Shigeyama, T. & Yoshii, Y. (2000), 'Probing the Site for r-Process Nucleosynthesis with Abundances of Barium and Magnesium in Extremely Metal-Poor Stars', ApJ Letters, in press (astro-ph/0001220).

Watson, F. (1998), 'Board's green light for 6dF', *AAO Newsletter* (85), 11–12.

5 A Large, Flux-Limited Sample of Carbon Stars

5.1 Introduction

Since carbon can reach the surface of an isolated star only in late evolutionary states, it has long been assumed that all carbon stars are *giants*. Due to their high luminosity it is possible to detect them at large distances: Brewer et al. (1996) have identified C stars even in the local group galaxy M31. As members of our own Galaxy, they are useful as tracers for the kinematics of the halo (e.g., Mould et al. 1985; Morrison et al. 2000), and as "test particles" for weighing the Galactic potential well. For these purposes, faint high galactic latitude carbon (FHLC) stars have been searched by objective prism surveys (e.g., Sanduleak & Pesch 1988; MacAlpine & Lewis 1978) and in the CCD survey of Green et al. (1994).

However, there was one exception known for a long time. Trigonometric parallax measurements for the carbon star G77-61 showed that this star, having $M_V = +9.6$ (Dahn et al. 1977), lies close to the main sequence. Another dwarf carbon star (dC), KA 2, was discovered in the 1980s by Ratnatunga (1983) in the course of an objective prism survey, and was proven to be a dwarf by its high proper motion (p.m.). In the early 1990s, a real "inflation" of dC discoveries took place: Green et al. (1991, 1992) discovered 4 further dCs, again due to their high p.m. Warren et al. (1993) list another 3 possible dCs, but however, the p.m. measurement of only one of them has a significance $> 3\sigma$. Heber et al. (1993) reported that PG 0824+289, a hot DA white dwarf, is in a double-line spectroscopic binary with a dC companion of absolute magnitude very similar to G77–61 ($M_V \sim +10$). Another DA/dC composite system, CBS 311, was discovered by Liebert et al. (1994). Margon et al. (1999) recently reported the discovery of one certain, and one likely dC in the commissioning data of the Sloan Digitized Sky Survey (SDSS).

From its radial velocity variation, G77-61 is known to be a binary; Dearborn et al. (1986) report a period of 245 days. This means that three dCs (the other two being PG 0824+289 and CBS 311) out of ~ 10 dCs are *known* to be members of binary systems. Therefore, the most reasonable explanation of the prominent carbon bands in these dwarf spectra is mass transfer from a companion during the companion's second ascent of the giant branch. The enhanced Barium abundance and the wide range of Carbon isotope ratios observed in 6 dCs by Green & Margon (1994) support this scenario.

With about 10 dC stars now known from an incomplete hodgepodge of surveys and serendipity, the conclusion seems inescapable that many more C giants than C dwarfs are presently known only by virtue of the much greater luminosities of the former class. From a p.m. survey of 39 FHLC stars, Green et al. (1992) concluded that the local space density of dCs probably surpasses that of all other types of C stars combined. They found 5 stars (or 13 %) out of their sample to be dwarfs. Assuming $M_V = +10$ for dwarfs, an average of $M_V = +1$ for all other C stars, and assuming that the sample is flux-limited, this would mean that the space density of dCs is $\sim 37\,000$ times higher than the space density of all other C stars! This conclusion is *conservative*, since disk dCs may remain in the FHLC star sample, with p.m.s below the detection threshold. Thus, contrary to the formerly prevailing paradigm, dwarf C stars are likely to be the numerically dominant type of carbon star in the Galaxy.

The discovery of so many dCs, and the remarkable similarity of their spectra to those of C giants means that care must be taken to distinguish dwarfs from giants in FHLC star samples intended for dynamics (Green et al. 1992). As innocent bystanders in a mass transfer binary (MTB) system, dC's spectroscopic and orbital properties provide valuable fossil records of the history and evolution of an extinct population of AGB stars. Even using conservative constraints on the shape of the initial mass function and binary fractions in the disk and spheroid, we may expect mass transfer to have occurred in a large number of such systems (de Kool & Green 1995). The majority of these low mass, post MTB stars could be M dwarfs, in which the evidence for past mass transfer may be subtle, or even undetectable. In dCs, the spectroscopic signature of extensive mass transfer is glaringly obvious. However, not all dCs have detectable p.m.s, so other luminosity/distance indicators are needed. Comparison of high resolution optical spectra to model atmospheres might seem promising, but most dCs have $V \geq 15$, and thus spectroscopy of sufficient resolution for luminosity estimates is difficult. Green et al. (1992) have shown that high p.m. FHLC stars may exhibit distinctive JHK colors appropriate to late-type dwarfs, suggesting infrared colors as a possible luminosity indicator. However, the sample of known dCs is still too small to draw any definitive conclusions.

Larger samples of all types of FHLC stars are thus of interest: giants as tracers of outer halo dynamics and structure (as can be seen in Fig. 31, C stars with distances of up to ~ 30 kpc can be found in the HES), and dC stars in particular to improve our fledging understanding of their evolution, and to investigate possible luminosity indicators other than p.m. We are therefore undertaking a two-part investigation. We select C stars in the HES with automated selection techniques, to compile a large, uniformly selected, and flux-limited sample of FHLC stars. We complement this sample with recent epoch CCD astrometry, to measure p.m.s for as many objects as possible, and thereby separate the dCs from C giants.

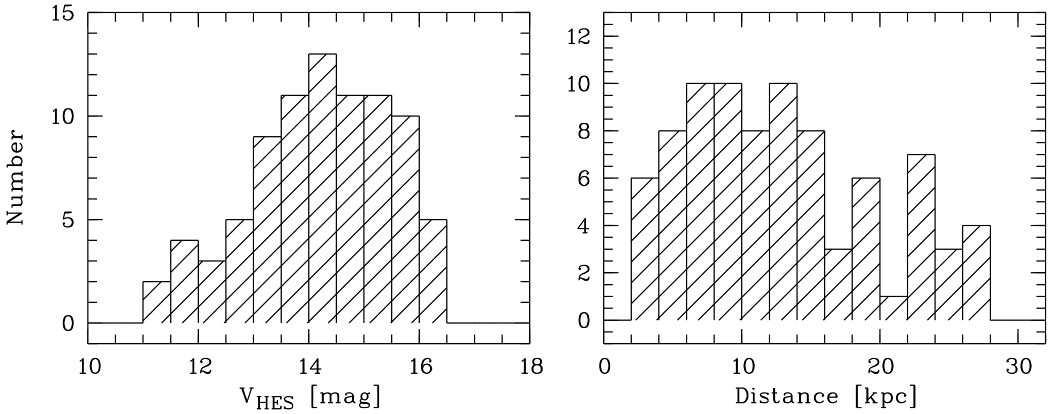

Figure 31: Magnitude and distance distribution of 86 HES carbon stars without significant p.m. V has been derived from the HES spectrum, using Eq. 1 for conversion between B_J and B, and the $B-V$ calibration of dx_hpp2 for red stars given in Tab. 6. Rough distances have been derived by assuming $M_V = -1.0$.

5.2 Carbon Star Selection

Carbon stars can be identified in the HES with high confidence without follow-up slit spectroscopy, based on their strong C_2 and CN bands. A representative collection of HES spectra of C stars is shown in Fig. 37. Most importantly, C stars can be distinguished from other late type stars, e.g. M or S stars, even if only weak C bands are present in their spectra (see Fig. 32).

Moreover, C stars can be distinguished reliably from white dwarfs of type DQ (hereafter shortly referred to as DQs), since the latter usually have a much bluer continuum (see Fig. 37). The average $U-B$ of HES C stars is ~ 0.9, more than 90 % have $U-B > 0.5$, and there is *no* C star of $U-B < 0$ in the HES sample. McCook & Sion (1999) list 49 DQs, of which 30 have an available $U-B$ measurement. The average $U-B$ of those is -0.58, i.e., $\sim 1.5^{\mathrm{m}}$ away from the average $U-B$ of the HES C star sample. However, 4 objects (i.e., 13 % of the 30 objects with available $U-B$) have $U-B > 0.0$.

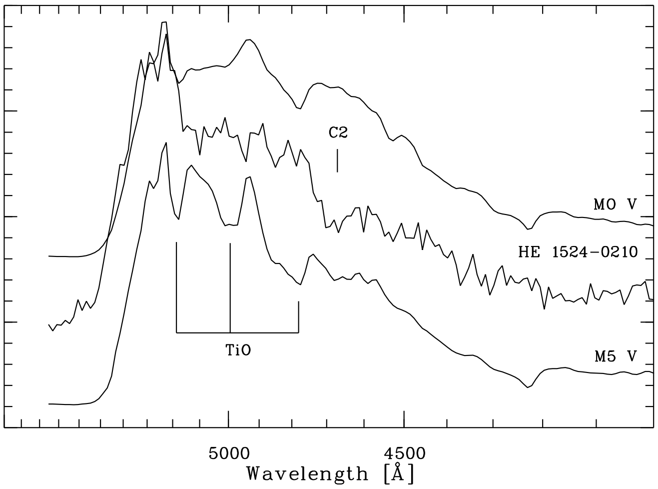

Figure 32: Comparison of HES spectra of the C star HE 1524−0210, exhibiting a weak C band only, with two M stars. The abscissa is density in arbitrary units.

With a rough estimate of the surface density we can quantify by how many "red" ($U-B>0.0$) DQs the HES C star sample is expected to be contaminated. First of all, we have to take into account that the ratio of northern hemisphere to southern hemisphere DQs is unbalanced in McCook & Sion (1999), as much as the *total* catalog is. This is because the southern hemisphere so far has been surveyed less extensively for white dwarfs. Assuming that the northern hemisphere sample of DQs is complete, we derive a surface density of 9 DQs brighter than $V = 16.5$ in 20000 deg^2, i.e. $4.5 \cdot 10^{-4}$ deg^{-2}. Hence, the surface density of $U-B>0.0$ DQs is $5.9 \cdot 10^{-5}$ deg^{-2}, and we expect 0.45 DQs to be present on all 380 HES plates (effective area 7700 deg^2). Even if we assume that the sample of DQs known so far is by a factor of 2 incomplete, we statistically expect less than 1 DQ to be present in the final HES C star sample.

We select carbon star candidates in the HES by two methods: A carbon band index method (Sect. 5.2.1), and template matching (Sect. 5.2.2). We inspect all automatically selected spectra individually to identify any remaining plate artifacts, to reject the few overlapping spectra that have not been recognized by the automatic overlap detection procedure (see p. 9), and to verify their C star nature.

5.2.1 C Band Index Method

In the carbon band index method, we select stars when the mean S/N in the relevant wavelength range is >5 per pixel and both of the C_2 bands $\lambda\lambda$5165, 4737, or both of the CN bands $\lambda\lambda$4216, 3883 are stronger than a selection threshold. Band strengths are measured by means of line indices – ratios of the mean photographic densities in the carbon molecular absorption features and the continuum bandpasses shown in Fig. 33, and listed in Tab. 10. The use of *pairs* of indices prevents confusion with plate artifacts, e.g., scratches. It is very unlikely that two such artifacts are present at the positions of two molecular bands. Selection boxes in the $I(C_2\,\lambda 5165)$ versus $I(C_2\,\lambda 4737)$ and $I(\mathrm{CN}\,\lambda 4216)$ versus $I(\mathrm{CN}\,\lambda 3883)$ planes have been chosen well-separated from the dense locus of "normal" stars (see Fig. 34).

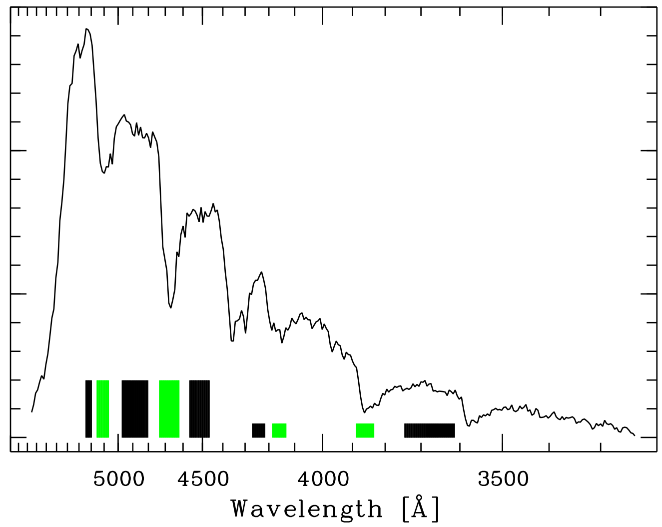

Figure 33: HES objective prism spectrum of the R-type carbon star CGCS 2954 (Stephenson 1989), illustrating the positions of continuum (black) and band (grey) bandpasses defining the C_2 (high boxes) and CN (flat boxes) line indices. The abscissa is density in arbitrary units.

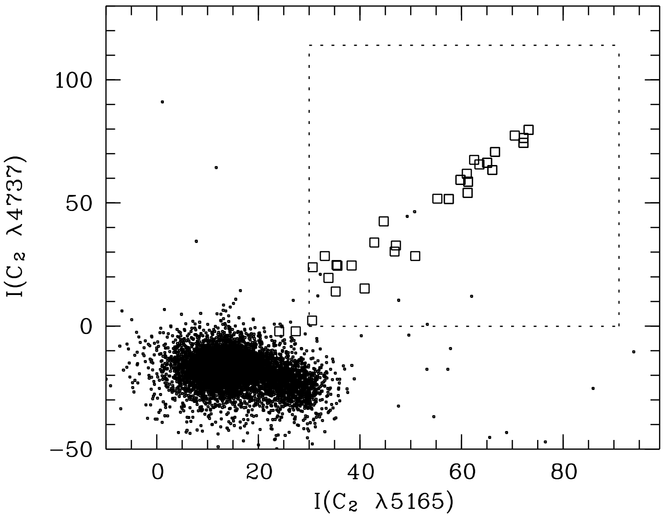

Figure 34: Selection of carbon stars in the $I\,(C_2\ \lambda 5165)$ versus $I\,(C_2\ \lambda 4737)$ plane. Band strengths are measured by line indices in arbitrary units. '·' – all spectra on a randomly chosen HES plate, '□' – test sample of known FHLC stars present on HES plates (see Tab. 12), dashed box – selection region. Spectra in which only *one* high C_2 band index value has been measured suffer either from an overlapping spectrum, or from a plate artifact. The selection in the $I\,(\mathrm{CN}\ \lambda 4216)$ versus $I\,(\mathrm{CN}\ \lambda 3883)$ plane is done analogously. The two test sample objects outside the selection box are CGCS 525 and CGCS 3180. They are selected by CN band indices (see Tab. 12).

Passband	Use for band index			
	C_2 5165	C_2 4737	CN 4216	CN 3883
5190–5240 Å	cont			
5060–5150 Å	flux			
4800–4970 Å	cont	cont		
4620–4730 Å		flux		
4460–4560 Å		cont		
4210–4270 Å			cont	
4130–4180 Å			flux	
3830–3890 Å				flux
3610–3740 Å				cont

Table 10: Wavelengths of C band passbands used for computation of band indices.

5.2.2 Template Matching

In the HES, some care must be taken when objects with p.m. shall be selected. This is because the input catalog for extraction of objective prism spectra is generated by using the Digitized Sky Survey I (DSS I). Therefore, large proper motions and/or large epoch differences between HES and DSS I plates (13.5 years on average, see Fig. 35) may result in non-detection of objects in the HES (if $\mu_\alpha \cdot \Delta t_{\text{HES-DSS I}} \gtrsim 4''$, i.e., > 3 pixels), and/or an offset of the wavelength calibration zero point, resulting in wrong C band measurements. Therefore, we use a template matching algorithm (see e.g. Castleman 1979, for the concept of template matching), which compensates for offsets in dispersion direction by *shifting* the templates through each spectrum.

As is shown in Fig. 36, p.m.s of a typical halo object ($<u>=<w>= 0$ km/s; $<v>\sim 200$ km/s) result mainly in offsets along declination (i.e., parallel to the HES dispersion direction), and only small offsets in R.A.

We have generated 7 carbon star templates by using a wide range of carbon star types (see Fig. 37). For these spectra a (pseudo-)continuum is determined by median filtering, and subsequent smoothing with a narrow Gaussian filter. These templates are shifted in the range $-20\ldots+20$ pixels in sub-pixel steps along the dispersion direction of (again continuum divided) HES spectra. The shift range corresponds to $\pm 27''$.

For each shift step j, realized by template offsets, the template scaling factor c_j is computed by means of a least squares fit, i.e.,

$$\chi_j^2 = \sum_{i=1}^{n_j} \frac{(s_i - c_j \cdot t_{i-j})^2}{\sigma_i^2} \stackrel{!}{=} \text{min}. \tag{25}$$

s_i are the pixels of the spectrum, and t_i the template pixels; σ_i is the pixel-wise noise. The sum runs over all n pixels for which the shifted template is defined. The amplitude of the pixel-wise noise as a function of density D is determined plate-wise using an absorption line free spectral region of A-type stars (Sect. 2.2.6; see also Christlieb 1995). Minimizing the χ^2 sums for each shift step yields template scaling factors c_j,

$$c_j = \frac{\sum_{i=1}^{n_j} \frac{s_i \cdot t_{i-j}}{\sigma_i^2}}{\sum_{i=1}^{n_j} \frac{t_{i-j}^2}{\sigma_i^2}}. \tag{26}$$

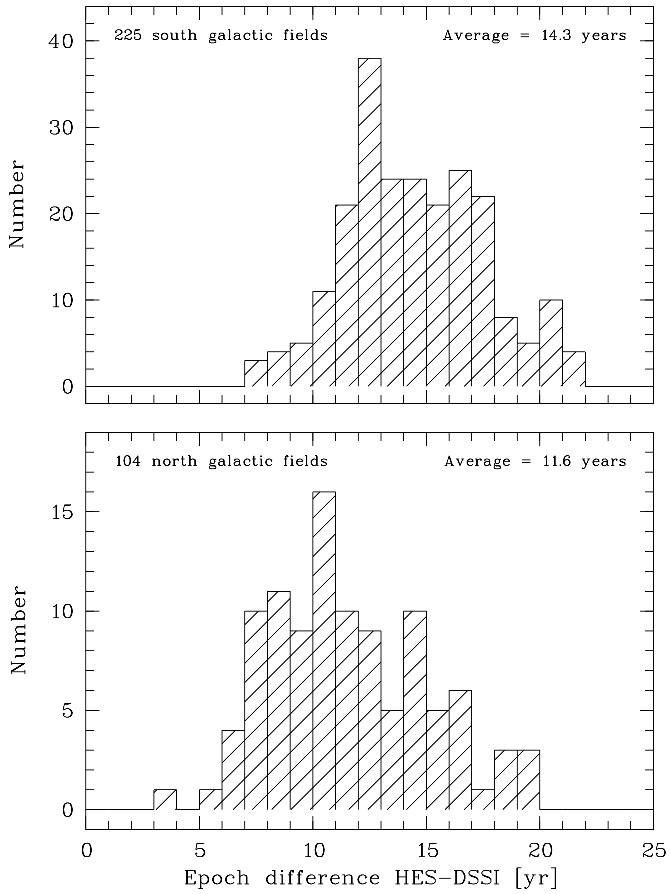

Figure 35: Histograms of epoch differences Δt between HES plates and DSS I plates used for spectral reduction. Δt is 2.7 yr less on average for the 104 HES plates of north Galactic fields. The total average for all 329 plates is 13.5 yr.

We adopt the template scaling factor c_j, which has the lowest χ^2 probability $P(\chi_j^2|\nu_j)$. That is, we look for the offset at which the template "matches best". ν_j is the number of degrees of freedom, i.e. $\nu_j = n_j - 1$.

Cutoff template scaling factors c_{min} are determined plate-wise, and for each template, by computing average template scaling factors $\overline{c}$, and standard deviations σ_c. We use a 5σ cutoff, i.e.

$$c_{\mathrm{min}} = \overline{c} + 5\sigma_c. \tag{27}$$

A spectrum is selected as C star candidate, if the template scaling factor for *at least one* template is above the cutoff. Note that template matching is not carried out for HES spectra above the saturation threshold, because we do not have an estimation of pixel-wise noise for these.

5.3 Testing the Automatic Selection

We tested the automatic selection extensively, and by various methods. In Sect. 5.3.1, we investigate the selection probability as a function of $\mu_\delta \Delta t$ for both selection algorithms. In Sect. 5.3.2 we derive the plate-wise selection probability for halo dCs on HES plates. The results of tests with "real" objects are given in Sect. 5.3.3, and in Sect. 5.3.4 we investigate the selection efficiency.

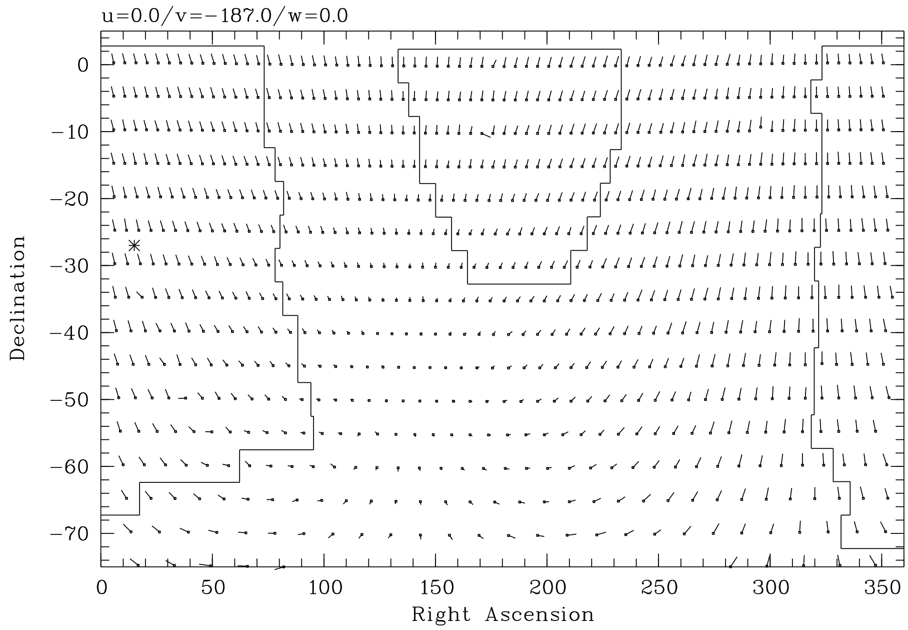

Figure 36: Simulation of p.m. directions.

5.3.1 Dependence of Selection Probability on $\mu_\delta \Delta t$

As a test sample for our investigation of the dependence of the selection probability on $\mu_\delta \Delta t$, we used a sample of 78 C stars from HES 44 plates *without* significant p.m. (as measured in the follow-up campaign '99 April at the ESO 2.2 m; see Sect. 5.5), below saturation threshold, i.e. object classes `stars` and `ext`. These were shifted in 1 pixel (= $1''.35$) steps through the range $-700\mu\mathrm{m} < x < +700\mu\mathrm{m}$, corresponding to $-47''.25 < \mu_\delta \Delta t < 47''.25$. At each shift step, both selection algorithms have been applied.

The result is displayed in Fig. 38. The combined relative selection rate of both selection methods is $> 50\,\%$ for $-4''.5 < \mu_\delta \Delta t < 2''.5$. At larger $\mu_\delta t$, the selection rate is nonzero only for the selection by template matching, with exception of two regions with very high $|\mu_\delta \Delta t|$ (where it is unlikely to find a star in reality). The peak selection rate for template matching, around $\mu_\delta \Delta t = 0$, is hardly above 50 %, and is $\sim 30\,\%$ at larger $|\mu_\delta \Delta t|$. Since the test sample has originally been selected by the C band index method, the peak selection rate for this method obviously *has* to be 100 %.

5.3.2 Decrease of Selection Probability for Halo dCs

In order to estimate how many dCs are expected to be missed in our survey due to the epoch difference problem, we carried out a simulation study in which the plate-wise selection function for halo dCs was determined. The simulation is similar to that described in Green et al. (1992). We let some dwarfs "fly through space" with halo kinematics, as given by Norris (1986). For the solar neighborhood, he gives

$$v_{\mathrm{rot}} = 37 \pm 10\,\mathrm{km/s} \Longleftrightarrow <v> = -187\,\mathrm{km/s}, \tag{28}$$

and he determined the velocity ellipsoid to be

$$\sigma_u = 131 \pm 6\,\mathrm{km/s} \tag{29}$$
$$\sigma_v = 106 \pm 6\,\mathrm{km/s} \tag{30}$$

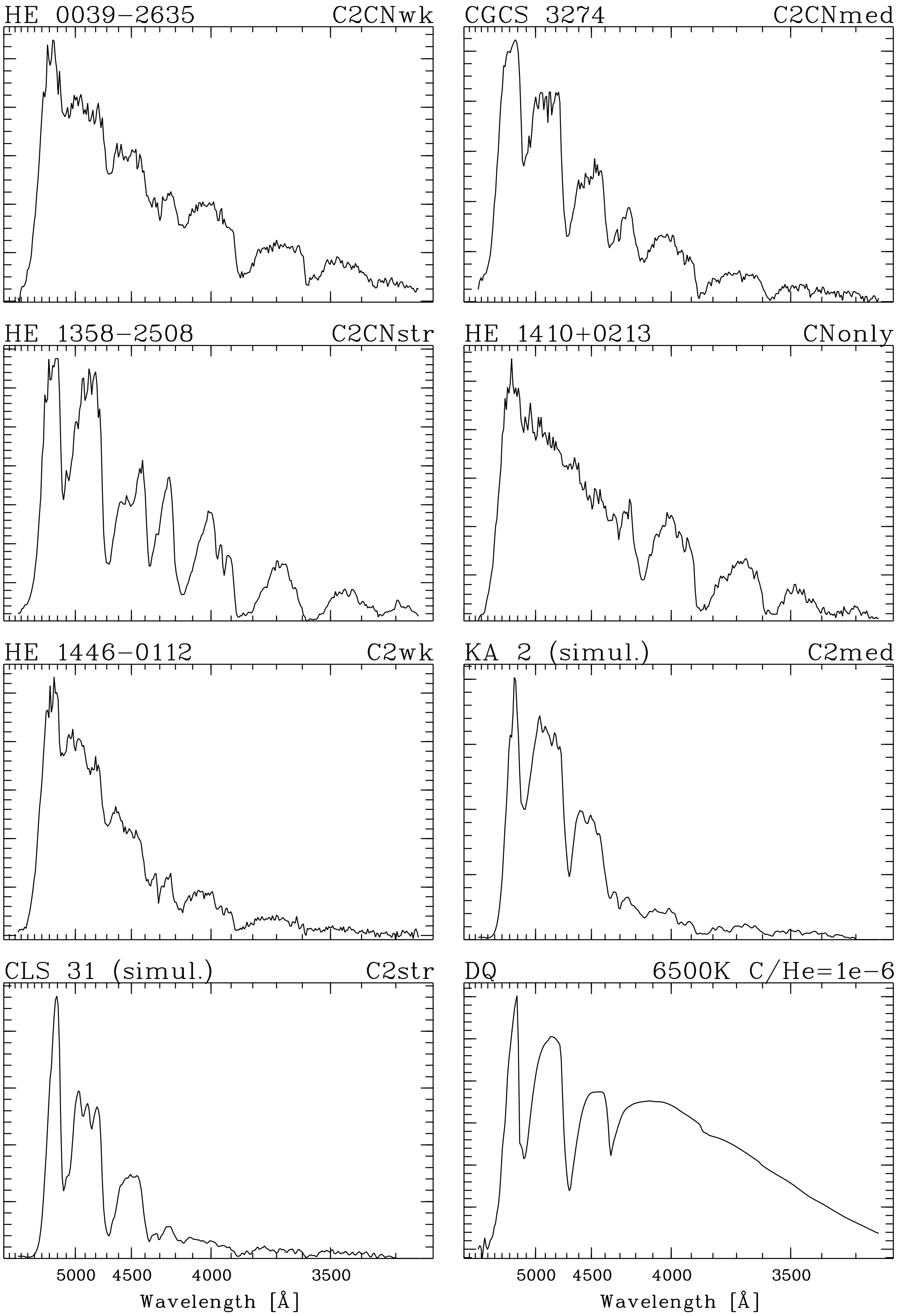

Figure 37: Objective prism spectra of seven C stars used as templates. The spectra of KA 2 and CLS 31 have been derived from slit spectra using the procedures described in Sect. 3.1 on p. 17ff. For comparison, the spectrum of a DQ white dwarf with $T_{\rm eff} = 6500\,$K and $\mathrm{C/He} = 10^{-6}$ is shown in the lower right panel. That star has $U - B = -0.6$.

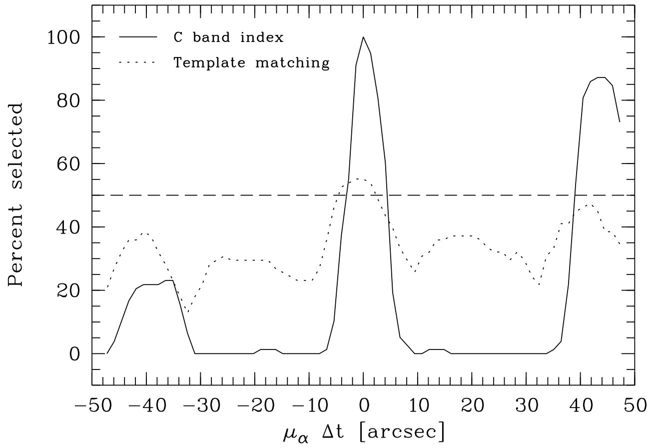

Figure 38: C star selection function in dependence of simulated proper motion $\mu_\alpha \cdot \Delta t$, for template C band index method (solid line), and template matching (dotted line). Selection by template matching has a higher effectivity in the ranges $-30'' \lesssim \mu_\alpha \Delta t \lesssim -2''$ and $5'' \lesssim \mu_\alpha \Delta t \lesssim 40''$.

$$\sigma_w \quad = \quad 85 \pm 6\,\mathrm{km/s}. \tag{31}$$

In each simulation we constructed 100 random velocity vectors (u, v, w), with components following Gaussian distributions according to the above parameters, i.e.

$$\begin{pmatrix} u \\ v \\ w \end{pmatrix} = \begin{pmatrix} N(\quad 0\,\mathrm{km/s}, 131\,\mathrm{km/s}) \\ N(-187\,\mathrm{km/s}, 106\,\mathrm{km/s}) \\ N(\quad 0\,\mathrm{km/s},\ 85\,\mathrm{km/s}) \end{pmatrix}. \tag{32}$$

$N(\mu, \sigma)$ denotes a Gaussian distribution with parameters μ, σ. These velocity vectors were each applied to stars placed at distances d computed from the apparent V magnitude distribution of a sample of 86 HES C stars without significant p.m. (see Fig. 31), and assuming $M_V = +10$ for dwarf carbon stars. This yields $86 \cdot 100 = 8\,600$ simulated stars.

We now define a coordinate system which is aligned with (u, v, w), i.e., x points away from the Galactic center, y into the direction of Galactic rotation, and z perpendicular to the Galactic plane. The vector $\vec{r}$ pointing from the Sun to a star with galactic coordinates l, b, at distance d is then:

$$\vec{r} = \begin{pmatrix} x \\ y \\ z \end{pmatrix} = d \cdot \begin{pmatrix} -\sin b \\ \cos b \sin l \\ \sin b \end{pmatrix}. \tag{33}$$

After the time Δt, the star with velocity vector (u, v, w) can be found at position $\vec{r}'$, which is

$$\vec{r}' = \begin{pmatrix} x' \\ y' \\ z' \end{pmatrix} = d \cdot \begin{pmatrix} -\sin b \\ \cos b \sin l \\ \sin b \end{pmatrix} + \Delta t \cdot \begin{pmatrix} u \\ v \\ w \end{pmatrix}. \tag{34}$$

Using the inverse transformations

$$d' \quad = \quad \sqrt{(x')^2 + (y')^2 + (z')^2} \tag{35}$$

$$b' \quad = \quad \arcsin \frac{z'}{d'} \tag{36}$$

$$l' \quad = \quad \arcsin \frac{y'}{d' \cos b'}, \tag{37}$$

we can compute the galactic coordinates l', b' of the star after the time Δt. Converting l, b and l', b' into α, δ and α', δ' then yields proper motions μ_α, μ_δ for each of the 8 600 simulated stars. As starting coordinates l, b we take the plate centers of each HES plates, and for Δt the epoch difference between DSS I and HES plate, $\Delta t_{\text{HES-DSS I}}$.

Finally, we select the subsample of the 8 600 stars with $\mu_\alpha \cdot \Delta t_{\text{HES-DSS I}} < 4''$, and determine, by multiplication with the selection probability in dependence of $\mu_\delta \Delta t$, the fraction of stars which would be detected in the HES *and* selected by either of the two carbon star selection methods. The result is shown in Fig. 39, and summarized in Tab. 11.

	Tmatch	C bands
Selection rate	36.1 %	21.4 %
Dwarf proof rate	96.5 %	61.5 %

Table 11: Average halo dC selection rates relative to zero p.m., and fraction of provable dwarfs for 329 HES plates.

Another number of interest is the rate of halo dCs which we can *proof* to be dwarfs from their p.m (we shortly call this rate *dwarf proof rate*, d.p.r). We can proof a star to have a luminosity $M_V > M_{V,\max}$, if its transverse velocity v_{trans} would be larger than the Galactic escape velocity v_{esc} otherwise, i.e. if

$$\text{p.m.} > \frac{v_{\text{trans}}}{4.74 \cdot 10\,\text{pc}} \cdot 10^{-\frac{m_V - M_{V,\max}}{5}}. \tag{38}$$

For dCs we use $M_{V,\max} = 8$, and we assume $v_{\text{esc}} = 400\,\text{km/s}$. As can be seen in Fig. 39, the d.p.r. is of course much higher for C stars selected by template matching, because with this method stars of higher p.m. can be selected.

Note that for halo dCs in the HES, there is no problem of p.m. *detection* for dCs that can be proven to be dwarfs by their transverse velocity, since it follows from Eq. 38 and the criteria described above that a $V = 16.5$ star must have a p.m. $> 0.17''/\text{yr}$ to be proven to be a dwarf. In Sect. 5.5 we will show that the typical 3σ uncertainty of the p.m. measurement method we employed is $\sim 0.012''/\text{yr}$ for baselines of ~ 45 yrs. So even if only archival images with a 10 years epoch difference were available for comparison with our CCD images, resulting in a 3σ uncertainty of $\sim 0.054''/\text{yr}$, we could easily detect proper motions $> 0.17''/\text{yr}$.

From the results shown in Tab. 11 and Fig. 38 we can derive correction factors c for the dwarf fractions (in %) we detect in our samples. We define:

$$c = \frac{\text{frac}_{\text{real}}}{\text{frac}_{\text{measured}}}.$$

Let N_D/N_G be the real ratio of dwarfs to giants, and f_D, f_G the detection fraction of dwarfs and giants, respectively. Then it can be easily computed that

$$c = \frac{\frac{N_D}{N_G} + \frac{f_G}{f_D}}{\frac{N_D}{N_G} + 1}. \tag{39}$$

According to Green et al. (1992),

$$\frac{N_D}{N_G} = \frac{0.13}{0.87} = 0.15.$$

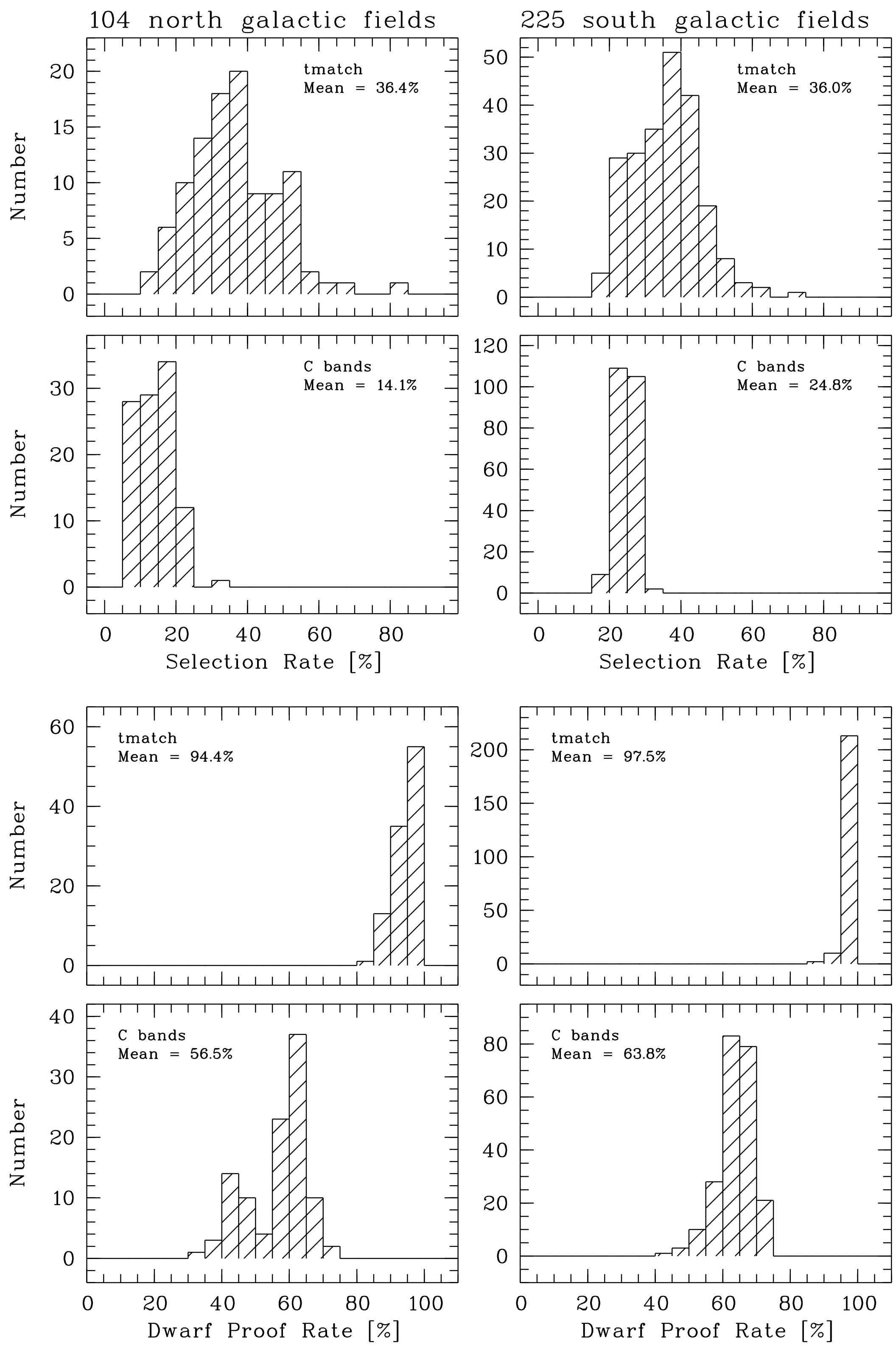

Figure 39: Distribution of plate-wise relative selection probabilities of halo dCs for 329 HES plates.

For the C band index method, we have

$$\frac{f_{G,\mathrm{C\ band}}}{f_{D,\mathrm{C\ band}}} = \frac{1.00}{0.214 \cdot 0.615} = 7.60,$$

and for template matching

$$\frac{f_{G,\mathrm{tmatch}}}{f_{D,\mathrm{tmatch}}} = \frac{0.50}{0.361 \cdot 0.965} = 1.44,$$

so that we obtain

$$c_{\mathrm{C\ band}} = 6.7, \tag{40}$$

and

$$c_{\mathrm{tmatch}} = 1.4. \tag{41}$$

That is, within the C band index selected sample, the dwarf fraction will be 6.7 times lower than it really is, and in the template matching selected sample 1.4 times lower.

Even more interestingly, we will be able to derive the local space density for halo dCs, $N_{\mathrm{dC}}^{\mathrm{halo}}$, by applying the correction factors $f_{D,\mathrm{C\ band}}$, $f_{D,\mathrm{tmatch}}$ to our flux-limited sample of dCs.

5.3.3 Tests with Known C Stars

We also compiled a test sample of known dwarf and giant C stars present on HES plates (see Tab. 12). We took all three dCs in the southern hemisphere listed by Deutsch (1994), i.e. LHS 1075, G77-61, and KA 2. The (possible) dCs of (Warren et al. 1993), having $B_J > 20$, unfortunately are by far too faint to be detectable on HES plates. Cross-identification with the C star lists of Slettebak et al. (1969), Stephenson (1989), Bothun et al. (1991), and Totten & Irwin (1998), yielded 22 stars. Another 6 spectra were produced from slit spectra with the procedures described in Sect. 3.1.

In our test, *all* 22 stars not known as dwarfs have been selected either by their strong C_2 bands, or their CN bands, with the band index method. The simulated spectra were also *all* selected either by C_2 band indices, or CN indices. For these spectra it was not possible to carry out template matching, because they are noise-free. 13 of the 14 remaining stars below saturation threshold and not known as dwarfs have been selected by template matching. This fraction is much higher than expected from our simulations (50 %). This is probably due to the fact that our test sample is biased towards red objects, with *strong* C bands, so that they are easier to select than the stars in our test sample. Of the three dCs, one (KA 2) has been selected by all methods, one (G77-61) by template matching only, and one (LHS 1075) by neither method.

From these results we conclude that our sample of giant C stars and dwarfs with low p.m. (e.g. dCs belonging to the disk population) is highly complete. From the small number of dCs in our test sample we are not able to draw any definitive conclusions, but our result is consistent with our simulations. Using Poisson statistics, we derive from our test sample that our dC detection rate is 66 ± 33 %.

5.3.4 Selection Efficiency

Another important criterion for the evaluation of the quality of a selection algorithm is the *selection efficiency*, i.e. the fraction of desired stars in the raw candidate sample. Tab. 13 summarizes the results for both selection methods used.

The C band index method has a much higher selection efficiency than the template matching method. This is because with the latter, a lot of artifacts and noisy spectra are selected. The low fraction of artifacts in the sample selected with the C band method demonstrates that the usage of *pairs*

Name	HE Name	B_J	$B-V$	$\mu_\alpha \Delta t$	$\mu_\delta \Delta t$	Selected by				Source
						C_2	CN	T	All	
CGCS 39	HE 0017+0055		1.4			1	1	–	1	S89
SKB 2	HE 0039−2635	13.1	1.1			1	1	–	1	SKB69
BEM91 23	HE 0100−1619	15.9	1.5			1	0	1	1	BEM91
CGCS 177	HE 0106−2837	13.8	2.1			1	0	1	1	S89
SKB 5	HE 0111−1346	13.3	1.4			1	1	–	1	SKB69
0207-0211	HE 0207−0211	15.5	2.2	0.0	0.0	1	0	1	1	TI98
BEM91 08	HE 0228−0256	16.2	2.0			1	0	1	1	BEM91
CGCS 525	HE 0330−2815	13.8	1.5			0	1	0	1	S89
CGCS 935	HE 0521−3425	13.0	1.3			1	1	–	1	S89
0915-0327	HE 0915−0327	14.5	2.3	0.0	0.0	1	0	1	1	TI98
1019-1136	HE 1019−1136	15.2	1.8	0.0	0.0	1	0	1	1	TI98
CGCS 2954	HE 1104−0957		1.2			1	1	–	1	S89
KA 2	HE 1116−1628	16.6	1.3			1	0	1	1	R83
CGCS 3180	HE 1207−3156	12.8	1.2			0	1	–	1	S89
CGCS 3274	HE 1238−0836		1.7			1	1	–	1	S89
1254-1130	HE 1254−1130	16.1	2.2	0.0	0.0	1	0	1	1	TI98
1339-0700	HE 1339−0700	15.0	1.7	0.0	0.0	1	0	1	1	TI98
1442-0058	HE 1442−0058	17.8	2.2	0.0	0.0	1	0	1	1	TI98
CGCS 5435	HE 2144−1832	12.6	1.4			0	1	–	1	S89
CGCS 5549	HE 2200−1652	12.3	0.9			1	1	–	1	S89
2213-0017	HE 2213−0017	16.4	2.4	0.0	0.0	1	0	1	1	TI98
2225-1401	HE 2225−1401	16.5	2.9	0.0	0.0	1	0	1	1	TI98
CLS 50				0.0	0.0	1	0	–	1	Simul.
CLS 31				0.0	0.0	1	1	–	1	Simul.
CLS 54				0.0	0.0	1	1	–	1	Simul.
KA 2				0.0	0.0	1	1	–	1	Simul.
B1509-0902				0.0	0.0	1	1	–	1	Simul.
UM 515				0.0	0.0	1	0	–	1	Simul.
LHS 1075	HE 0023−1935	16.1	1.4	$-0.''24$	$-10.''0$	0	0	0	0	D94
KA 2	HE 1116−1628	16.6	1.3	$-0.''21$	$0.''24$	1	0	1	1	D94
G77-61	HE 0330+0148	15.0	1.4	$1.''9$	$-7.''5$	0	0	1	1	D94

Table 12: Test sample of dwarf and giant C stars present on HES plates. Sources: BEM91=Bothun et al. (1991), D94=Deutsch (1994), R83=Ratnatunga (1983), S89=Stephenson (1989), SKB69=Slettebak et al. (1969), TI98=Totten & Irwin (1998). Stars marked with TI98 have been recently reported by Totten et al. (2000) to have no significant p.m. Therefore, we list them with $(\mu_\alpha \Delta t, \mu_\delta \Delta t) = (0,0)$. For some of these stars, we independently obtained a p.m. measurement, too (see Appendix B). Our results agree with those of Totten et al. (2000). Template matching is not carried out for HES spectra above the saturation threshold, because we do not have an estimation of pixel-wise noise for these. KA 2 has not been selected by CN bands, using its real spectrum, but it *has* been selected in the course of our simulations. This is because the S/N at the position of the CN bands is too low in the former spectrum, and effectively infinite in the simulated spectrum.

	C bands	Tmatch
Raw candidate reduction factor	1/2900	1/800
C stars	31.6 %	2.4 %
UNID	7.0 %	1.5 %
OVL	29.2 %	6.6 %
ART	8.7 %	32.0 %
NOIS	3.8 %	54.8 %
SAT	15.6 %	0.0 %

Table 13: Selection efficiency for C stars in the HES, for both selection methods used. UNID=*probable* C stars with weak C bands, OVL=overlapping spectra, ART=artifacts, NOIS=very noisy spectra, SAT=saturated spectra. The raw candidate reduction factor is the factor by which the selection algorithms reduce the *total* set of HES spectra. For example, the C band index method extracts 1 199 candidates from 3 437 630 spectra present on 329 HES plates.

of C_2 bands and CN bands indeed very reliably excludes artifacts from selection. On the other hand, with this method more overlapping spectra are selected, because the band indices can be easily confused by them. The fraction of saturated spectra is zero for the template matching method, because sources above the saturation threshold are excluded from template matching. This is because the template matching method needs an estimate of the pixel-wise noise, and our noise estimation is not valid for saturated spectra.

5.4 The Surface Density of C Stars

In an effective area of $\sim 6400\,\mathrm{deg}^2$ (329 of 380 the HES plates), we have isolated a total of 351 C stars, selected by either the C band index or the template matching method. In 225 fields, located at $20^h30 <$R.A.$< 06^h30$ (“south Galactic fields”), we find 0.037 FHLC stars deg^{-2}. This is almost twice what has been reported by Green et al. (1994) from their own CCD survey and the sum of FHLC stars selected from photographic objective prism surveys then available. Moreover, the CCD survey limit of Green et al. (1994) was $V = 18$, which is also a typical brightness limit for the relevant objective prism surveys, whereas the HES survey limit is $V \simeq 16.5$ (see Fig. 31). Interestingly, the surface density of FHLC stars in 104 fields located at $09^h00 <$R.A.$< 15^h20$ (“north Galactic fields”) is almost a factor 3 higher than in the south Galactic fields: In the former we find 0.099 FHLC stars deg^{-2}.

5.5 Astrometry

To measure the p.m.s of our carbon stars, we obtained V images for 92 FHLC stars at the European Southern Observatory, La Silla, Chile on April 26–28, 1999, using the Wide Field Imager attached to the ESO/MPI 2.2 m telescope.

We compared the CCD positions of our carbon stars with positions from archival plate material. The USNO-A2.0 catalog (Monet et al. 1998), derived from re-scanned Palomar Observatory Sky Survey I (POSS I) plates, provides the earliest epochs; typically in the 1950s. However, POSS I plates are only available at $\delta > -25°$. Additionally, we extracted DSS I and DSS II image data from the ST ScI data archive. When available, the original POSS I images were also retrieved.

Subimages of $8' \times 8'$ size with our targets in the center were extracted from our CCD frames. In these images, we selected 20–60 sufficiently bright, isolated reference stars by hand. These were then used for alignment of the reference coordinate system (provided by the archival data) with the target image. For most of our images it was possible to do carry out three alignments: (1) DSS I/POSS I image to the CCD image, (2) USNO-A2.0 catalog to the DSS II image, and (3) USNO-A2.0 catalog to the CCD image. Since the USNO-A2.0 catalog was generated from POSS I plates, neither of the alignment pairs is independent of the others.

After rejection of reference objects with significant p.m. or measurement errors, the alignment usually employs 15–50 stars, depending on the field density, and deepness of the exposure obtained. The transferred solution is a simple linear solution (sufficient for the small fields used for this purpose) derived with a least-squares fit using procedures from the IDL *Astronomy User's Library* (Landsman 1993) and written in IDL by E.W. Deutsch (University of Washington). The uncertainty in the transfer is typically $\sim 0\farcs05$. The shift in position of the target star is recorded for each of the three comparisons described above, along with a 1σ uncertainty estimated from the residuals of the fit. We report here only the results from the transfer of the USNO-A2.0 catalog positions to the CCD images, but the other solutions are examined to verify these results.

Candidates have been selected to have a significant p.m. measurement if (a) their p.m. is higher than $3\times$ the 1σ uncertainty estimate from the USNO-A2.0 to CCD comparison, (b) the results from the other comparisons are consistent, and (c) no nearby companions are present which might cause significant centroiding errors. Tab. 14 shows coordinates of the 5 stars out of our sample of 92 for which we measure a significant p.m. Astrometry results for these stars are given in Tab. 15. Stars without significant p.m. are listed in Tab. 25 and 26, in Appendix B.

#	Name	α (2000.0)	δ (2000.0)	Epoch
1	HE 0930−0018	09 33 24.7	−00 31 46	1983.4
2	HE 0945−0813	09 48 18.7	−08 27 40	1983.4
3	HE 1428−1950	14 30 59.4	−20 03 42	1976.5
4	HE 1429−0551	14 32 31.3	−06 05 00	1983.3
5	HE 1524−0210	15 26 56.9	−02 20 45	1979.5

Table 14: Coordinates of 5 HES carbon stars with significant p.m.

In addition to our targets, we carried out a new proper motion measurement for KA 2 (Ratnatunga 1983; Green et al. 1992; Deutsch 1994), which was rediscovered in our survey. A comparison of our result with previous measurements is given in Tab. 16. Our values are in good agreement with those of Ratnatunga (1983) and Deutsch (1994). Green et al. (1992) reported a marginal detection of a p.m. for this object in the same order of magnitude as that of Ratnatunga (1983), but with opposite sign in μ_α, which disagrees with our result.

From our p.m. measurements, Eq. (38), and photometry presented in Tab. 17 we conclude that one star (HE 0930−0018) out of the 5 new HES carbon stars for which we measure a significant p.m. is likely to be a dwarf, and another (HE 0945−0813) is possibly a subgiant.

5.6 Discussion and Conclusions

In an effective area of $\sim 6400\,\mathrm{deg}^2$ (329 of 380 the HES plates), we have isolated a total of 351 C stars. Our efforts have thus already increased the number of known FHLC stars by a factor of nearly five.

#	Name	μ_α σ_{μ_α}	μ_δ σ_{μ_δ}	μ σ_μ	Baseline
1	HE 0930-0018	−0.051 0.005	0.034 0.004	0.061 0.005	1955.0–1999.3
2	HE 0945-0813	0.004 0.004	0.012 0.004	0.013 0.004	1953.0–1999.3
3	HE 1428-1950	0.014 0.003	0.006 0.003	0.015 0.003	1953.0–1999.3
4	HE 1429-0551	−0.005 0.003	−0.014 0.003	0.015 0.003	1954.4–1999.3
5	HE 1524-0210	0.003 0.004	−0.012 0.003	0.012 0.003	1953.0–1999.3

Table 15: Proper motions for 5 HES carbon stars with significant p.m. For each object we list in the first row the proper motion in arcseconds per year, and in the second row 1σ errors.

Reference	μ_α	μ_δ	σ_{μ_α}	σ_{μ_δ}
This work	−0.020	0.027	0.003	0.004
Deutsch (1994)	−0.026	0.031	0.003	0.003
Ratnatunga (1983)	−0.026	0.024	0.003	0.003

Table 16: Comparison of astrometry results for KA 2. Proper motions and errors are given in arcseconds per year.

#	Name	B_J	$(B-V)^*_{\rm HES}$	$(B-V)_{\rm CCD}$	$B^{**}_{\rm HES}$	$B_{\rm CCD}$	$V_{\rm HES}$	$V_{\rm CCD}$
1	HE 0930-0018	15.7	1.4	–	16.1	–	**14.7**	–
2	HE 0945-0813	16.2	1.2	–	16.5	–	**15.3**	–
3	HE 1428-1950	12.8	1.2	1.15	13.1	13.15	11.9	**12.00**
4	HE 1429-0551	13.4	1.4	1.28	13.8	13.94	12.4	**12.67**
5	HE 1524-0210	14.5	1.5	1.56	14.9	15.70	13.4	**14.14**
	KA 2	16.6	1.3	–	16.9	–	**15.6**	–

* From calibration of `dx_hpp2` (see Tab. 6).

** Following Hewett et al. (1995), we use $B = B_J + 0.28 \cdot (B-V)$.

Table 17: Photometry for the 5 carbon stars with significant p.m. B_J is measured on HES plates and is accurate to ± 0.2 mag. Adopted V magnitudes are written in bold.

#	Name	μ^*	$M_{V,\min}^{**}$	Dwarf ($M_V = 10$)			Giant ($M_V = -1$)	
				d	π	$v_{\rm trans}^{***}$	d	$v_{\rm trans}^{***}$
1	HE 0930-0018	0.″061	4.0	87 pc	0.″011	25 km/s	14 000 pc	4 000 km/s
2	HE 0945-0813	0.″013	1.2	110 pc	0.″0091	6.8 km/s	18 000 pc	1 100 km/s
3	HE 1428-1950	0.″014	−2.0	25 pc	0.″040	1.7 km/s	4 000 pc	260 km/s
4	HE 1429-0551	0.″015	−1.4	35 pc	0.″029	2.5 km/s	5 400 pc	390 km/s
5	HE 1524-0210	0.″013	−0.7	66 pc	0.″015	4.1 km/s	11 000 pc	660 km/s
	KA 2	0.″033	8.6	130 pc	0.″0076	21 km/s	21 000 pc	3 300 km/s

* $\mu = \sqrt{\mu_\alpha^2 \cos^2\delta + \mu_\delta^2}$.

** Assuming $v_{\rm trans} < 400$ km/s (∼ Galactic escape velocity).

*** $v_{\rm trans}\,[\mathrm{km/s}] = 4.74 \cdot \mu\,[''/\mathrm{yr}] \cdot d[\mathrm{pc}]$.

Table 18: Distances and transverse velocities for 5 HES carbon stars with significant p.m., for the assumptions that they are dwarfs or giants.

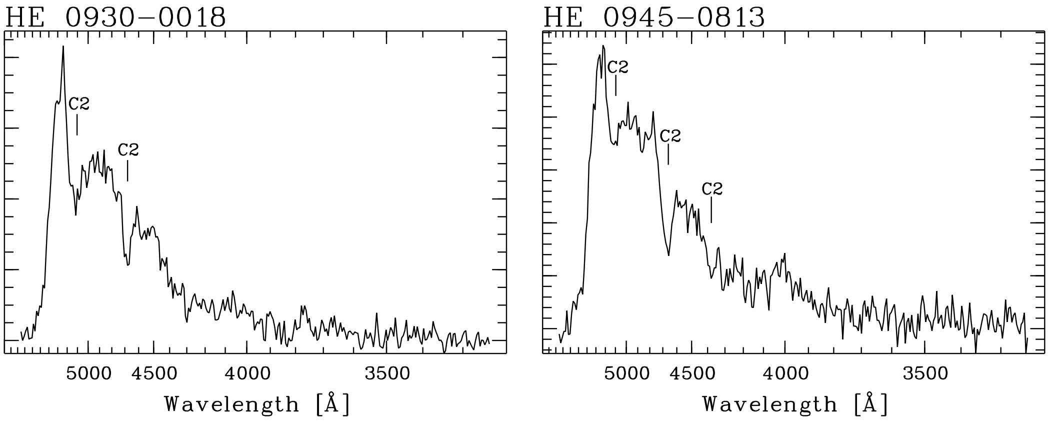

Figure 40: Objective prism spectra of the carbon stars HE 0930−0018 and HE 0945−0813, discovered in the HES. According to our proper motion measurement, HE 0930−0018 is likely to be a dwarf, and HE 0945−0813 is possibly a subgiant. Abscissae are densities in arbitrary units.

The surface density of FHLC stars found in the HES indicates that previous surveys suffer from severe incompleteness. For instance, at a survey limit $\sim 1.5^m$ *brighter* than the CCD survey of Green et al. (1992), we find a factor of ∼ 2 higher surface density of FHLC stars in 225 southern galactic latitude fields (0.037 deg^{-2}), and a factor of ∼ 5 higher surface density in 104 northern Galactic fields (0.099 deg^{-2}). This corresponds to ∼ 16× and ∼ 40× higher space densities of C stars, respectively. The south Galactic fields are located at higher galactic latitude on average ($|b| = 60^\circ$ compared to $|b| = 45^\circ$), but the mean plate limits of the corresponding HES plates do not differ significantly, so that a scale height effect might be present.

Our results indicate that previous FHLC selection procedures have been less sensitive to the strength or variety of C_2 or CN molecular bands. Automatic selection techniques may be superior to visible inspection of objective-prism spectra with binocular microscopes, as done e.g. in the survey of Sanduleak & Pesch (1988). Photometric surveys for C stars have generally selected red objects only, which preferentially selects mostly the much less common high latitude AGB stars.

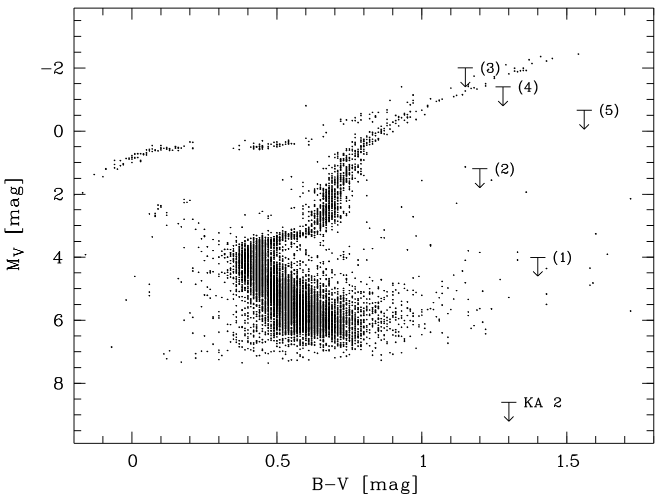

Figure 41: Upper limits for M_V of 5 HES carbon stars with significant p.m., and KA 2, for orientation shown together with the HR diagram of the old (18.7 Gyr), metal-poor ([Fe/H] = −1.66) globular cluster M 3 = NGC 5272 (Buonanno et al. 1994). M_V has been computed from the data of Buonanno et al. (1994) by assuming $m_v - M_V = 15.10$ (Reid 1999).

Due to an average epoch difference of 13.5 years between DSS I and HES plates, we expect to detect and select only $\sim 40\,\%$ of the dCs that we could detect and select if direct plates had been taken simultaneously with the HES plates. However, our extensive simulations yielded correction factors for the dwarf fraction in our sample (Eqs. 40 and 41).

Our corrected dwarf fractions predict $92 \cdot 0.13/6.7 = 1.8$ provable dwarfs to be present in our sample of 92 FHLC stars observed in April '99 with the ESO 2.2 m. This is consistent with the one *provable* dwarf we found, when applying the criterion $M_V > 8$ and assuming $v_{\rm esc} = 400$ km/s. This dC is the previously known star KA 2.

Using again the dwarf fraction obtained by Green et al. (1992), we can estimate how many provable dCs we expect to find in the HES. We selected a total of 347 C stars with the C band index method. Assuming a selection efficiency for giants of 100 % and using the numbers in Tab. 11, we derive that this sample should consist of 336 giants and 11 dwarfs, of which we can proof 7 to be dwarfs by their p.m. On this basis we predict that another 39 dwarfs should be out there in space which we miss by the C band index method. Of the total of 50 dwarfs, we can select 18 by template matching, according to our simulations, and 17 of them we can proof to be dwarfs. Half of the dCs found with the C band index method are expected to be found by template matching as well, so that we predict to find a total of $17 + 7 \cdot 0.5 \simeq 21$ provable dwarfs. This would *triple* the sample of known dCs.

5.7 Outlook

With HE 0930−0018 we found a star which is likely to be a new dwarf. If any of the remaining four C stars for which we measure a significant p.m. is a dwarf, it would have a parallax which is measurable from ground-based observatories (see Tab. 18). Therefore, and to get a definitive answer for HE 0930−0018, we are seeking all 5 stars to be observed in a long-term parallax program. Alternatively, parallaxes could be easily measured by the upcoming new generation of astrometry satellites, like FAME and SIM.

HE 0930−0018 is also scheduled to be observed at high resolution in the commissioning phase of the High Dispersion Spectrograph (HDS) at the Subaru telescope for an abundance analysis, and to derive stellar parameters spectroscopically.

CCD images of another 109 C stars and 10 control objects have been obtained with the ESO 2.2 m telescope in November 1999. These are currently being analyzed. 8 hours of observing time in period 65 (April–October 2000) has been granted to our project by ESO, so that another ~ 80 targets will soon be observed.

We plan to obtain JHK photometry for all new dCs we discover in the HES, and also for as many stars without p.m. as possible. Should dCs be confirmed to be distinguishable from giants by JHK colors (as suggested by the results of Green et al. 1992), we would be able to construct a luminosity criterion. This is very important for all kinematic studies using carbon stars, since a contamination by a significant number of dwarfs (*at least* 13 % according to Green et al. 1992) would bias the results considerably. Moreover, being able to identify all giants means that we are also able to identify all *disk* dCs in our sample, which are less easily found by means of p.m. This would allow us to estimate the local space density of disk dCs, $N_{\rm dC}^{\rm disk}$, and test the model for the space density of dCs suggested by de Kool & Green (1995). Their model predicts a strong metallicity dependence of the fraction of binaries in which the secondary becomes a dC. Taking the ~ 500 times higher local space density of disk stars into account (Bahcall & Soneira 1984), de Kool & Green (1995) predict that $N_{\rm dC}^{\rm disk}$ is 2.5–5 times higher than $N_{\rm dC}^{\rm halo}$.

Acknowledgements

I thank my fellow "dwarf hunters", P. Green and E. Deutsch, for a very productive and joyful collaboration, and many discussions. From Paul I learned much about the scientific background of current C star research. He also provided me with a list of known C stars, and with slit spectra for some of them. Eric provided his neat IDL programs, and processed *more* than half of our 92 CCD images with them when we were visiting Paul at the Harvard-Smithsonian Center for Astrophysics (CfA), because he is much faster at it than I am!

Paragraphs 3–5 of Sect. 5.5 have been originally written by Eric for an article which is in preparation; I just added a few further explanations and remarks. The same holds for paragraphs 3–5 of the introduction, which have been written by Paul.

I acknowledge the hospitality shown to me at CfA, where part of the work described in this section was carried out.

References

Bahcall, J. N. & Soneira, R. M. (1984), 'Comparisons of a standard galaxy model with stellar observations in five fields', *ApJS* **55**, 67–99.

Bothun, G., Elias, J. H., MacAlpine, G., Matthews, K., Mould, J. R., Neugebauer, G. & Reid, I. N. (1991), 'Carbon stars at high Galactic latitude', *AJ* **101**, 2220–2228.

Brewer, J. P., Richer, H. B. & Crabtree, D. R. (1996), 'Late-type stars in M31. II. C-, S-, and M-star spectra', *AJ* **112**, 491–508.

Buonanno, R., Corsi, C. E., Buzzoni, A., Cacciari, C., Ferraro, F. R. & Pecci, F. F. (1994), 'The stellar population of the globular cluster M 3. I. Photographic photometry of 10 000 stars', *A&A* **290**, 64.

Castleman, K. R. (1979), *Digital Image Processing*, Prentice Hall, Englewood Cliffs.

Christlieb, N. (1995), Automatische Klassifikation von digitalisierten Objektivprismen-Platten, Diplomarbeit, Universität Hamburg.

Dahn, C. C., Liebert, J., Kron, R. G., Spinrad, H. & Hintzen, P. M. (1977), 'G77-61 – A dwarf carbon star', *ApJ* **216**, 757–766.

de Kool, M. & Green, P. J. (1995), 'A model for the space density of dwarf carbon stars', *ApJ* **449**, 236–245.

Dearborn, D. S. P., Liebert, J., Aaronson, M., Dahn, C. C., Harrington, R., Mould, J. & Greenstein, J. L. (1986), 'On the nature of the dwarf carbon star G77-61', *ApJ* **300**, 314–324.

Deutsch, E. W. (1994), 'Positions and Proper Motions of Dwarf Carbon Stars', *PASP* **106**, 1134–1137.

Green, P. J. & Margon, B. (1994), 'Constraints on the origin of dwarf carbon stars', *ApJ* **423**, 723–732.

Green, P. J., Margon, B. & Anderson, S. F. (1992), 'Carbon star luminosity indicators', *ApJ* **400**, 659–664.

Green, P. J., Margon, B. & MacConnell, D. J. (1991), 'Three newly recognized dwarf carbon stars', *ApJ* **380**, L31–L34.

Green, P. J., Margon, B., Anderson, S. F. & Cook, K. H. (1994), 'A CCD survey for faint high-latitude carbon stars', *ApJ* **434**, 319–329.

Heber, U., Bade, N., Jordan, S. & Voges, W. (1993), 'PG 0824+289: a dwarf carbon star with a visible white dwarf companion', *A&A* **267**, L31–L34.

Hewett, P. C., Foltz, C. B. & Chaffee, F. H. (1995), 'The Large, Bright QSO Survey. VI. Quasar Catalog and survey parameters', *AJ* **109**, 1498–1521.

Landsman, W. B. (1993), The IDL Astronomy User's Library, *in* R. J. Hanisch, R. J. V. Bissenden & J. Barnes, eds, 'ADASS II', Vol. 52 of *ASP Conf. Ser.*, pp. 246–248.

Liebert, J., Schmidt, G. D., Lesser, M., Stepanian, J. A., Lipovetsky, V. A., Chaffe, F. H., Foltz, C. B. & Bergeron, P. (1994), 'Discovery of a dwarf carbon star with a white dwarf companion and of a highly magnetic degenerate star', *ApJ* **421**, 733–737.

MacAlpine, G. M. & Lewis, D. W. (1978), 'Curtis Schmidt-thin prism survey for extragalactic emission-line objects. University of Michigan List IV.', *ApJS* **36**, 587–593.

Margon, B., Anderson, S. F., Deutsch, E. W. & Harris, H. C. (1999), Faint Carbon Stars Discovered by the Sloan Digital Sky Survey, *in* 'AAS Meeting 195', p. #80.06.

McCook, G. P. & Sion, E. M. (1999), 'A catalog of spectroscopically identified white dwarfs', *ApJS* **121**, 1–130.

Monet, D. G., Bird, A. & Canzian, B. (1998), USNO-A2.0: A catalog of astrometric standards, Technical report, U.S. Naval Observatory.

Morrison, H. L., Mateo, M., Olszewski, E. W., Harding, P., Dohm-Palmer, R. C., Freeman, K. C., Norris, J. E. & Morita, M. (2000), 'Mapping the Galactic Halo I. The "Spaghetti" Survey', *ApJ* **?**, ? in press (astro-ph/0001492).

Mould, J. R., Schneider, D. P., Gordon, G. A., Aaronson, M. & Liebert, J. W. (1985), 'The velocity dispersion of carbon stars at the north Galactic pole', *PASP* **97**, 130–137.

Norris, J. (1986), 'Population studies. II – Kinematics as a function of abundance and galactocentric position for [Fe/H]≤ -0.6', *ApJS* **61**, 667–698.

Ratnatunga, K. U. (1983), Outer regions of the Galactic halo, PhD thesis, Australian National University, Canberra.

Reid, I. N. (1999), 'The HR Diagram and the Galactic Distance Scale After Hipparcos', *ARAA* **37**, 191–237.

Sanduleak, N. & Pesch, P. (1988), 'The Case low-dispersion northern sky survey. VII. Late-type stars', *ApJS* **66**, 387–390.

Slettebak, A., Keenan, P. C. & Brundage, R. K. (1969), 'Carbon stars in a south galactic pole region', *AJ* **74**, 373–374.

Stephenson, C. B. (1989), 'A General Catalog of Cool Galactic Carbon Stars, 2nd Edition', *Publ. W.&S. Obs*.

Totten, E. J. & Irwin, M. J. (1998), 'The APM survey for cool carbon stars in the Galactic halo. I', *MNRAS* **294**, 1–27.

Totten, E. J., Irwin, M. J. & Whitelock, P. A. (2000), 'The APM survey for cool carbon stars in the Galactic halo. II. The search for dwarf carbon stars', *MNRAS* **000**, 000–000. in press (astro-ph/0001113).

Warren, S. J., Irwin, M. J., Evans, D. W., Liebert, J. W., Osmer, P. S. & Hewett, P. C. (1993), 'More dwarf carbon stars', *MNRAS* **261**, 185–189.

6 Field Horizontal Branch A-Type Stars

Field horizontal branch A-Type stars (FHB/A) are valuable tracers for the kinematics of the halo of the Galaxy. In the HES, they can be found at distances of up to ~ 20 kpc. Compared to carbon stars, they have the advantage that they are much more numerous, with surface densities of $\sim 2.5\,deg^{-2}$ in the HES. In the HES, A-type stars can be selected even at very low S/N, since the Balmer lines are so prominent. Therefore, the faintest objects have $V \simeq 17.5$.

For FHB/A stars, there is no such complication as a contamination with spectroscopically indistinguishable dwarfs, like for the C stars. Main-sequence A-type stars *are* found at high galactic latitudes, but they can easily distinguished from low gravity stars by UBV photometry (Wilhelm et al. 1999*a*).

Another application of FHB/A stars is distance estimation of High Velocity Clouds (HVCs). These are clouds of neutral hydrogen at velocities incompatible with Galactic differential rotation (for a recent review see Wakker & van Woerden 1997). With HVCs, we might observe a continuous infall of metal-poor ($\sim 1/10$ solar) gas into the Galaxy, which dilutes the enrichment of the interstellar medium (ISM) by heavy elements produced in stars (Wakker et al. 1999). The understanding of the nature of HVCs would therefore be important for modeling the chemical evolution of the Galaxy. However, there is an ongoing discussion on whether HVCs are really Galactic objects (van Woerden et al. 1998), or if they are extragalactic remnants of gas that formed the local group of galaxies, which would put them in distances in the order of Mpc (Blitz et al. 1999).

Distances to HVCs can be determined by using stars of known distance in the line of sight to the clouds (Wakker & van Woerden 1997). Provided that the HVC under consideration has a detectable metal content, we see absorption lines of these metals at the velocity of the cloud in the spectra of stars located *behind* the cloud, but do not see these lines in spectra of stars located *in front of* the stars. By using a sample of stars of different distances in the line of sight of the cloud, we can bracket it, provided the cloud is Galactic, and the most distant star used in the procedure is far enough away. If so, a distance range can be determined for the cloud. FHB/A stars are particularly suited for these purpose, because they are numerous, distant, and their spectra are almost free of intrinsic absorption lines of metals.

Finally, FHB/As can be used for the detection of possible "clumping" of the Galactic halo, which would prove that merger events have taken place during the formation of our Galaxy. In a first attempt, Doinidis & Beers (1989) have carried out a two-point correlation function analysis of a catalog of 4 400 *candidate* FHB/A stars and found evidence for an excess of stellar pairs with angular separations $\leq 10'$. However, at that time it was not yet clear that samples of high latitude A-type stars contain a considerable fraction ($\sim 1/3$) of main-sequence A-type stars. The distances of these stars were hence overestimated, and the detection of clustering is possibly an artifact. In Sect. 6.4 we outline how the fraction of high-gravity A-type stars can be reduced in HES FHB/A candidate samples.

Yanny et al. (1999) report on the isolation of a first set of 2 000 objects with colours of A-type stars in the SDSS commissioning data. Since the SDSS magnitude limit is $V \simeq 20$, these stars can be rather distant $d \lesssim 40$ kpc, which makes them particularly valuable for studying the outer regions of the Galactic halo. However, the SDSS has just started to produce data, and spectroscopic analysis of a large sample of FHB/A stars from that survey will likely not be available within the next few years.

6.1 Candidate Selection

For selection of candidate FHB/A stars we use automatic spectral classification. A learning sample of 654 spectra (see Tab. 19) has been compiled by classifying HES spectra by hand. We used the spectra of Jacoby et al. (1984), converted to objective prism spectra, for comparison. Note that *rectified* spectra were used in the comparison process. To the learning sample we add artificial noise, resulting in 5 S/N steps (5, 10, 15, 20, 25). $S/N = 30$ was not achievable since some of the learning sample spectra have a lower S/N than that.

i	Class	N
1	A5–8	39
2	A9–F2	67
3	F3–6	130
4	F7–G0	119
5	G1–K0	134
6	K1–3	65
7	K4–9	67
8	SdFearly	33

Table 19: Learning sample for selection of FHB/A star candidates. The sample size is 654.

We carried out a search for the best feature combination for compiling a complete sample of FHB/A stars on a set of 14 features, using the above learning sample. A complete search was done, i.e. all $2^{14} - 1$ feature combinations were evaluated, using the leaving-one-out method. The result is shown in Tab. 20. With exception of the original learning sample, without artificial noise added, there is a tendency to use more features for classification at lower S/N, and to use more continuum shape or broad band colour features.

Feature	S/N					
	orig.	25	20	15	10	5
`all5160eqw`	1	0	0	1	1	1
`all4861eqw`	0	1	0	0	1	0
`all4388eqw`	1	0	0	0	1	0
`all4340eqw`	1	1	1	1	1	1
`all4300eqw`	1	0	1	0	1	1
`all4261eqw`	0	0	1	1	0	0
`all4227eqw`	1	0	1	1	0	0
`all4102eqw`	1	1	1	1	0	0
`all3969eqw`	1	0	0	0	1	0
`all3934eqw`	1	0	0	1	0	1
`klcomp_1`	1	0	0	0	0	1
`klcomp_2`	0	1	0	1	1	1
`dx_hpp1`	0	0	0	0	1	1
`dx_hpp2`	0	1	1	1	0	0
$n =$	9	5	6	8	8	7

Table 20: Best feature combination for compilation of a complete sample of A-type stars.

Cost factors were selected by using the cost factor adjustment tool described in Sect. 3.6. They were chosen such that no spectrum of the classes A5–8 and A9–F2 (the target classes) were classified into one of the other classes, and such that the contamination of the sample is as low as possible.

We selected stars assigned to the classes A5–8 and A9–F2 having `dx_hpp2` > -100 as FHB/A star candidates.

6.2 Follow-Up Observations

BV photometry of 104 HES targets close to the SGP, and additional UB photometry of 58 of these stars was obtained by C. Flynn and B. Schuster in the nights October 6–11, 1998, with the ESO Danish 1.54 m telescope, with DFOSC. The accuracies obtained for $B-V$ and $U-B$ are $\sigma_{B-V} < 0.015^m$ and $\sigma_{U-B} < 0.03^m$, respectively.

Spectroscopy of HES FHB/A candidates was obtained with the CTIO 4 m telescope on December 12–15, 1998 by T. Beers and S. Rossi. The spectra have a dispersion of 0.5 Å/pixel, and a typical S/N of 20. 86 stars with available photometry from the ESO run were observed. In the direction of Galactic anti-rotation, additional 74 spectra were obtained, and in the Galactic anti-center direction, we obtained another 46 spectra, so that a total of 206 stars were observed.

The results of the follow-up campaigns for the 58 stars with available UBV photometry and spectroscopy are listed in Tab. 27 on pp. 110–111 in Appendix C. As is usual in high Galactic latitude samples of A-type stars (Wilhelm et al. 1999*b*), $\sim 1/3$ are main-sequence stars. In Sect. 6.4 we outline how an improved selection might be able to reduce this fraction considerably. However, the very good news is that 91 of 104 stars for which $B-V$ is available, or 88 %, are A-type stars, so that our selection by automatic classification works very well. The remaining stars are just too cool ($B-V > 0.3$). However, these stars, being main-sequence stars close to the turnoff, are interesting in themselves, since at those temperatures predominantly metal-poor stars are found.

In the next section we evaluate the FHB/A candidate selection in more detail.

6.3 Evaluation of the FHB/A Candidate Selection

For an evaluation of the automatic classification used for FHB/A candidate selection one has to compare the *real* classes with the classes automatically assigned. The problem then is: Where can we get the real classes from? It would be possible *in principle* to classify the available moderate resolution spectra with the classification criteria of the MK system, since the spectral resolution is high enough, and the S/N probably sufficient, if the spectra are smoothed to the spectral resolution used in the MK system (~ 2 Å). However, the MK system is not applicable to our spectra, since we are dealing with *metal-poor* stars. This would require to expand the two-dimensional MK system to a third dimension, i.e. [Fe/H], and to use different classification criteria for the two dimensions used in the MK system, since metallicity influences the strengths of the lines used.

In order to get a *rough* idea of the real classes of our stars, we derived a relation between $(B-V)_0$ and spectral type, by using the library of MK classified spectra of Jacoby et al. (1984). We used all 33 stars of class B9–F3 in that data set, and defined stars of class B9 to have class number $i=1$, A0$=2,\ldots,$ F3$=14$. By a straight line fit, we obtained the relation (see also Fig. 42:)

$$i = 2.65 + 29.5 \cdot (B-V)_0. \tag{42}$$

Spectral classes were computed for the 104 stars for which we have a $B-V$ measurement using the above relation. Note that *reddening* causes a systematic offset between the classification system used for automatic classification, and the classification system defined by Eq. 42. The average reddening in

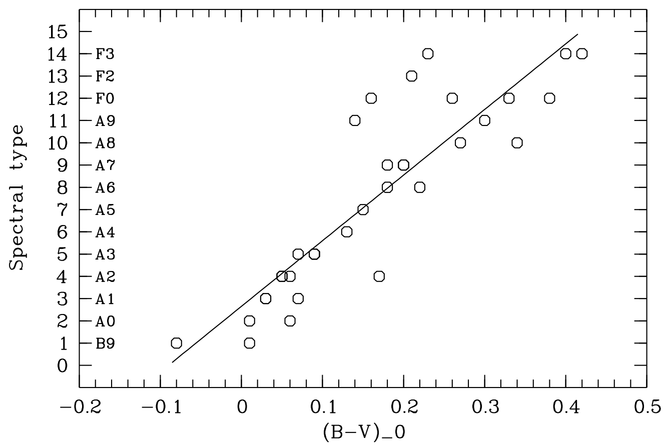

Figure 42: Calibration spectral type versus $(B-V)_0$, derived by using the data of Jacoby et al. (1984).

the sample of 1121 high latitude A-type stars of Wilhelm et al. (1999*b*) is $E(B-V) = 0.044$. Since it follows from Eq. 42 that

$$\sigma_i = 29.5\sigma_{B-V}, \tag{43}$$

the offset between both systems is expected to be ~ 1.3 classes. However, we are mainly interested in evaluating the *scatter* of the classes, and not zero point offsets. The result is shown in Fig. 43.

There is a systematic offset between the automatically assigned classes, and the classification from $(B-V)$. The direction of the offset is opposite to what is expected from the above reddening arguments: In the $(B-V)$-system, the stars are assigned to *earlier* types. In case of class A5–8, this can be explained by the fact that stars earlier than A5 are not represented in our learning sample (which was due to lack of objects). Since we have not applied a reject rule, stars of earlier spectral type have probably been assigned to A5–8.

In case of class A9–F2, there is an offset present between the $(B-V)$-system and the MK system already in the learning sample (see Fig. 44), which is in the same order of magnitude as the offset present in the test sample. Additionally, a few cooler stars might have been rejected from the candidate sample in the process of visual inspection.

The classification accuracy achieved with automatic classification is hardly better than could be achieved by applying the precise $B-V$ colours available *today* for all HES spectra: The error of the $B-V$ calibration for blue stars is $\sigma_{B-V} = 0.12$, which results in a classification error of 3.5 classes.

6.4 Identification of Main-Sequence A-Type Stars

Since we are interested in distant horizontal branch stars rather than main-sequence stars in the applications indicated above, it is desired to clean the sample of FHB/A candidates as much as possible from the latter stars. Therefore, we explored if this could be possible by using Strömgren c_1 coefficients.

As a test sample we used 45 unsaturated HES stars from the follow-up campaigns carried out in 1998, for which have UBV photometry and spectra, and 214 not saturated stars from Wilhelm et al. (1999*b*) present on HES plates. Both types of stars are not clearly separable by c_1 (see Fig. 45); however, it is possible to reduce the contamination with main-sequence stars at moderate cost of completeness. By using the simple selection criterion $c_1 > 0.9$ for FHB/A stars, a sample with 71 % com-

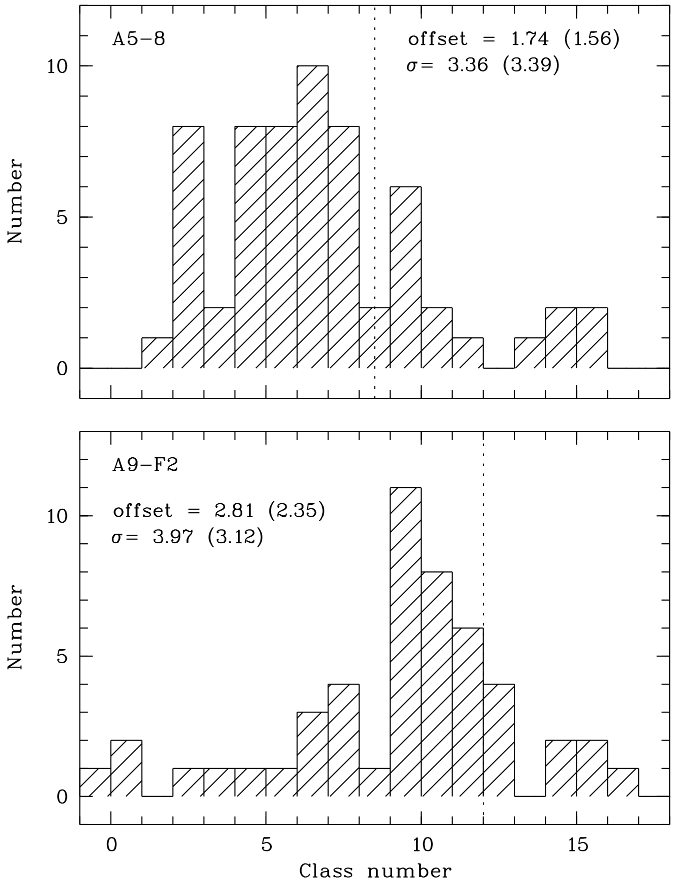

Figure 43: Evaluation of A-type star classification

pleteness can be generated, which has a contamination of 15 % only, compared to 35 % before. With a more sophisticated selection algorithm, e.g. automatic classification, it should be possible to decrease the contamination even more.

As can be seen from Fig. 49, the use of c_1 also allows to clean the *raw* sample from DA white dwarfs. Up to now, these objects have been rejected by visual inspection.

6.5 Outlook

Spectra of an additional set of 109 HES FHB/A candidates have been taken at the CTIO 4 m in October 1999, and spectra of 10 stars in January 2000 with the Kitt Peak 4 m telescope. The data are currently being reduced, and will be analyzed soon.

The author is founding member of the DIST (**D**istance to the **I**SM through **S**tellar **T**argets) consortium which aims at coordinating efforts of distance determinations of HVCs.

Acknowledgements

I thank T. Beers, S. Rossi, C. Flynn and B. Schuster for carrying out the follow-up observations. S. Rossi and C. Flynn did the data reduction of the spectroscopy and photometry runs, respectively, and T. Beers carried out the analysis of the spectra.

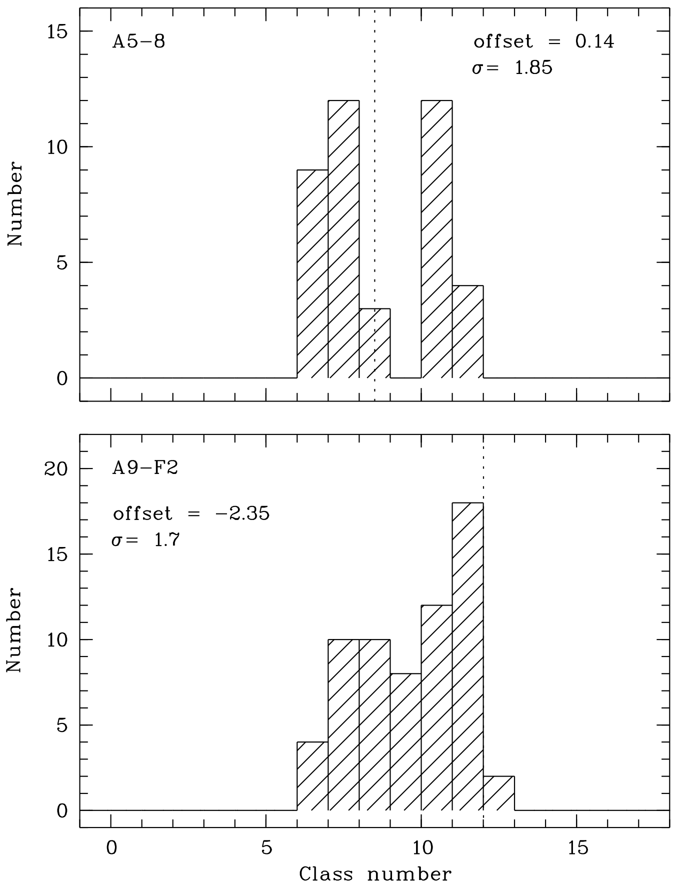

Figure 44: Class distribution of A-type stars in learning sample

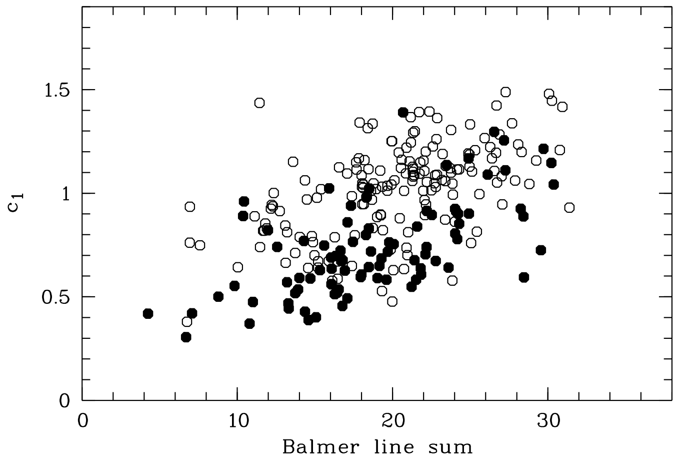

Figure 45: Separation of main-sequence A-type stars (filled circles) and FHB/A stars (open circles) by Strömgren c_1.

References

Blitz, L., Spergel, D. N., Teuben, P. J., Hartmann, D. & Burton, W. B. (1999), 'High-Velocity Clouds: Building Blocks of the Local Group', *ApJ* **514**, 818–843.

Doinidis, S. P. & Beers, T. C. (1989), 'Evidence for clustering of field horizontal-branch stars in the Galactic halo', *ApJ* **340**, L57–L60.

Jacoby, G., Hunter, D. & Christian, C. (1984), 'A library of stellar spectra', *ApJ Suppl.* **56**, 257–281.

van Woerden, H., Wakker, B. P., Schwarz, U. J., Peletier, R. F. & Kalberla, P. M. W. (1998), The High-Velocity Clouds: Galactic or Extragalactic?, *in* D. Breitschwerdt, M. J. Freyberg & J. Truemper, eds, 'IAU Coll. 166: The Local Bubble and Beyond', Vol. 506 of *Lecture Notes in Physics*, Springer, Berlin, pp. 467–470.

Wakker, B. P. & van Woerden, H. (1997), 'High-Velocity Clouds', *ARA&A* **35**, 217–266.

Wakker, B. P., Howk, J. C., Savage, B. D., van Woerden, H., Tufte, S. L., Schwarz, U. J., Benjamin, R., Reynolds, R. J., Peletier, R. F. & Kalberla, P. M. W. (1999), 'Accretion of low-metallicity gas by the Milky Way', *Nature* **402**, 388–390.

Wilhelm, R., Beers, T. C. & Gray, R. O. (1999*a*), 'Spectroscopy of Hot Stars in the Galactic Halo. II. The Identification and Classification of Horizontal-Branch and Other A-Type Stars', *AJ* **117**, 2308–2328.

Wilhelm, R., Beers, T. C., Sommer-Larsen, J., Pier, J. R., Layden, A. C., Flynn, C., Rossi, S. & Christensen, P. R. (1999*b*), 'Spectroscopy of Hot Stars in the Galactic Halo. III. Analysis of a Large Sample of Field Horizontal-Branch and Other A-Type Stars', *AJ* **117**, 2329–2380.

Yanny, B., Newberg, H. J., Becker, R. H., Laurent-Muehleisen, S., Pier, J. R. & Richards, G. (1999), Faint A stars as tracers of the structure of the Galactic Halo, *in* 'AAS Meeting 194', p. #84.05.

7 White Dwarfs

There is a long list of topics that can be addressed by large samples of white dwarfs (WDs) drawn from the HES. These include:

- Testing the double-degenerate (DD) scenario for SN Ia progenitors, in which a binary, consisting of two white dwarfs of large enough mass, merges and produces a thermonuclear explosion. If this scenario is correct, it should be possible to identify SN Ia progenitor systems by searching for radial velocity (RV) variations in a large enough sample of WDs. Studies carried out so far suffer from too small sample sizes (see Maxted & Marsh 1999), and possibly from the fact that only DA white dwarfs were investigated (Renzini 1999, priv. comm.).

- Determination of the scale height and luminosity function of DA white dwarfs with a large, flux-limited sample of such stars. These quantities provide valuable information on the star formation history of the Galaxy (see e.g. Boyle 1989).

- Increasing the sample of pulsating DA white dwarfs (ZZ Ceti stars) for astroseismological investigations, which allow to study the interior of these stars. Bergeron et al. (1995) report that the ZZ Ceti instability strip consists of the temperature range 11 200–12 500 K. As can be seen in Fig. 47, DAs of such temperatures can very easily identified in the HES, since they have very prominent Balmer lines. However, the challenge in finding ZZ Cetis is to derive accurate effective temperatures directly from the survey material used, since the instability strip is very small. Hence, the selection efficiency for these stars is proportional to the temperature accuracy.

- Magnetic DBs can be used as cosmic laboratory: Quantum mechanical calculations of He I in strong magnetic fields can be tested *only*, since in terrestrial laboratories only magnetic fields up to $\sim 10\,\mathrm{MG}$ can be produced.

- Finding more DZ white dwarfs. DZs are cool ($T_{\mathrm{eff}} \lesssim 10\,000\,\mathrm{K}$) white dwarfs with He rich atmospheres, exhibiting metal lines in their spectra. Accretion scenarios for the origin of metals in the photospheres of DZs predict a hydrogen-to-metal ratio *above* the solar value (see e.g. Dupuis et al. 1993), since the diffusion time scale for metals very short in He-rich atmospheres (e.g., $\sim 10^5$ yrs for Ca in a 15 000 K He-rich WD of 0.6 $\mathrm{M}_{\odot}$; see Paquette et al. 1986), and hydrogen, being lighter than helium, is accumulated on the surface. However, the contrary is observed: the hydrogen-to-metal ratio in DZs is typically several orders of magnitude *below* the solar value (Dupuis et al. 1993). A larger sample of DZs would help to explore which mechanism could be responsible for this.

White dwarfs have been selected in wide angle surveys before, and also in the HES (see below). "Classical" UV excess surveys, like the (MCT; Demers et al. 1986; Lamontagne et al. 2000), or the Edinburgh-Cape survey (EC; Stobie et al. 1997; Kilkenny et al. 1997) can efficiently select complete samples of very hot stars, including white dwarfs. However, completeness at the *cool* end is either sacrificed for efficiency, as in the MCT (see Fig. 46), where only objects with $U-B < -0.6$ enter the sample of stars for which follow-up spectroscopy is obtained, or efficiency is sacrificed for completeness, as in the EC. The EC has been claimed to be 94 % complete for objects of $U-B < -0.4$ down to $B = 16.5$ (Stobie et al. 1997). An intermediate selection step based on photoelectric *UBV* photometry has to be used in the EC to eliminate the large fraction ($\sim 30\,\%$; see Kilkenny et al. 1997) of "normal" F and G type stars. Some of these are metal-poor stars (see Beers et al. 1999), which are interesting in themselves, but as we have seen in Sect. 4, such stars are best selected spectroscopically.

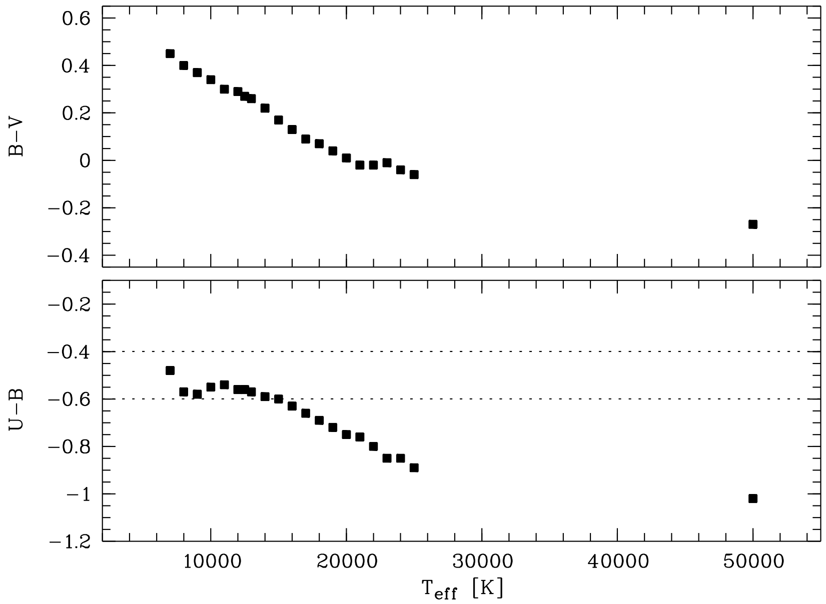

Figure 46: $U - B$ and $B - V$ DAs as a function of effective temperature, determined with model spectra. The selection criterion $U - B < -0.6$ used in the MCT survey leads to rejection of cool ($T_{\rm eff} \lesssim 16000$ K) DA white dwarfs.

In the HES, white dwarfs enter the quasar candidate sample if they have $U - B > 0.18$ (Wisotzki et al. 2000). However, HES quasar candidates are inspected manually at the computer screen, and in this process very hot stars, and stars clearly exhibiting stellar absorption lines (like e.g. DA white dwarfs having strong, broad lines over a wide temperature range; see Fig. 47) are rejected, and follow-up spectroscopy is not obtained for them in the course of the quasar survey. This results in a very efficient quasar selection: typically 70 % of the objects for which follow-up spectroscopy is obtained *are* quasars. The remaining 30 % are mainly hot subdwarfs, cool ($T_{\rm eff} \lesssim 20000$ K) helium-rich white dwarfs (DBs, DCs); a couple of very interesting peculiar objects, e.g., magnetic DBs (Reimers et al. 1998) and magnetic DAs (Reimers et al. 1994, 1996) have been discovered in this way, too. However, if it is intended to compile a *complete* samples of white dwarfs, other selection procedures, as described below, have to be employed.

The dominant population among UV excess objects are hot subdwarfs. In the UV excess sample of the EC, 44.9 % are sdOs or sdBs, and only 14.9 % are white dwarfs (Kilkenny et al. 1997). Ongoing projects in the HES are aiming at specifically selecting such stars. While I am writing these lines, Stefan Dreizler obtains moderate resolution follow-up spectroscopy of HES sdOs at the South African Astronomical Observatory, in order to identify PG 1159 stars among them. Astroseismological analysis of pulsating PG 1159 stars open the possibility to study their interior (Kawaler & Bradley 1994), and improve the general understanding of post-AGB evolution. Another project is devoted to the determination of the scale height, space density and birth rate of sdBs, to clarify their evolutionary origin. An efficient selection of WDs on the one hand, and hot subdwarfs on the other hand both require that these classes of stars can be separated from each other with a reasonable accuracy. In Fig. 48 it is demonstrated that the comparatively high spectral resolution helps a lot in accomplishing this. Automated selection procedures for hot subdwarfs have been developed, and exhaustively tested by simulations, and by using known objects present on HES plates. A description will be given in future publications.

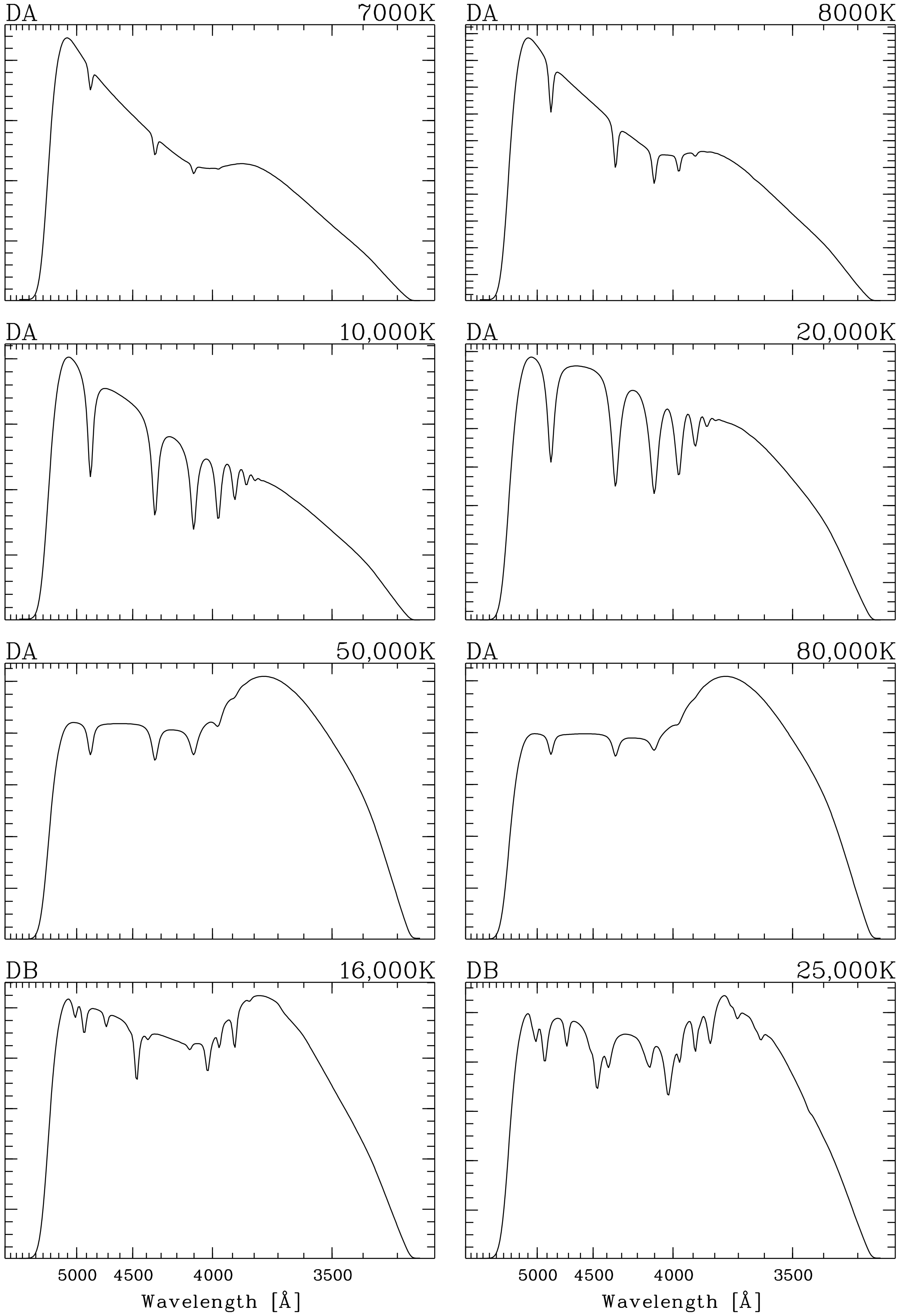

Figure 47: DA and DB White dwarf model spectra, converted to objective prism spectra.

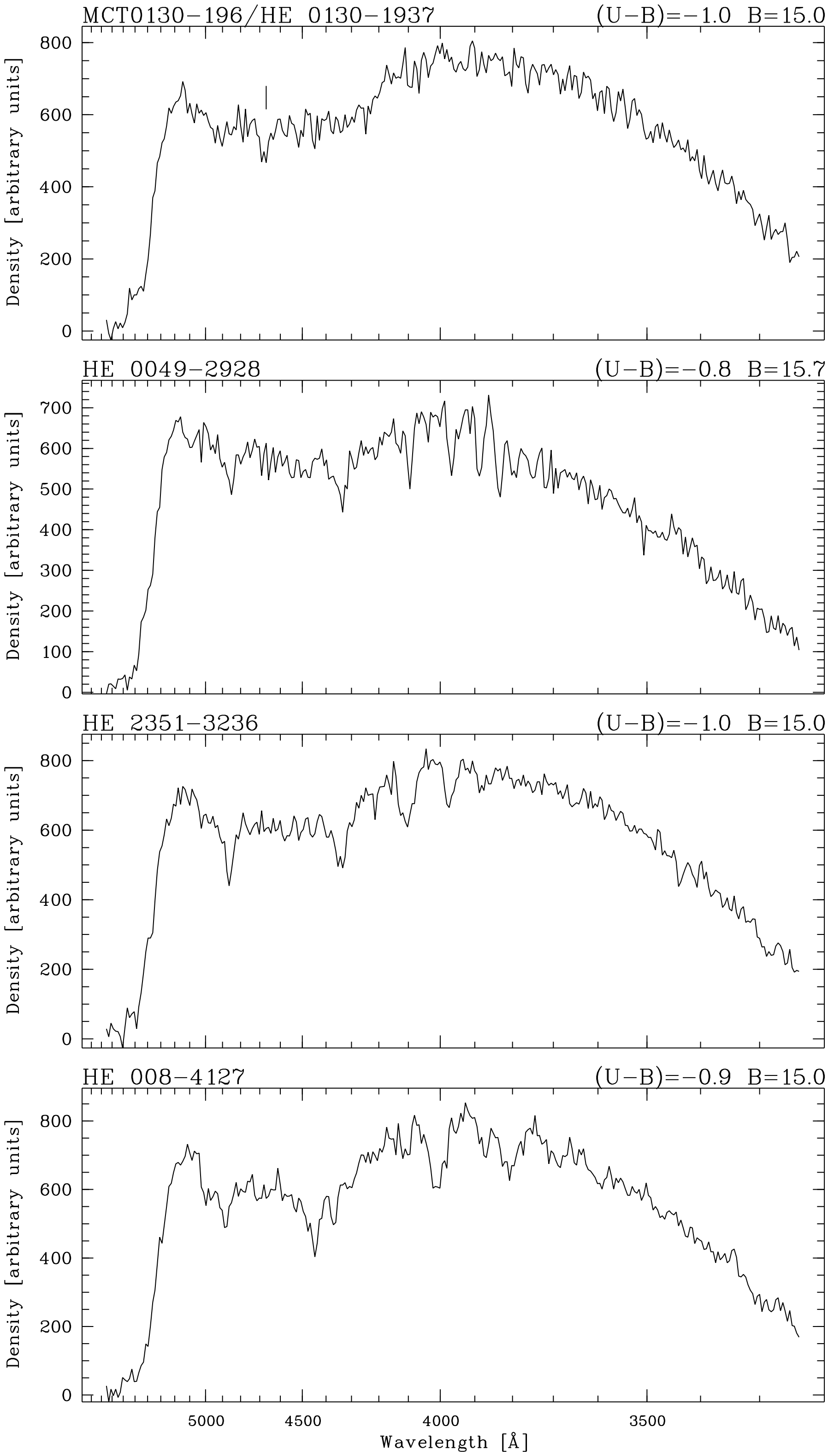

Figure 48: Example spectra of hot stellar objects. From top to bottom: MCT 0130-196, a PG 1159 star luckily showing the blend of He II λ4686 and [CIV] λ4660 (tickmark); HE 0049-2928, a subdwarf B star with prominent Balmer lines; HE 2351-3236, a hot DA white dwarf, showing broader Balmer lines than HE 0049-2928, and a less prominent Balmer jump; HE 0008-4127, a DB white dwarf with strong and broad He I lines.

One major shortcoming of WD selection in the HES may again be the epoch difference problem discussed in Sect. 5. Since most white dwarfs are even fainter than dCs (which have $M_V \sim 10$), the problem may even be more pronounced for WDs *with halo kinematics* then for halo dCs. On the other hand, the local space density of disk stars is ~ 500 times higher than space density of halo stars (Bahcall & Soneira 1984), so that disk WDs, having lower p.m.s, are expected to dominate the WD sample.

How large the incompleteness due to the epoch difference problem is can be roughly estimated from a cross-identification of the HES with the catalog of McCook & Sion (1999). It lists 2 187 objects. 1 633 have an available V measurement. Of these, 1 300 (or 80.0 %) lie in the HES magnitude range ($12 \lesssim V \lesssim 17.5$, assuming an average $B-V$ of zero). 604 objects are located in the southern hemisphere ($\delta < 2\overset{\circ}{.}5$), and at high galactic latitude ($|b| > 30^\circ$). Therefore, we expect ~ 480 WDs to be in the HES area, and detectable in the HES. Taking into account a loss of 20 % due to overlapping spectra, we expect 390 known WDs to be found on all 380 HES plates, and 330 WDs on the 329 plates used in this work. However, in a cross-identification procedure using a $10'' \times 10''$ search box, to compensate for the sometimes very inaccurate coordinates of McCook & Sion (1999), only 151 WDs were found. At the chosen search box width a "saturation" of identified objects was reached; by using a larger box, no further WDs were found. We conclude that the HES WD sample incompleteness is of the order of 50 %, if no special techniques for finding high p.m. objects are used. We describe such techniques in Sect. 7.4 below.

7.1 DA White Dwarfs

In this section we describe two methods for selection of DA white dwarfs in the HES, and give completeness estimates.

7.1.1 Selection by Automatic Classification

A complete search for the best feature combination was run on a set of 14 features. The optimization criterion was the number of misclassifications between the white dwarf classes (10–17), and the remaining classes (1–9). That is, misclassifications between any of the classes 10–17 themselves, and any of the classes 1–9 where *ignored*, since we were mostly interested in separating DA white dwarfs from the remaining stars. The feature combinations found are shown in Tab. 22. As for the previously described applications, there is a tendency to use more features for classification at lower S/N, and to use more continuum shape or broad band colour features.

Stars assigned to classes $\Omega_i, i \geq 10$ were selected; no rejection criterion was applied. The selection was tested on 42 HES fields. In these fields, 18 DA white dwarfs from McCook & Sion (1999) are present; 16 of them (or ~ 90 %) have been re-discovered. An additional test sample were 17 DAs found in the course of the search for FHB/A candidates. 2 of them are also present in the catalog of McCook & Sion (1999). Of these 17 stars, 12 (or ~ 70 %) have been selected. Combining both test samples, we arrive at a completeness estimate of 79 % (26 of 33 stars found). Note that these completeness estimates are *relative* to the sample of McCook & Sion (1999), i.e., we do not know how many stars we miss of those potentially systematically missing in McCook & Sion (1999).

The stars not found were generally assigned to late type star classes. Closer inspection of the reasons for the misclassification revealed that the feature detection failed in both cases; the measured Balmer line equivalent widths are much to low. This is because the feature detection algorithm in its present form is not appropriate for the broad lines of white dwarfs. The algorithm makes use of the assumption that the spectral lines are not resolved, i.e., that the line profile is dominated by the instrumental profile. The line profile widths is held *constant* at the measured widths of the instrumental

i	Class	N	Remarks
1	A5–8	39	
2	A9–F2	67	
3	F3–6	130	
4	F7–G0	119	
5	G1–K0	134	
6	K1–3	65	
7	K4–9	67	
8	SdFearly	33	
9	mphs	100	MPHS-Modell
10	DA07	90	DA, $T = 7\,000$ K; 3 different SSCs
11	DA08	90	DA, $T = 8\,000$ K; 3 different SSCs
12	DA10	90	DA, $T = 10\,000$ K; 3 different SSCs
13	DA15	90	DA, $T = 15\,000$ K; 3 different SSCs
14	DA20	90	DA, $T = 20\,000$ K; 3 different SSCs
15	DA25	90	DA, $T = 25\,000$ K; 3 different SSCs
16	DA50	90	DA, $T = 50\,000$ K; 3 different SSCs
17	DA80	90	DA, $T = 80\,000$ K; 3 different SSCs

Table 21: Learning sample for search of DA white dwarfs. The total sample size is 1 474. Non-DA classes are needed in the learning sample since DAs shall be distinguished from them.

Feature	S/N					
	orig.	25	20	15	10	5
`all5160eqw`	1	1	0	0	1	0
`all4861eqw`	1	1	0	1	1	1
`all4388eqw`	0	1	1	1	1	1
`all4340eqw`	0	0	1	1	0	1
`all4300eqw`	1	1	0	1	1	0
`all4261eqw`	0	0	1	0	0	1
`all4227eqw`	0	0	0	0	1	1
`all4102eqw`	0	0	0	1	1	1
`all3969eqw`	1	1	1	0	1	1
`all3934eqw`	0	0	1	0	1	1
`klcomp_1`	1	1	0	1	1	1
`klcomp_2`	0	0	1	1	0	0
`dx_hpp1`	0	0	0	0	1	1
`dx_hpp2`	0	0	0	0	0	0
$N =$	5	6	6	7	10	10

Table 22: Best feature combinations for compilation of a complete sample of DA white dwarfs.

profile. Moreover, the assumed profile *form*, i.e. a Gaussian profile, is not appropriate for the lines of white dwarfs, which show broad wings.

On 10 of the 42 test fields we inspected the raw candidate sample (typically 30–40 spectra per field) closely. 52 stars were identified as white dwarfs; for some of the hotter stars, it is not possible to say with certainty from the HES spectra alone if they are DAs or DBs.

7.1.2 Selection by Cutoff Lines in Colour-Colour and Feature Space

For the development of an alternative selection method for white dwarfs (and also for the selection of hot stars), we investigated to what extent different types of hot stars can be distinguished in the HES in a two-colour diagram ($U-B$ versus $B-V$), and in the two-dimensional feature space c_1 versus `balmsum`. Using various catalogs, we then identified 521 hot stars in the HES. The catalogs are: (Kilkenny et al. 1997), Wilhelm et al. (1999), an updated version of the Kilkenny et al. (1988) subdwarf catalog (Heber 2000, priv. comm.), and McCook & Sion (1999). Additionally, 39 HES A-type stars with known stellar parameters were included. Since $U-B$, and especially c_1 can be easily confused by overlaps, and our colour calibrations are not valid for saturated stars, we excluded stars above the saturation threshold, and we applied a harder rejection criterion for overlaps (i.e., *no* overlapping object detected, instead of allowing for overlapping objects at $x > 3000$, corresponding to $\lambda < 3830$ Å).

It turned out that high gravity stars (white dwarfs, sdBs, and sdOs) can be distinguished quite reliably from lower gravity stars (main-sequence and horizontal branch stars). By defining selection boxes in the two-colour space, and c_1 versus `balmsum` feature space, it is possible to select DA white dwarfs, and a large fraction of the DBs present in the "learning sample" of 521 objects (see Fig. 49).

We tested this selection with an enlarged sample of 59 DAs and 5 DBs from McCook & Sion (1999) present on HES plates, and 15 of the 17 DAs from the FHB/A candidate set used for evaluation of the automatic classification selection. The enlarged test sample includes 17 of the 18 objects from the previously used McCook & Sion (1999) sample. The remaining objects were excluded by the tighter overlap rejection criterion.

72 of the 74 DAs (or 97 %) and 3 of the 5 DBs (60 %) have been selected by the cutoff line approach. The DBs have probably been selected either because some He I lines are not very far away from the Balmer lines (e.g., He I 4921, 4387), or because of noise. In applications in which DBs are unwanted objects, the DA sample contamination can likely be reduced by applying a higher selection threshold for the sum of Balmer line equivalent widths. However, because DBs are highly desired in the SN Ia progenitor project (see above), we decided to use a rather relaxed criterion ($W_\lambda(\mathrm{H}_\beta+\mathrm{H}_\gamma+\mathrm{H}_\delta) > 0$).

One of the DAs not selected by automatic classification (HE 0315-3314) has been excluded from the test sample by the stronger overlap rejection criterion. It would *not* have been selected if it would have been included into the enlarged test sample. However, from our close inspection of this object we know that the presence of an overlapping object is not the reason for both selection algorithms to fail.

Four objects have not been selected by automatic classification, but selected by the cutoff method. For two of them, it is likely that the usage of the sum of three Balmer lines in the selection was able to compensate the deficiency of the feature detection algorithm described above: The objects have $S/N = 25.2$ and $S/N = 37.3$, respectively, so that they were classified by using the equivalent widths of Hβ and $H\varepsilon$ only (see Tab. 22). We hence conclude that the sum of Balmer line equivalent widths is a more stable feature than the usage of one (or two) Balmer lines only. The other two objects are rather noisy ($S/N > 10$), and for one of them the identification of as DA is uncertain.

One object has been selected by automatic classification, but *not* by the cutoff method. It is again a faint object ($B_J = 17.3$; $S/N = 5.7$).

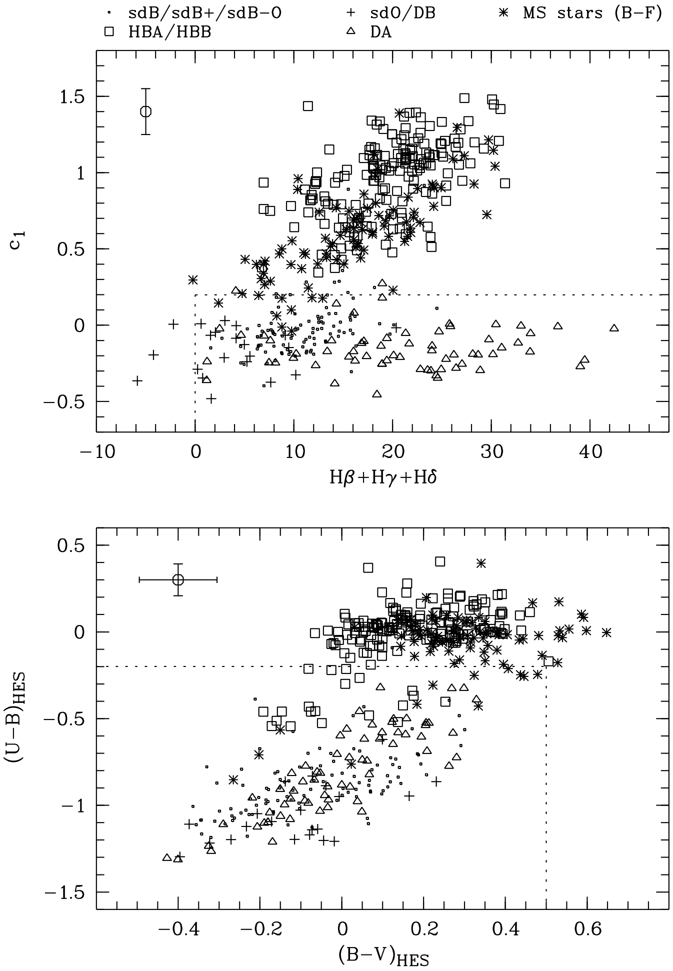

Figure 49: DA selection in colour-colour space and c_1 versus Balmer line sum feature space. In the upper left corner, error bars for c_1, $U-B$ and $B-V$ are displayed.

7.1.3 Discussion

Since 4 DAs have been selected by the cutoff method, but not by automatic classification, but only one object has not been selected by the cutoff method, but by automatic classification, we conclude that the former selection method might currently lead to slightly more complete DA samples than automatic classification. However, based on the tests carried out, it is not possible to attribute the superiority of the cutoff selection to the algorithm itself, since in both of the two cases in which we can rule out noisy spectra to be the likely reason for the non-selection, we have indications that the usage of a set of more stable features may have lead to selection.

Our completeness estimates for the cutoff method (97 % for DAs, and 60 % for DBs) are *relative* to a sample of southern hemisphere white dwarfs from catalog of McCook & Sion (1999), since most of the test objects (59 of 74) are from that source. The catalog lists objects from many different sources, and it is not clear if any selection biases are present in our test sample. Therefore, we can not exclude that we are systematically missing objects that have already been missed in previous surveys, and we can only derive an estimate of the *relative* completeness. Estimations of the *absolute* completeness can only be derived by simulations in which model atmospheres covering the whole possible range of stellar parameters are converted to objective prism spectra, and processed by the selection algorithm.

It has not yet been tested how *clean* the samples of DAs (or DAs and DBs in case of the cutoff method) are. This requires spectroscopic follow-up observations.

A *rough* surface density estimate of DAs can be derived by using our sample selected by automatic classification. The sample selected by the cutoff method cannot be used for these purposes, since the harder overlap criterion results in a decrease of the effective HES area, which we have not yet quantified. 19 of the 52 white dwarfs we selected are DAs with $B < 16.4$. We follow the arguments of Homeier et al. (1998) and apply a correction of $-3.4\,\%$ to our counts ($\sigma_{B_J} = 0.2$ in the HES), to account for scatter of faint objects into our sample by photometric errors, so that we arrive at 18 DAs. The predicted number of DAs from the PG survey (Green et al. 1986) for our 10 fields, assuming an average effective area of $20\,\mathrm{deg}^2$ per plate, is 11. We hence confirm the result of Homeier et al. (1998), who suspected that the DA sample from the PG survey is incomplete by a factor of the order of 2. Our result is *conservative*, since we have not corrected our counts for incompleteness.

As has already been suspected by Goldschmidt et al. (1992) for the quasar sample drawn from the PG, the reasons for the survey being incomplete are inaccurate, and systematically too bright B magnitudes, and inaccurate colours. Köhler et al. (1997) confirm the incompleteness of the PG quasar sample by using a complete sample of quasars drawn from the HES. They found a 3.6 times higher surface density of quasars at $B = 16$. Wisotzki (1998) later derived a somewhat lower surface density discrepancy (i.e., a factor 1.48 higher surface density than found by the PG), by using a larger HES quasar sample, to which a correction for Galactic extinction was applied.

The selection criterion for UV excess stellar objects in the PG was $U-B < 0.46$ where $U-B$ has an error of $\sigma_{U-B} = 0.38$ (Green et al. 1986). As can be seen from Fig. 46, this means that a considerable fraction of DA white dwarfs below $\sim 15\,000$ K are likely not found by the PG. 23 of the 69 DA white dwarfs (or 1/3) listed in Homeier et al. (1998) have $T_{\mathrm{eff}} < 15\,000$ K, so that the incompleteness of the DA sample drawn from the PG found by Homeier et al. (1998) can at least partly explained by missing cool DAs.

7.2 Magnetic DBs: A Cosmic Laboratory

Reimers et al. (1998) reported the discovery of four magnetic DBs in the HES. Unfortunately, based on higher quality spectra, three out of the four stars published in Reimers et al. (1998) turned out to be a rare type of binary system, i.e. a hot subdwarf with K-type secondary. However, one of the stars, HE 0241-0155, is *really* a magnetic DB, with field strengths of ~ 25 MG. Using this star, we implemented a selection algorithm that uses a feature at ~ 4200 Å, which is a stationary He I feature (Jordan 2000, priv. comm.), and a further feature at ~ 4200 Å (see Fig. 51). A search on 104 HES plates revealed 8 highly ranked candidates. Spectroscopy of these candidates is currently being obtained at ESO.

7.3 DZ White Dwarfs

Three DZ white dwarfs, HE 0122-2244, HE 0446-2531 and HE 0449-2554, entered the HES quasar candidate sample because of their blue continuum (see Fig. 53). HE 0449-2554 and HE 0122-2244 have been observed in October 1997 with the ESO 1.52 m telescope at low spectral resolution (~ 15 Å), and limited S/N. These spectra confirmed their DZ nature.

In order to increase the sample of DZs, we implemented a selection algorithm which looks for hot objects ($B-V < 0.4$) showing weak or absent Balmer lines, and a strong Ca K line. Application of this

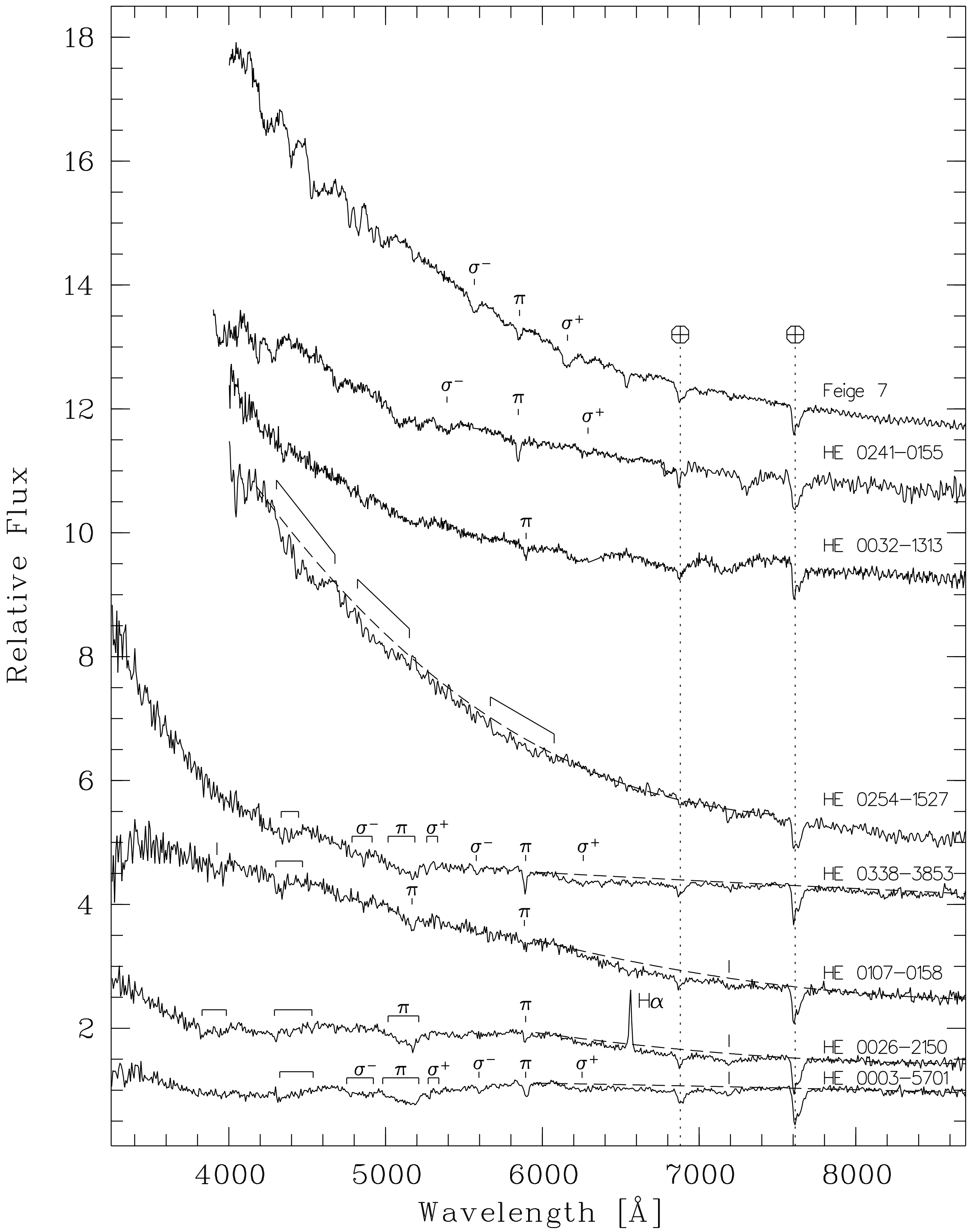

Figure 50: Spectra of the magnetic DB white dwarfs Feige 7, and HE 0241-0155. The lower four objects turned out to be binaries, and *no* magnetic DBs. The lines identified as π component of He I 5876 are Na I D in reality; the band-like features are MgH bands of K dwarf secondaries. The nature of HE 0032-1313 is still unclear.

Passband	Use for band index	
	`magDBidx1`	`magDBidx2`
4370–4636 Å		cont
4167–4307 Å		flux
4065–4141 Å	cont	cont
4029–4065 Å	flux	

Table 23: Wavelengths of passbands used for computation of indices for stationary He I features.

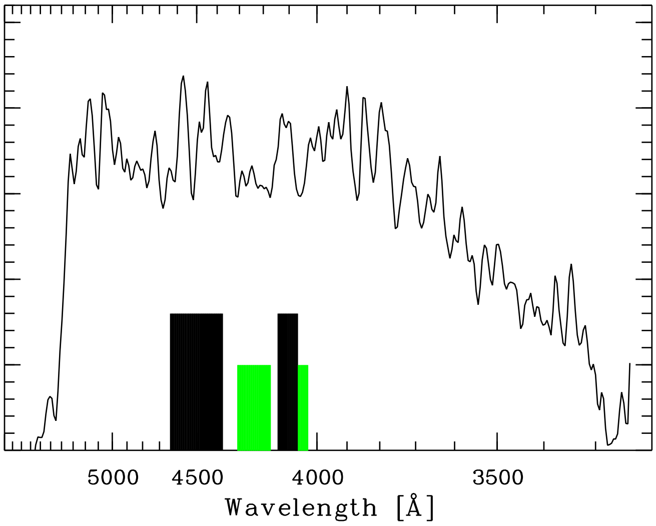

Figure 51: Smoothed HES spectrum of the magnetic DB HE 0241-0155, illustrating the positions of continuum (black, high boxes) and line (grey, low boxes) bandpasses defining the feature indices used for the selection of magnetic DBs.

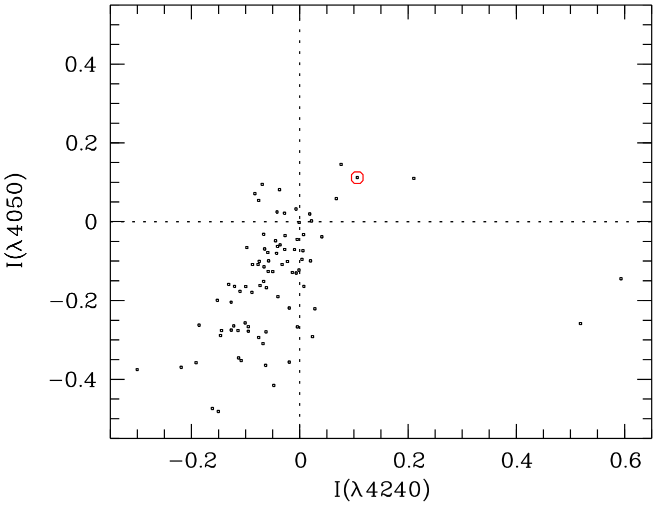

Figure 52: Feature index selection box for magnetic DBs. Dots are all objects with $B-V<0.3$ on one HES plate; HE 0241-0155 is encircled.

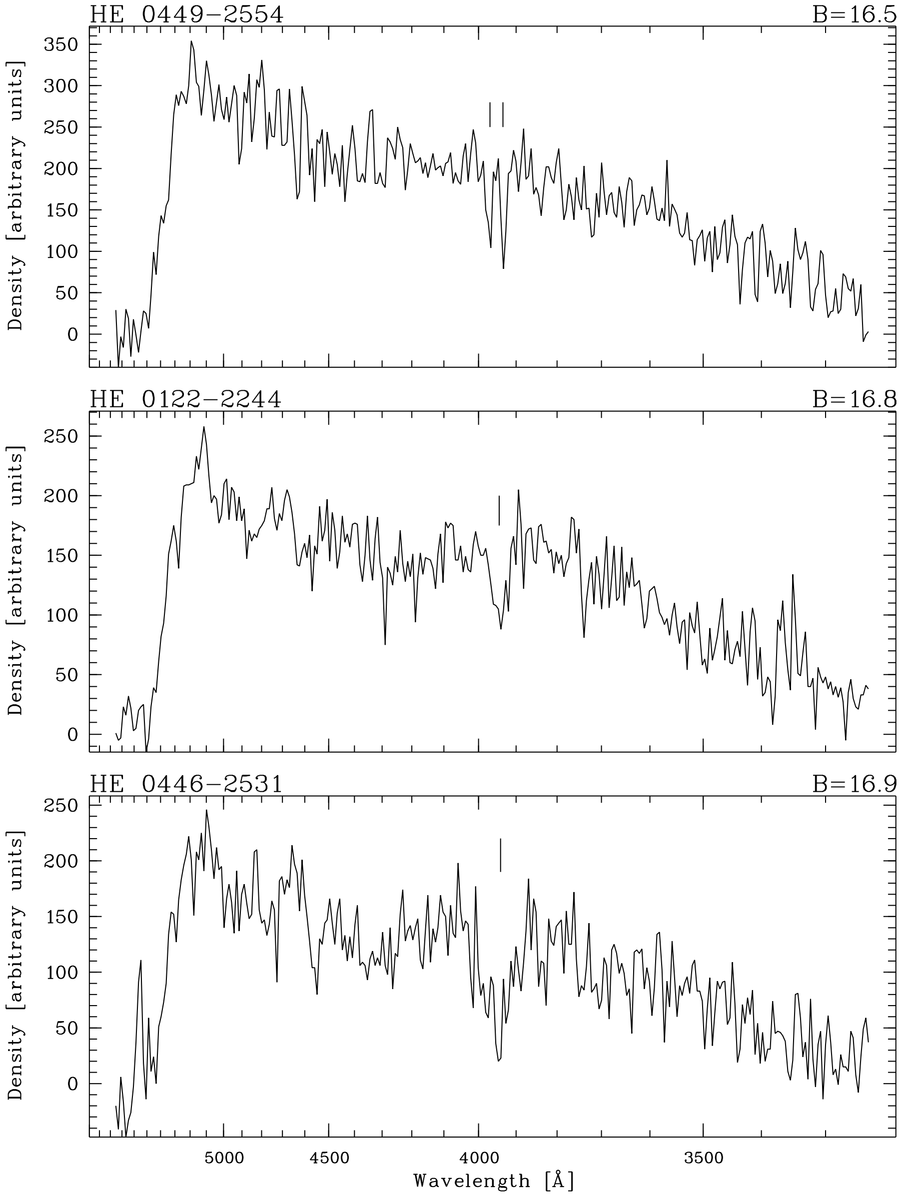

Figure 53: HES spectra of three DZ white dwarfs that entered the HES quasar candidate sample. Note the strong Ca H+K absorption feature at ~ 3950 Å. In the spectrum of HE 0449-2554, Ca H and Ca K are resolved.

selection to 131 HES fields yielded 17 new candidates for DZs.

Better quality spectra of HE 0122-2244, HE 0446-2531 and HE 0449-2554, and 2 of the 17 newly selected DZs were obtained by the author in the night November 27–28, 1998, with DFOSC attached to the ESO-Danish 1.54 m telescope. Grism #4 and a $5''$ slit, rotated to parallactic angle, was used, yielding a seeing-limited spectral resolution of 10 Å and a covered wavelength range of $3500\,\text{Å} < \lambda < 7000\mathring{A}$. Before each observation the slit was rotated such that it was in parallactic angle after half of the exposure time.

HE 0446-2531 was confirmed as DZ, but the two new DZ candidates turned out to be normal stars. Follow-up observations of the remaining objects is under way.

7.4 Outlook

The solution of the epoch difference problem is simple in principal: One just has to take a look at all HES spectra that potentially belong to mis-extracted objects, i.e., spectra with very low S/N, that *should* have a higher S/N according to the brightness on the direct plate. For these objects, the DSS-I positions could be compared with positions on a plate taken at another epoch (that data can be easily retrieved from online archives). This should yield a p.m. for most of the stars, which can be used to compute the coordinates at the HES plate epoch. These provide the information where to extract the HES spectrum. This procedure should not only reveal most of the missed WDs, but also a lot of other interesting objects, e.g. dwarf carbon stars.

A refined feature detection algorithm adapted for the broad lines of white dwarfs will also soon be implemented.

Even *without* solving the p.m. problem, we expect to find ~ 2000 white dwarfs in the HES, when we extrapolate the number of white dwarfs found by automatic classification (52 in 42 fields), to the total survey. McCook & Sion (1999) list a total 1715 white dwarfs of type DA or DB; 662 of them are in the southern hemisphere ($\delta < +2\overset{\circ}{.}5$). This means that the HES is able to at least *double* the total number of known white dwarfs, and to at least *triple* their number in the southern hemisphere.

A survey program for radial velocity variations of WDs using UVES at VLT UT1 has been approved by ESO as a Large Programme. However, in difference to usual Large Programmes, our project has low priority; i.e., our targets will be observed only when the weather conditions on Paranal do not fulfill the requirements specified in other programs. As has been pointed out by Gilmozzi (1999), in period 63 (April–September 1999) there was a very small number of programs that could be carried out at seeing $> 1''$, full moon, or under non-photometric conditions. Therefore, we are optimistic to receive a considerable amount of data.

Acknowledgements

I thank D. Koester, U. Heber and S. Dreizler for providing model atmospheres for WDs, sdBs and sdOs, respectively. I also acknowledge many valuable discussions, and extensive communication by e-mail.

References

Bahcall, J. N. & Soneira, R. M. (1984), ‘Comparisons of a standard galaxy model with stellar observations in five fields’, *ApJS* **55**, 67–99.

Beers, T. C., Rossi, S., O’Donoghue, D., Kilkenny, D., Koen, C. & Stobie, R. S. (1999), Metal Abundance Estimates for F- and G-Type Stars from the Edinburgh-Cape Blue Object Survey, *in* B. Gibson, T. Axelrod & M. Putman, eds, ‘The Third Stromlo Symposium: The Galactic Halo’, Vol. 165 of *ASP Conf. Ser.*, pp. 254–258.

Bergeron, P., Wesemael, F., Lamontage, R. & Fontaine, G. (1995), ‘Optical and ultraviolett analyses of ZZ Ceti stars and study of atmospheric convective efficiency in DA white dwarfs’, *ApJ* **449**, 258–279.

Boyle, B. J. (1989), ‘The space distribution of DA white dwarfs’, *MNRAS* **240**, 533–549.

Demers, S., Beland, S., Kibblewhite, E. J., Irwin, M. J. & Nithakorn, D. S. (1986), 'The Montreal-Cambridge survey of southern subluminous blue stars', *AJ* **92**, 878–884.

Dupuis, J., Fontaine, G. & Wesemael, F. (1993), 'A study of metal abundance patterns in cool white dwarfs. III – Comparison of the predictions of the two-phase accretion model with the observations', *ApJS* **87**, 345–365.

Gilmozzi, R. (1999), 'The first six months of VLT science operations', *The Messenger* **98**, 25–27.

Goldschmidt, P., Miller, L., LaFranca, F. & Cristiani, S. (1992), 'The high surface density of bright ultraviolet-excess quasars', *Monthly Notices of the Royal Astronomical Society* **256**, 65p–68p.

Green, R. F., Schmidt, M. & Liebert, J. (1986), 'The Palomar-Green catalog of ultraviolet-excess stellar objects', *ApJS* **61**, 305–352.

Homeier, D., Koester, D., Hagen, H.-J., Jordan, S., Heber, U., Engels, D., Reimers, D. & Dreizler, S. (1998), 'An analysis of DA white dwarfs from the Hamburg Quasar Survey', *A&A* **338**, 563–575.

Kawaler, S. D. & Bradley, P. A. (1994), 'Precision asteroseismology of pulsating PG 1159 stars', *ApJ* **427**, 415–428.

Kilkenny, D., Heber, U. & Drilling, J. S. (1988), 'A catalogue of spectroscopically identified hot subdwarf stars', *SAAO Circ.* **12**, 1–80.

Kilkenny, D., O'Donoghue, D., Koen, C., Stobie, R. S. & Chen, A. (1997), 'The Edinburgh-Cape Blue Object Survey – II. Zone 1 – The North Galactic Cap', *MNRAS* **287**, 867–893.

Köhler, T., Groote, D., Reimers, D. & Wisotzki, L. (1997), 'The local luminosity function of QSOs and Seyfert 1 nuclei', *A&A* **325**, 502–510.

Lamontagne, R., Demers, S., Wesemael, F., Fontaine, G. & Irwin, M. J. (2000), 'The Montreal-Cambridge-Tololo Survey of Southern Subluminous Blue Stars: The South Galactic Cap', *AJ* **119**, 241–260.

Maxted, P. F. L. & Marsh, T. R. (1999), 'The fraction of double degenerates among DA white dwarfs', *MNRAS* **307**, 122–132.

McCook, G. P. & Sion, E. M. (1999), 'A catalog of spectroscopically identified white dwarfs', *ApJS* **121**, 1–130.

Paquette, C., Pelletier, C., Fontaine, G. & Michaud, G. (1986), 'Diffusion in white dwarfs – New results and comparative study', *ApJS* **61**, 197–217.

Reimers, D., Jordan, S., Beckmann, V., Christlieb, N. & Wisotzki, L. (1998), 'Four magnetic DB white dwarfs discovered by the Hamburg/ESO survey', *A&A* **337**, L13–L16.

Reimers, D., Jordan, S., Koehler, T. & Wisotzki, L. (1994), 'HE 1045-0908: a new magnetic DA white dwarf with a distinctive Zeeman line splitting pattern', *A&A* **285**, 995–997.

Reimers, D., Jordan, S., Koester, D., Bade, N., Koehler, T. & Wisotzki, L. (1996), 'Discovery of four white dwarfs with strong magnetic fields by the Hamburg/ESO Survey.', *A&A* **311**, 572–578.

Stobie, R. S., Kilkenny, D., O'Donoghue, D., Chen, A., Koen, C., Morgan, D. H., Barrow, J., Buckley, D. A. H., Cannon, R. D., Cass, C. J. P., Cranston, M. R., Drinkwater, M., Hartley, M., Hawkins, M. R. S., Hughes, S., Humphries, C. M., Macgillivray, H. T., McKenzie, P. B., Parker, Q. A., Read, M., Russell, K. S., Savage, A., Thomson, E. B., Tritton, S. B., Waldron, J. D., Warner, B. & Watson, F. G. (1997), 'The Edinburgh-Cape Blue Object Survey – I. Description of the survey', *MNRAS* **287**, 848–866.

Wilhelm, R., Beers, T. C., Sommer-Larsen, J., Pier, J. R., Layden, A. C., Flynn, C., Rossi, S. & Christensen, P. R. (1999), 'Spectroscopy of Hot Stars in the Galactic Halo. III. Analysis of a Large Sample of Field Horizontal-Branch and Other A-Type Stars', *AJ* **117**, 2329–2380.

Wisotzki, L. (1998), 'The evolution of optically luminous QSOs', Habilitationsschrift, University of Hamburg.

Wisotzki, L., Christlieb, N., Bade, N., Beckmann, V., Köhler, T., Vanelle, C. & Reimers, D. (2000), 'The Hamburg/ESO survey for bright QSOs. III. A large flux-limited sample of QSOs', A&A, in press.

8 A Homogeneously Selected Sample of Cataclysmic Variable Stars

There is an enormous discrepancy of up to two orders of magnitude between the observed space density of cataclysmic variable stars (CVs), and population synthesis calculations. Patterson (1984) give an observed space density of $\sim 10^{-6}\,\mathrm{pc}^{-3}$, whereas Kolb (1993) predict $\sim 10^{-4}\,\mathrm{pc}^{-3}$ from theoretical calculations. This discrepancy has been attributed to a bias in the selection of CVs. Bright detection limits in surveys carried out so far may have led to preferential selection of *high* mass transfer systems (Patterson 1984; Shara 1986), whereas population studies indicate that the population of CVs is dominated by *low* mass transfer systems; i.e., mainly dwarf novae (DN). DNs show very infrequent outbursts, and are intrinsically faint, so that they may have been missed by surveys with bright detection limits. Patterson (1984) argue that this "hidden population" of CVs may amount to $\sim 99\,\%$ of all CVs.

The HES with its deep limiting magnitude, and high spectral resolution, making it possible to resolve the broad emission lines of CVs, offers the chance to look for this hidden population. Examples for HES spectra of CVs are shown in Fig. 54. The final aim of the project is to determine the scale height and space density of a well-defined sample of CVs.

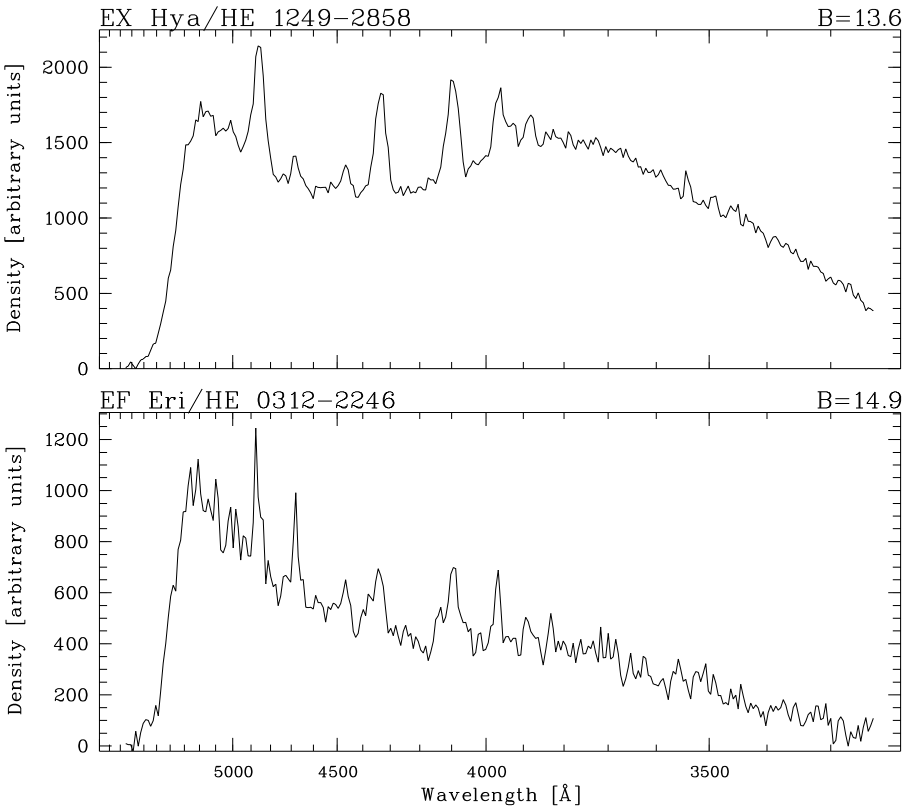

Figure 54: HES spectra of cataclysmic variable stars. Upper panel: the dwarf nova EX Hya; lower panel: EF Eri, a magnetic CV. In this type of object the formation of an accretion disc is prevented by strong magnetic fields. The absence of an accretion disc results in a less blue continuum.

We select CVs in the HES with the help of a feature detection algorithm similar to that described in Sect. 3.2. In the version adapted for CVs, the continuum is not determined by filtering, but is fitted simultaneously with the stellar lines under consideration. The selection criteria for CVs were:

(a) UV excess, i.e. `dx_hpp1`> 0, corresponding to $(U-B) \lesssim -0.18$

(b) Detection of Hβ in emission.

On an effective area of $\sim 1500\,\mathrm{deg}^2$ we identified 20 CV candidates. 6 of them could be identified as galaxies with the help of DSS-I images; another 5 were already known CVs. The remaining 9 candidates have been observed at the ESO-Danish 1.54 m-telescope in November 1997 with a resolution of $R = 1\,300$ (Grism #7 with $1''$ slit), which allows to resolve emission lines broader than 230 km/s. Since in CVs gas of the secondary is accreted onto the surface of a white dwarf, having a small radius, the velocity components of the gas along the line of sight in the inner part of the accretion disc are typically much higher than 230 km/s. This enables us to distinguish CVs from T Tauri stars, in which a much larger star sits in the middle of the accretion disc, so that lower velocities occur, and from dMe stars, with photospheric, unresolved lines.

Of the 9 stars observed, 6 have been confirmed as CVs; the remaining three are a dMe star, a T Tauri star, and a QSO, respectively. Hence, of the original set of 14 candidates, 11 (or 79 %) are CVs. This is the highest selection efficiency ever obtained in a survey for CVs. One of the CVs discovered in the HES, HE 0409-3029, turned out to be an eclipsing binary with a period of $\sim 3^h\,25^m$ (Augusteijn 1998, priv. comm.).

A first, rough estimate of the surface density of CVs based on our small sample indicates that in the HES, $\sim 3\times$ more CVs are found than in the Calán-Tololo Survey (CTS), when we apply the HES limiting magnitude to the CTS sample (Augusteijn 1998, priv. comm.). In the CTS, CVs are searched *by eye* on objective prism plates. The limiting magnitude of the CTS is $B_J = 18.5$. The above estimate is consistent with the fact that 5 of the 11 confirmed HES CVs *should* have been found in the CTS, since the survey areas overlap, but only 2 *have* been found. This suggests again, as in case of metal-poor stars, that quantitative selection criteria applied to digital data are superior to manual selection. However, our arguments are so far based on small numbers only.

Acknowledgements

The search for CVs was carried out in collaboration with T. Augusteijn and C. Tappert. Thomas carried out the follow-up observations of HES CVs.

References

Kolb, U. (1993), ‘A model for the intrinsic population of cataclysmic variables’, *A&A* **271**, 149–166.

Patterson, J. (1984), ‘The evolution of cataclysmic and low-mass X-ray binaries’, *Astrophyisical Journal Supplement* **54**, 443–493.

Shara, M. (1986), ‘Do novae hibernate during most of the millennia between eruptions?’, *ApJ* **311**, 163–171.

9 Conclusions

I have demonstrated that the digital data base of the HES is a *gold mine* for various types of scientifically exciting stars. Exhaustive efforts to calibrate the HES plate material, and understand the properties of these detectors enable us to select a large variety of stars by *quantitative*, *objective* and *reproducible* selection criteria, and to study the selection probability as a function of stellar parameters and object brightness.

Several stellar projects carried out in the HES indicate that quantitative selection on a digitized objective prism plates are dramatically superior to “manual” selection with binocular microscopes. I have shown that samples selected in the latter way are either highly *incomplete* (as in case of carbon stars, and CVs, although in the latter the HES sample size is still small), or much more *contaminated* with undesired objects than expected for the quality of the spectra used, as in case of metal-poor stars, where I achieved a 3–7 times higher selection efficiency in the HES as compared to the HK survey, which has a 2 times *higher* spectral resolution.

The faint limit of the HES ($B_J \simeq 17.5$) harmonizes very well with the limit to which high-resolution ($R > 40\,000$) spectroscopy is feasible with the new generation of > 8 m class telescopes (e.g., VLT, Subaru, Keck, and HET). It is thus an ideal source for providing targets for these telescopes. Moreover, since the HES is *unique* in the sense that currently no other survey provides as many spectra of a spectral resolution as high as in the HES, I predict that in the next years the scientific community will confront the HES group with an even greater demand of rare and peculiar stellar objects as the author experienced throughout his thesis work.

A HES Metal-Poor Stars

Name	α(2000)	δ(2000)	B_J	V	$B-V$	$T_{\rm eff}$	$\log g$	$[Fe/H]_{HES}$	$[Fe/H]_{HK}$	Method
HE 0000-5003	00 03 17.0	-49 46 32	16.6	16.3	0.3	6000	3.5	-2.0	-2.5	auto
HE 0007-1832	00 09 52.8	-18 16 12	15.9	15.6	0.4	6200	4.1	-2.5	-3.0	auto
HE 0008-3842	00 10 56.0	-38 26 10	14.4	13.7	1.0	4700	1.5	-2.5	-3.0	CaKidx
HE 0014-2141	00 16 56.3	-21 25 03	16.5	16.2	0.5	5700	3.7	-1.9	-2.4	auto
HE 0019-3635	00 22 06.0	-36 18 34	16.5	16.3	0.4	5800	3.6	-2.0	-2.5	auto
HE 0020-5123	00 22 52.1	-51 06 57	15.7	15.4	0.5	6200	4.0	-1.8	-2.3	auto
HE 0028-2152	00 31 07.7	-21 36 07	16.0	15.8	0.3	6000	3.9	-1.9	-2.4	auto
HE 0032-4749	00 35 22.1	-47 32 32	16.4	16.2	0.4	6300	4.6	-1.8	-2.3	auto
HE 0051-1334	00 54 06.8	-13 18 11	15.5	15.2	0.4	5900	3.9	-1.8	-2.3	auto
HE 0051-2950	00 53 39.8	-29 34 13	13.9	13.6	0.4	6250	3.2	-2.2	-2.7	CaKidx
HE 0054-2123	00 56 53.2	-21 07 29	15.7	15.4	0.4	6200	3.6	-1.8	-2.3	auto
HE 0058-5557	01 00 11.9	-55 41 24	16.3	16.0	0.4	6300	3.8	-1.9	-2.4	auto
HE 0105-2202	01 07 31.2	-21 46 06	15.9	15.6	0.3	5800	4.2	-2.1	-2.6	auto
HE 0113-3702	01 15 21.9	-36 47 05	16.3	15.9	0.5	6100	4.4	-1.7	-2.2	auto
HE 0114-4039	01 16 41.1	-40 23 55	16.4	16.0	0.5	5900	3.5	-1.6	-2.1	auto
HE 0119-4211	01 22 11.2	-41 56 14	15.6	15.2	0.6	5300	2.0	-2.3	-2.8	CaKidx
HE 0122-4743	01 24 34.1	-47 28 22	15.9	15.6	0.4	5900	3.9	-2.0	-2.5	auto
HE 0130-2303	01 33 18.2	-22 48 36	14.9	14.7	0.4	6500	4.5	-2.3	-2.8	CaKidx
HE 0131-2638	01 33 43.3	-26 23 16	15.8	15.6	0.4	6200	4.2	-1.5	-2.0	auto
HE 0131-2740	01 33 25.8	-27 25 28	15.1	14.7	0.5	5600	3.5	-2.1	-2.6	CaKidx
HE 0132-2439	01 34 58.8	-24 24 18	15.2	14.8	0.5	5450	3.3	-2.9	-3.4	CaKidx
HE 0142+0147	01 44 47.8	+02 02 18	15.9	15.6	0.3	6200	3.9	-2.2	-2.7	auto
HE 0148-2611	01 50 59.5	-25 57 02	14.9	14.7	0.4	6400	3.3	-3.2	-3.7	CaKidx
HE 0201-4707	02 03 24.4	-46 52 48	15.2	14.9	0.5	6300	4.1	-1.7	-2.2	auto
HE 0202-0104	02 04 37.0	-00 49 49	15.5	15.2	0.3	6300	4.5	-1.5	-2.0	auto
HE 0221-2127	02 23 25.2	-21 13 35	16.1	15.8	0.4	6200	3.8	-1.7	-2.2	auto
HE 0222-5707	02 24 09.2	-56 54 25	16.5	16.2	0.4	5900	3.7	-1.5	-2.0	auto
HE 0225-0033	02 27 35.4	-00 20 15	15.9	15.6	0.3	5900	3.8	-2.0	-2.5	auto
HE 0226-5519	02 28 34.2	-55 05 45	16.5	16.2	0.4	5900	3.2	-1.8	-2.3	auto
HE 0235-3649	02 37 58.3	-36 37 02	14.8	14.5	0.4	7000	3.0	-1.6	-2.1	CaKidx
HE 0236-2809	02 38 55.9	-27 56 59	16.5	16.2	0.4	6300	4.0	-2.0	-2.5	auto
HE 0238-0852	02 40 40.2	-08 39 24	16.1	15.9	0.3	6000	3.9	-1.8	-2.3	auto
HE 0239-5127	02 41 12.1	-51 14 51	16.7	16.4	0.3	5800	3.2	-1.6	-2.1	auto
HE 0240-2839	02 42 53.2	-28 26 30	16.1	15.8	0.4	6200	4.0	-1.5	-2.0	auto
HE 0242-0728	02 44 53.2	-07 15 51	15.9	15.6	0.4	6000	3.7	-2.2	-2.7	auto
HE 0242-0732	02 45 00.6	-07 19 42	16.0	15.7	0.4	6200	4.7	-2.7	-3.2	auto
HE 0249-0126	02 51 39.7	-01 14 33	15.9	15.6	0.4	6100	3.8	-2.0	-2.5	auto
HE 0251-4743	02 52 58.2	-47 31 26	15.9	15.6	0.5	6200	4.8	-2.0	-2.5	auto
HE 0309-0857	03 12 25.5	-08 46 35	15.4	15.2	0.3	5900	3.2	-2.0	-2.5	auto
HE 0312-3418	03 14 52.1	-34 07 18	15.5	15.2	0.5	6500	3.8	-1.8	-2.3	CaKidx
HE 0313-3640	03 15 01.8	-36 29 54	14.6	14.2	0.5	6550	4.0	-2.8	-3.3	CaKidx
HE 0332-2657	03 34 53.3	-26 47 39	15.7	15.5	0.4	6200	4.3	-2.0	-3.0	auto
HE 0338-2657	03 40 35.3	-26 48 18	15.5	15.2	0.4	5800	3.7	-1.5	-2.0	auto
HE 0338-5454	03 39 29.7	-54 44 30	15.5	15.2	0.4	5800	2.5	-1.9	-2.4	auto
HE 0341-5112	03 43 18.7	-51 03 11	15.3	15.1	0.3	6350	3.2	-2.1	-2.6	CaKidx
HE 0350-4804	03 51 36.9	-47 55 47	16.4	16.1	0.4	6100	4.5	-2.0	-2.5	CaKidx

(continued on next page)

(continued from previous page)

Name	α(2000)	δ(2000)	B_J	V	$B-V$	T_{eff}	$\log g$	$[\mathrm{Fe/H}]_{\mathrm{HES}}$	$[\mathrm{Fe/H}]_{\mathrm{HK}}$	Method
HE 0357-5054	03 59 18.5	-50 45 47	16.8	16.5	0.4	6100	3.8	-2.0	-2.5	auto
HE 0401-5212	04 03 02.5	-52 04 46	14.4	14.1	0.4	6500	4.0	-2.5	-3.0	CaKidx
HE 0417-4040	04 19 38.0	-40 33 49	14.4	14.2	0.3	6200	4.5	-2.7	-3.2	CaKidx
HE 0419-5544	04 20 12.2	-55 37 38	16.9	16.6	0.4	5800	3.3	-2.1	-2.6	auto
HE 0424-5411	04 25 20.0	-54 04 38	16.5	16.2	0.4	5900	3.5	-1.5	-2.0	auto
HE 0426-3913	04 28 14.2	-39 07 03	15.3	15.0	0.4	5900	3.9	-1.9	-2.4	auto
HE 0427-3337	04 29 33.1	-33 30 55	14.9	14.7	0.3	6700	3.2	-1.8	-2.3	CaKidx
HE 0442-5113	04 43 15.8	-51 07 47	15.5	15.2	0.5	5900	3.7	-1.9	-2.4	CaKidx
HE 0445-3506	04 47 26.5	-35 01 03	13.9	13.6	0.4	6200	4.0	-1.8	-2.3	CaKidx
HE 0448-3524	04 50 08.6	-35 19 05	15.4	15.0	0.4	6100	3.8	-0.4	-0.9	CaKidx
HE 0503-5519	05 04 32.5	-55 14 59	14.9	14.7	0.3	6200	3.4	-1.2	-1.7	auto
HE 0507-3915	05 08 43.2	-39 11 19	16.1	15.7	0.5	5800	3.2	-1.9	-2.4	auto
HE 0512-2355	05 14 23.8	-23 51 50	15.6	15.3	0.4	5700	3.3	-2.2	-2.7	auto
HE 0513-2421	05 16 01.6	-24 18 10	14.8	14.5	0.4	5900	3.9	-1.9	-2.4	auto
HE 0513-4557	05 15 12.1	-45 54 10	16.1	15.8	0.4	5700	3.5	-2.2	-2.7	auto
HE 0514-5711	05 15 41.5	-57 07 57	15.3	15.1	0.4	5900	3.4	-1.9	-2.4	auto
HE 0519-5525	05 19 59.1	-55 22 41	15.4	15.0	0.5	6100	4.3	-1.4	-1.9	auto
HE 0544-4416	05 45 59.1	-44 14 58	14.7	14.4	0.3	6400	3.5	-2.5	-3.0	CaKidx
HE 0545-4715	05 46 50.8	-47 14 07	14.2	13.8	0.7	5350	3.2	-3.3	-3.8	CaKidx
HE 0548-4121	05 49 52.9	-41 20 39	15.6	15.4	0.4	6300	4.1	-2.0	-2.5	auto
HE 1143-0010	11 46 10.2	-00 27 21	14.3	14.0	0.5	6500	4.8	-2.3	-2.8	CaKidx
HE 1155-1501	11 58 06.0	-15 18 25	14.8	14.6	0.4	6400	4.3	-2.5	-3.0	CaKidx
HE 1219-0045	12 22 28.4	-01 02 17	15.4	15.1	0.4	6200	3.0	-2.6	-3.1	CaKidx
HE 1219-0413	12 22 09.4	-04 30 12	16.1	15.9	0.4	6200	3.5	-2.4	-2.9	CaKidx
HE 1227-2755	12 30 14.1	-28 11 39	13.5	13.3	0.4	6400	4.2	-2.3	-2.8	CaKidx
HE 1257-3113	13 00 31.9	-31 29 33	12.9	12.6	0.5	6200	4.0	-2.2	-2.7	CaKidx
HE 1303-2708	13 06 37.8	-27 24 22	15.5	15.3	0.4	6500	4.2	-2.8	-2.3	CaKidx
HE 1306-0954	13 08 55.3	-10 10 34	15.3	15.0	0.4	6000	3.0	-2.4	-2.9	CaKidx
HE 1320-1219	13 23 31.1	-12 35 12	14.4	14.2	0.4	6500	4.5	-2.0	-2.5	CaKidx
HE 1353-2735	13 56 42.5	-27 49 54	15.0	14.7	0.4	6000	4.8	-2.9	-3.4	CaKidx
HE 1354-2810	13 57 36.1	-28 25 19	14.6	14.4	0.4	6200	3.5	-2.3	-2.8	CaKidx
HE 1444-1610	14 47 44.3	-16 23 14	15.2	14.9	0.4	6000	3.0	-2.5	-3.0	CaKidx
HE 1447-2008	14 50 25.4	-20 21 09	14.4	14.0	0.6	6200	3.5	-2.4	-2.9	CaKidx
HE 1528-1048	15 31 03.7	-10 58 19	14.5	14.2	0.5	6300	3.8	-2.0	-2.5	CaKidx
HE 2133-1426	21 36 07.2	-14 12 36	16.0	15.7	0.3	5900	4.1	-2.7	-3.2	auto
HE 2148-1247	21 51 17.8	-12 33 42	15.2	14.9	0.4	6200	3.7	-1.6	-2.1	auto
HE 2152-3058	21 55 52.3	-30 44 29	15.9	15.6	0.3	6700	3.9	-1.7	-2.2	auto
HE 2155-2836	21 58 10.0	-28 22 02	16.1	15.9	0.4	6200	4.4	-1.5	-2.0	auto
HE 2202-2020	22 05 07.7	-20 05 35	15.8	15.5	0.5	5800	4.1	-2.4	-2.9	auto
HE 2306-6115	23 09 10.8	-60 59 22	16.4	16.1	0.3	5500	2.2	-2.2	-2.7	auto
HE 2321-5854	23 24 29.2	-58 38 30	16.3	16.0	0.4	6000	3.4	-2.0	-2.5	auto
HE 2326-6005	23 28 56.0	-59 48 47	16.7	16.4	0.4	5800	3.5	-2.1	-2.6	auto
HE 2328-5839	23 31 35.6	-58 23 05	16.3	16.0	0.5	5900	3.9	-2.1	-2.6	auto
HE 2338-3108	23 41 09.0	-30 51 35	16.0	15.7	0.4	5800	3.2	-1.8	-2.3	auto

Table 24: Metal-poor stars discovered in the HES. Stars selected by the Ca K index method are marked with "CaKidx"; stars found with automatic classification are labeled with "auto". Metal abundances are on the HES scale; for conversion to the HK survey scale, -0.5 dex have to subtracted.

B HES Carbon Stars Without Significant P.M.

Name	α(2000.0)	δ(2000.0)	B_J	$(B-V)^*_{\mathrm{HES}}$	V_{HES}	Comment
HE 0915-0327	09 18 08.2	-03 39 57	14.5	2.3	12.8	TI98
HE 0926-0417	09 29 10.3	-04 30 44	14.1	1.2	13.3	
HE 0954+0137	09 57 19.2	+01 23 00	16.6	1.2	15.7	
HE 1008-0636	10 10 37.0	-06 51 13	14.5	2.3	12.9	
HE 1008-0946	10 11 22.4	-10 01 13	16.8	1.4	15.8	
HE 1011-0942	10 14 25.0	-09 57 54	15.4	1.6	14.2	
HE 1015-2050	10 17 34.2	-21 05 14	16.8	0.9	16.2	
HE 1019-1136	10 22 14.7	-11 51 39	15.2	1.8	13.9	TI98
HE 1023-1504	10 25 55.5	-15 19 18	15.7	1.8	14.4	
HE 1027-2501	10 29 29.5	-25 17 16	13.9	1.7	12.7	
HE 1036-2615	10 38 25.9	-26 30 50	14.6	1.2	13.7	
HE 1045-1434	10 47 44.1	-14 50 23	15.5	1.2	14.6	
HE 1051-0112	10 53 58.8	-01 28 15	17.0	1.4	16.0	
HE 1051-0518	10 54 28.8	-05 34 21	14.3	1.5	13.2	
HE 1102-2142	11 04 31.2	-21 58 29	16.0	1.4	14.9	
HE 1104-0957	11 07 19.4	-10 13 16	–	1.3	10.7**	
HE 1107-2105	11 09 59.6	-21 22 01	14.3	3.4	11.9	
HE 1110-0153	11 13 02.7	-02 09 28	16.5	1.5	15.5	
HE 1117-3020	11 20 23.5	-30 36 42	16.7	1.1	15.9	
HE 1119-2953	11 21 27.3	-30 10 06	12.8	1.3	11.9	
HE 1119-1933	11 21 43.5	-19 49 47	15.6	1.3	14.6	
HE 1119-3229	11 22 21.9	-32 46 19	14.0	1.2	13.1	
HE 1120-2122	11 23 18.6	-21 38 33	12.9	1.4	11.9	
HE 1123-2031	11 26 08.7	-20 48 19	16.8	1.3	15.8	
HE 1125-1357	11 27 43.0	-14 13 32	15.2	1.4	14.2	
HE 1125-2942	11 27 57.9	-29 59 04	15.0	1.7	13.8	
HE 1126-3001	11 28 57.6	-30 18 02	17.1	1.3	16.1	
HE 1150-2218	11 53 18.0	-22 35 23	14.9	1.3	14.0	
HE 1150-2800	11 53 26.2	-28 17 03	15.7	1.0	15.0	
HE 1150-2049	11 53 27.7	-21 05 50	15.6	1.0	14.9	
HE 1152-2702	11 55 26.3	-27 19 12	15.8	1.9	14.4	
HE 1221-2557	12 24 32.8	-26 14 07	12.8	2.1	11.3	
HE 1222-2952	12 25 31.4	-30 09 33	16.4	1.7	15.2	
HE 1259-2550	13 02 35.4	-26 06 49	13.9	1.8	12.6	
HE 1308-1012	13 11 10.9	-10 28 35	14.6	1.3	13.7	
HE 1315-2035	13 17 57.4	-20 50 53	16.7	1.3	15.7	
HE 1318-1657	13 21 19.4	-17 13 40	15.4	1.4	14.4	
HE 1319-1935	13 22 38.7	-19 51 11	15.3	1.4	14.3	
HE 1320-3150	13 23 27.8	-32 06 18	15.8	1.6	14.6	
HE 1324-3142	13 27 43.6	-31 57 50	13.0	1.5	11.9	
HE 1325-1638	13 28 37.7	-16 54 27	16.2	1.5	15.1	
HE 1326-1549	13 29 19.9	-16 05 00	15.6	1.5	14.5	
HE 1328-1357	13 31 02.4	-14 13 05	16.0	1.4	15.0	
HE 1331-2558	13 34 20.1	-26 13 38	17.1	1.5	16.0	
HE 1337-2203	13 39 46.4	-22 19 01	17.0	1.6	15.8	

* From calibration of `dx_hpp2` (see Tab. 6).
** CCD photometry.

Table 25: HES C stars without significant p.m. Objects marked with TI98 have been previously published by Totten & Irwin (1998). Totten et al. (2000) report all of them to have no significant p.m., in agreement with our result.

Name	α(2000.0)	δ(2000.0)	B_J	$(B-V)^*_{\mathrm{HES}}$	V_{HES}	Comment
HE 1337-0938	13 39 53.2	-09 53 49	16.5	1.5	15.5	
HE 1337-2923	13 40 13.7	-29 38 26	13.3	1.3	12.4	
HE 1339-2805	13 42 09.4	-28 21 02	14.2	1.2	13.4	
HE 1339-3016	13 42 24.6	-30 31 17	14.3	1.3	13.4	
HE 1339-0700	13 42 26.8	-07 15 23	15.0	1.7	13.7	TI98
HE 1342-2856	13 45 29.9	-29 11 30	15.3	1.2	14.5	
HE 1344-0411	13 47 25.7	-04 26 04	16.3	2.0	14.9	
HE 1347-1115	13 50 34.0	-11 29 57	16.8	1.4	15.8	
HE 1347-2646	13 50 41.3	-27 01 39	14.7	1.2	13.8	
HE 1349-2330	13 51 58.3	-23 45 20	15.4	1.3	14.4	
HE 1354-2257	13 57 43.3	-23 12 34	14.9	1.2	14.0	
HE 1355-1541	13 57 44.7	-15 56 28	15.5	1.3	14.5	
HE 1355-1758	13 57 56.0	-18 13 00	16.7	1.7	15.5	
HE 1356-2752	13 59 25.0	-28 06 59	13.3	1.3	12.3	
HE 1357-3049	14 00 06.4	-31 03 46	14.5	1.3	13.6	
HE 1358-2508	14 01 12.3	-25 22 39	13.2	1.3	12.3	
HE 1359-2841	14 01 54.9	-28 56 25	15.4	1.4	14.4	
HE 1400-1113	14 03 39.8	-11 28 04	16.0	1.2	15.1	
HE 1401-0745	14 04 08.9	-07 59 46	15.7	1.2	14.9	
HE 1404-0846	14 06 55.1	-09 00 58	15.3	1.5	14.3	
HE 1418-0306	14 20 57.1	-03 19 54	14.2	1.6	13.0	
HE 1418+0150	14 21 01.2	+01 37 18	–	1.4	12.4**	
HE 1425-2052	14 28 39.5	-21 06 05	13.6	1.3	12.6	
HE 1429-1411	14 32 40.6	-14 25 06	12.5	2.0	11.1	
HE 1430+0227	14 32 46.5	+02 14 44	17.1	1.7	15.9	
HE 1430-0919	14 33 12.9	-09 32 53	15.0	1.2	14.2	
HE 1431-0245	14 33 54.2	-02 58 33	16.2	1.3	15.3	
HE 1431-0755	14 34 32.7	-08 08 37	14.6	1.5	13.5	
HE 1432-2138	14 35 47.6	-21 51 37	17.1	1.2	16.2	
HE 1439-1338	14 42 26.4	-13 51 18	14.5	1.4	13.5	
HE 1440-1511	14 43 07.1	-15 23 48	14.6	1.2	13.7	
HE 1442-0058	14 44 48.9	-01 10 57	17.8	2.1	16.2	TI98
HE 1442-0346	14 45 02.1	-03 58 46	16.3	1.3	15.4	
HE 1443-0503	14 46 30.2	-05 16 21	13.9	1.2	13.1	
HE 1446-0112	14 49 02.2	-01 25 24	14.5	1.4	13.5	
HE 1447+0102	14 50 15.1	+00 50 15	15.6	1.0	14.9	
HE 1501-1500	15 04 26.3	-15 12 00	16.5	1.6	15.3	
HE 1522-0503	15 24 42.4	-05 14 29	14.9	1.0	14.2	
HE 1523-1155	15 26 41.0	-12 05 43	14.3	1.2	13.4	
HE 1525-0516	15 27 52.2	-05 27 04	16.8	1.3	15.8	
HE 1528-0409	15 30 54.3	-04 19 40	15.8	1.1	15.0	

* From calibration of `dx_hpp2` (see Tab. 6).
** CCD photometry.

Table 26: HES C stars without significant p.m., continued. Objects marked with TI98 have been previously published by Totten & Irwin (1998). Totten et al. (2000) report all of them to have no significant p.m., in agreement with our result.

C HES FHB/A Stars

Name	l	b	V	$(B-V)_0$	$(U-B)_0$	$T_{\rm eff}$	$\log g$	[Fe/H]	M_V	d	$v_{\rm rad}$	class
HE 0012-3738	336.9	−77.7	15.58	0.22	−0.01	7873.	4.06	−2.74	0.52	4.6	93	A
HE 0107-3950	284.6	−77.1	12.62	0.18	0.12	7943.	3.44	−1.02	0.15	1.3	1	Am
HE 0107-4205	287.8	−75.0	14.84	−0.07	−0.27	9722.	3.02	−1.07	0.22	4.4	72	FHB
HE 0107-4217	288.2	−74.8	13.94	0.23	0.09	7047.	2.23	−1.55	0.08	4.5	84	FHB
HE 0108-3839	282.0	−78.1	15.33	0.12	0.16	7919.	3.03	−2.26	0.01	8.7	−231	FHB
HE 0108-4121	286.1	−75.6	14.64	0.18	0.12	7869.	3.26	−0.64	0.14		42	FHB/A
HE 0109-3753	279.1	−78.7	15.13	0.23	0.00	7623.	3.82	−0.90	0.60	3.7	67	A
HE 0111-3736	277.1	−78.8	14.60	0.24	−0.05	7372.	3.51	−2.54	0.56	2.8	−67	A
HE 0115-4104	281.1	−75.3	12.48	0.14	0.13	7661.	2.75	−2.30	0.05	2.4	−23	FHB
HE 0117-3859	275.5	−77.0	13.83	0.27	0.06	7374.	3.15	−1.71	0.02	1.9	24	Am
HE 0126-3926	270.6	−75.6	12.39	0.23	0.15	7851.	4.56	−0.01	0.02	1.0	44	A
HE 0131-3800	263.5	−76.0	15.64	0.26	0.05	7123.	2.63	−1.41	0.53	4.4	−15	Am
HE 0131-4112	271.8	−73.7	16.23	0.23	0.06	7460.	3.19	−1.67	0.06	13.1	155	FHB
HE 0133-3830	264.0	−75.4	14.32	0.27	0.02	7626.	4.14	−0.12	0.23	2.4	−40	A
HE 0133-3914	266.0	−74.9	16.85	0.23	−0.12	7623.	4.27	−1.59	0.08	8.1	239	A
HE 0134-3912	265.1	−74.7	16.18	0.30	−0.03	7123.	3.37	−1.50	0.01	5.5	236	A
HE 0134-4101	269.6	−73.4	16.42	0.31	−0.06	6432.	2.31	−3.00	0.00	16.0	149	FHB
HE 0134-4126	270.7	−73.1	17.14	0.36	0.11	6776.	2.23	−1.78	0.10	20.1	24	FHB
HE 0135-3908	264.4	−74.6	14.55	0.42	−0.04	6201.	2.21	−2.66	0.44	6.6	102	FHB
HE 0135-4044	268.8	−73.5	15.27	0.05	0.14	8265.	3.15	−1.79	0.00	7.5	113	FHB
HE 0135-4119	270.0	−73.1	17.17	0.20	0.13	7375.	2.13	−1.75	0.29	20.3	−59	FHB
HE 0136-4035	267.9	−73.5	14.55	0.40	−0.01	6536.	3.22	−0.46	0.92		31	FHB/A
HE 0137-4106	268.5	−73.0	15.26	0.24	0.10	7129.	2.47	−2.17	0.19	8.7	217	FHB
HE 0138-3941	264.6	−73.9	15.64	0.31	0.01	7221.	3.37	−1.46	0.10	4.2	−31	A
HE 0139-3830	260.8	−74.5	15.13	0.06	0.13	8309.	3.29	−1.97	0.24		154	FHB/A
HE 0139-4051	266.8	−72.9	17.38	−0.04	−0.21	9871.	3.12	0.00	0.00	14.2	119	FHB
HE 0140-4045	266.5	−72.9	16.61	0.13	0.13	8191.	3.54	−1.33	0.32	9.3	30	A
HE 0140-4213	269.6	−71.8	17.20	0.03	0.20	8446.	3.21	−1.21	0.02	16.9	136	FHB
HE 0141-4135	267.7	−72.1	14.28	0.24	−0.02	7125.	3.21	−1.72	0.25		61	FHB/A
HE 0142-3740	257.0	−74.6	14.09	0.22	0.06	7674.	3.77		0.00	2.3	69	A
HE 0143-3912	261.0	−73.5	14.96	−0.01	0.03	9099.	3.39	−1.84	0.43		30	FHB/A
HE 0143-4055	265.4	−72.3	16.55	0.14	−0.04	8164.	4.31	−1.57	0.12	8.7	−12	A
HE 0144-3750	256.8	−74.2	12.96	0.23	0.02	7624.	3.76	−0.81	0.01	1.3	−22	Am
HE 0144-3903	260.3	−73.5	16.96	0.44	0.06	6305.	2.20	−1.45	0.00	18.0	85	FHB
HE 0145-3834	258.5	−73.6	16.17	0.23	−0.02	7871.	4.19	−1.59	0.03	5.9	177	A
HE 0147-3809	256.2	−73.4	16.97	0.00	0.05	8951.	3.79	−0.23	0.26	18.8	180	A
HE 0147-3811	256.3	−73.4	16.89	0.30	−0.11	7003.	3.75	−1.47	0.22	7.6	168	A
HE 0148-3914	259.1	−72.8	17.30	0.09	0.25	7998.	2.94	−2.64	0.72	21.6	−112	FHB
HE 0148-3945	260.2	−72.3	17.23	0.06	0.13	7625.	2.33	−2.72	0.24	20.4	−122	FHB
HE 0148-3954	260.5	−72.2	17.32	0.15	0.11	7549.	3.04		0.00	18.2	240	FHB
HE 0148-4057	263.4	−71.6	16.84	0.45	−0.26	6372.	4.20	−2.62	0.29	7.8	156	A
HE 0149-3834	256.7	−72.9	14.32	0.22	−0.10	7872.	4.42	−1.46	0.22	2.6	41	A
HE 0149-4029	261.9	−71.8	16.95	0.23	−0.05	7376.	3.63	−2.47	0.34	8.5	210	A
HE 0149-4034	262.2	−71.8	15.47	0.13	0.11	7404.	2.33	−2.28	0.24	9.3	−20	FHB
HE 0150-3840	256.6	−72.7	13.74	−0.07	−0.24	9865.	3.04		0.00	2.4	65	FHB
HE 2349-3902	345.6	−73.6	17.20	0.13	0.13	7763.	3.00	−2.85	0.26		188	FHB

(continued on next page)

(continued from previous page)

Name	l	b	V	$(B-V)_0$	$(U-B)_0$	$T_{\rm eff}$	$\log g$	[Fe/H]	M_V	d	$v_{\rm rad}$	class
HE 2352-4024	340.9	−73.0	12.83	0.03	0.13	8283.	3.04	−2.00	0.06	16.2	−79	FHB
HE 2354-4158	336.4	−72.2	17.06	0.01	−0.04	9029.	3.13	−2.32	0.41	12.2	84	FHB
HE 2355-3753	345.9	−75.3	16.73	0.10	0.10	8052.	3.26	−0.58	0.39		−315	FHB/A
HE 2356-4059	337.4	−73.2	16.64	0.40	−0.02	6475.	2.23	−3.00	0.00	22.0	−105	FHB

Table 27: Results from spectroscopy and photometry of FHB/A stars from the HES. Distances d are in kpc, heliocentric radial velocities $v_{\rm rad}$ in km/s.

General Acknowledgements

First of all I would like to thank Prof. Reimers, the supervisor of my PhD, and P.I. of the HES, for entrusting me with the exploitation of the stellar content of the HES, and many valuable advices. I could be sure of his support, whatever matter was concerned, and I can hardly remember any duties, so that I could fully concentrate on my thesis work.

My work would have been impossible without the existence of the HES data base. The survey as it exists today was mainly conceived by Lutz Wisotzki. He contributed to the conception of stellar applications, and a considerable fraction of the algorithms and methods I used have their "roots" in work he has done before I got involved in the HES. Throughout the many years we worked together on the HES, Lutz was a continuous source of valuable advices and suggestions. He also programmed almost all of the huge, sophisticated HES data reduction package.

I would like to express gratitude to my external collaborators again. It was very exciting to work with experts on many different fields of astronomy, and to learn from them. I mentioned these persons already at the end of the sections to which they have contributed. Tim Beers deserves special thanks for the almost daily e-mail correspondence with me, and for introducing me to many important people in metal-poor star business at conferences we attended together.

I thank Tim Beers, Paul Green and Lutz Wisotzki for smoothing my English and proof-reading the manuscript, or parts of it. Of course, the author takes the full responsibility for all clumsy formulations or errors the reader may still find!

I made extensive use of NASA's Astrophysics Data System Abstract Service (ADS), and the LEO English/German Dictionary (`http://dict.leo.org/`).

Funding for this work was provided under DFG grant Re 353/40, and BMBF-DLR grant 50 OR 9606 0, which I gratefully acknowledge.

Erklärung

Hiermit erkläre ich, dass ich die vorliegende Arbeit selbständig verfasst habe – soweit nicht anders am Ende jedes Kapitels im Abschnitt *Acknowledgements* verzeichnet – und nur die angegebenen Quellen und Hilfsmittel benutzt habe.

Hamburg, den 31. März 2000

Lebenslauf

14.8.1966	geboren in Hamburg
1986	Abitur in Hamburg, Durchschnittsnote: 2,8
1986–1988	Zivildienst beim DRK Hamburg
1988	Immatrikulation an der Universität Hamburg im Fach Physik
Nov. 1991–Juli 1995	stud. Hilfskraft im DFG-Projekt “Epistemische Systeme”, Projektleiter: Prof. Dr. G. Graßhoff
Sept. 1994–Dez. 1995	Diplomarbeit an der Hamburger Sternwarte bei Prof. Dr. D. Reimers, Thema: Automatische Spektralklassifikation
Sept. 1995–Jan. 1996	Werkvertrag mit dem Max-Planck Institut für Wissenschaftsgeschichte, Berlin; Projektthema: “Kalte Fusion”
Jan. 1996	Diplom in Physik, Universität Hamburg, Note: “sehr gut”.
März 1996–Juli 1996	wissenschaftlicher Mitarbeiter am Philosophischen Seminar, Universität Hamburg
Juli 1996	Teilnahme an der 5. ESO/OHP Sommerschule über astronomische Beobachtungen
Sept. 1996–März 2000	wissenschaftlicher Mitarbeiter an der Hamburger Sternwarte
Nov. 1998–Dez. 1998	Forschungsaufenthalt an der Europäischen Südsternwarte, Santiago de Chile (3 Wochen)
Mai 1999	Forschungsaufenthalt am Harvard-Smithsonian Center for Astrophysics, Cambridge, Massachusetts (10 Tage)

Publikationsliste

Artikel in referierten wissenschaftlichen Zeitschriften

(3) Wisotzki, L., **Christlieb, N.**, Bade, N., Beckmann, V., Köhler, T., Vanelle, C., Reimers, D. (2000), *The Hamburg/ESO survey for bright QSOs. III. A large flux-limited sample of QSOs*, A&A, im Druck.

(2) Wisotzki, L., **Christlieb, N.**, Liu, M.C., Maza, J., Morgan, N.D., Schechter, P.L. (1999), *The new complex gravitational lens system HE 0230-2130*, A&A 348, L41–L44.

(1) Reimers, D., Jordan, S., Beckmann, V., **Christlieb, N.**, Wisotzki, L. (1998), *Four magnetic DB white dwarfs discovered by the Hamburg/ESO survey*, A&A 337, L13–L16.

Artikel in referierten und nicht referierten Konferenzbänden

(6) **Christlieb, N.**, Beers, T.C. (2000), *Ongoing Large Surveys for Metal-Poor Stars in the Galactic Halo*, in: Proceedings of 2nd Subaru HDS Workshop, M. Takada-Hidai (Hg.), im Druck; astro-ph/0001378.

(5) **Christlieb, N.**, Wisotzki, L., Reimers, D., Gehren, T., Reetz, J., Beers, T.C. (2000), *Finding the First Stars: The Hamburg/ESO Objective Prism Survey*, in: The First Stars, A. Weiss et al. (Hg.), Springer, Heidelberg, im Druck; astro-ph/9911016.

(4) **Christlieb, N.**, Wisotzki, L., Reimers, D., Gehren, T., Reetz, J., Beers, T.C. (1999), *An automated search for metal-poor halo stars in the Hamburg/ESO objective-prism survey*, in: The Third Stromlo Symposium: The Galactic Halo, B.K. Gibson et al. (Hg.), ASP Conference Series 165, S. 263–267.

(3) **Christlieb, N.**, Graßhoff, G., Nelke, A., Schlemminger, A. & Wisotzki, L. (1998b), *Linné, a software system for automatic classification*, in: Proceedings of ADASS VII, R. Albrecht et al. (Hg.), ASP Conference Series 145, S. 457–460.

(2) **Christlieb, N.**, Graßhoff, G., Nelke, A., Schlemminger, A. & Wisotzki, L. (1998a), *Automatic spectral classification*, in: Classification, Data Analysis, and Data Highways, I. Balderjahn et al. (Hg.), S. 16–23, Springer, Berlin.

(1) **Christlieb, N.**, Graßhoff, G., Nelke, A. & Wisotzki, L. (1997), *Automatic classification of digitized objective prism spectra*, in: Kontizas et al. (Hg.), Wide-Field Spectroscopy, S. 109–113, Kluwer, Dordrecht.

Andere Veröffentlichungen

(3) Patat, F., **Christlieb, N.**, Sollermann, J. (1998), *Supernova 1998ew in NGC 6943*, IAU Circular 7061, 27. November 1998.

(2) **Christlieb, N.** (1995), *Automatische Klassifikation von digitalisierten Objektivprismen-Spektren*, Diplomarbeit, Universität Hamburg.

(1) **Christlieb, N.** & Wisotzki, L. (1995), *Automatic classification of objective prism spectra*, AG Abstract Series 11, 103.